SHEAR STRESS AND FOULING CONTROL IN HOLLOW FIBER MEMBRANE SYSTEMS UNDER DIFFERENT GAS SPARGING CONDITIONS

by

Dongying Ye

B.Eng, National University of Singapore, 2009

A THESIS SUBMITTED IN PARTIAL FULFILMENT OF
THE REQUIREMENTS FOR THE DEGREE OF

MASTER OF APPLIED SCIENCE

in

The Faculty of Graduate Studies
(Civil Engineering)

THE UNIVERSITY OF BRITISH COLUMBIA
(Vancouver)

August, 2012

ABSTRACT

The shear stress created by gas sparging has been widely recognized as a controlling factor in the fouling of submerged membrane systems. Effective gas sparging can significantly reduce the fouling and improve the membrane performance. Several factors, such as membrane module configuration, gas sparging tank configuration, gas sparging pattern and temperature, affect the hydrodynamic conditions around the membrane. Chan *et al.* (2011) reported that different types of shear profiles exist inside the submerged hollow fiber membrane module, and the different types of shear conditions have different effects on fouling control. In this thesis, the relationship between the shear stress generated by conventional sparging and a novel sparging approach on fouling control were studied. The results indicate that, to achieve the similar fouling control (fouling rate), only a quarter of energy (i.e air flow rate) input was required for the novel slug bubble sparger, compared to the conventional coarse bubble sparger.

TABLE OF CONTENTS

LIST OF TABLES

LIST OF FIGURES

ACKNOWLEDGEMENTS

First of all, I would like to thank my thesis supervisors, Dr. Pierre Bérubé for his valuable insight, guidance, and trust throughout my M.A.Sc. study. Without his continuous support, I wouldn't be able to overcome all the obstacles encountered during different stages of this research.

I would also like to thank Bill Leung and Scott Jackson for their genuine help in building the experiment apparatus and electrical set-up for the shear stress measurements and filtration tests. Special thanks to Paula Parkinson and Tim Ma for their technical assistance and advice in the Environmental laboratory, and their patience to bear with me for my demanding requirements of pipe fittings.

In addition, I would like to thank PhD candidate Sepideh Jankhah for teaching me how to fabricate and calibration the shear probe and PhD candidate Syed Abdhullah for sharing his knowledge of the membrane filtration.

I am sincerely grateful to my parents, for all they have done for me so that I can be where I am today. I am forever grateful for their boundless love and sacrifices.

Last but not least, without the support from my girlfriend Corrine, I wouldn't be able to live with my passion of research and commit myself to my M.A.Sc. study. Thank you for your unconditional and care all along the way. I am really grateful to have you with me.

1. INTRODUCTION

The tightening of regulations on drinking water quality and wastewater discharge limits has led to an increasing demand for advanced water and wastewater treatment technologies. With its excellent filtration capability and decreasing cost, membrane technology attracts the growing attention of researchers in the field of water and wastewater treatment.

The use of membranes in biological treatment of wastewater is becoming one of the most important applications of membranes. Compared to the conventional technologies, membrane bioreactors (MBR) offer many advantages, including smaller footprint, better treated water quality, higher volumetric loadings and less sludge production.

Despite the many benefits of membrane technologies, the unavoidable problem of membrane fouling remains during membrane filtration. Membrane fouling is a process where solute or particles deposit onto a membrane surface or into membrane pores. Membrane fouling causes a reduction in the permeate yield and a decrease quality of water produced (Metcalf and Eddy, 1991, 2003), which leads to the increase of operational and capital costs of the entire membrane filtration processes.

Shear forces are recognized to promote the mass transfer of foulants away from membrane surfaces and therefore contribute to fouling control. In the nanofiltration (NF) and reverse osmosis (RO) system, the cross-flow operation is typically used to induce shear stresses at the membrane surface for fouling control. In submerged microfiltration (MF) and ultrafiltration (UF) membrane systems, the gas sparging under the membrane module is commonly used to induce shear stresses at the membrane surface for fouling control. However, due to the complex conditions in the gas sparging membrane systems, the mechanisms of fouling control by sparging are poorly understood.

In the recent studies, Bérubé *et al.* (2006), Chan *et al.* (2007) and Fulton *et al.* (2011) demonstrated that air sparging can create different kind of shear profiles in submerged hollow fiber systems. Chan *et al.* (2011) also did a comprehensive study investigating the effects of sparger location, fiber movement and physical contact between fibers on the shear stress induced on the hollow fiber membrane surface. This research indicated that hydrodynamic conditions will affect the mass transfer at the membrane surface and affect the fouling control. The present thesis builds on these previous studies and investigates the

relationship between the shear stress generated by conventional sparging and novel sparging approach on fouling control.

2. LITERATURE REVIEW

In this chapter, the concepts of the membrane filtration process, transmembrane pressure, membrane fouling and shear stress are reviewed.

2.1 Membrane Filtration Process

During the filtration process, the membrane serves as a selective barrier that only allows the passage of certain constituents and will retain other constituents in the liquid. Referring to Figure 2-1, the influent to the membrane module is known as feed water (also known as feed stream). The liquid that passes through the semi-permeable membrane is known as permeate and the liquid containing the retained or rejected constituents is known as concentrate (also known as retentate, reject, or waste stream).

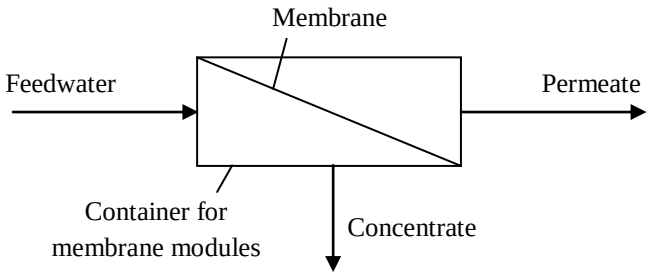

Figure 2-1. Definition sketch for a membrane process.

Membrane processes include microfiltration (MF), ultrafiltration (UF), nanoflitration (NF), reverse osmosis (RO), dialysis, and electrodialysis (ED) (Metcalf and Eddy, 2003). The first four membrane processes are commonly used in water and wastewater treatment and a hydraulic pressure provides the driving force. Dialysis involves the transport of constituents through a semi-permeable membrane on the basis of concentration differences. Electrodialysis involves the use of an electromotive force and ion-selective membranes to achieve the separation of charged ionic species. The focus of the following sections is on pressure-driven membrane processes. Table 2-1 illustrates the general characteristics of the four pressure driven membrane processes.

Table 2-1. General characteristics of membrane processes.

Membrane Process	Typical operating pressure, bar	Separation mechanism	Pore size	Typical operating range, μm	Typical constituents removed
Microfiltration	0.1-2	Sieve	Macropores (>50 nm)	0.08-2.0	TSS, turbidity, protozoan oocysts and cysts, some bacteria and viruses
Ultrafiltration	0.1-2	Sieve	Mesopores (2-50 nm)	0.005-2.0	Macromolecules, colloids, most bacteria, some viruses, proteins
Nanofiltration	4-20	Sieve + solution/ diffusion +exclusion	Micropores (<2 nm)	0.001-0.01	Small molecules, some hardness, viruses
Reverse osmosis	10-30	Sieve + solution/ diffusion +exclusion	Dense (< 2 nm)	0.0001-0.001	Very small molecules, color, hardness, sulphates, nitrates, sodium, other ions

Membranes used for water and wastewater application can be made from a number of organic and inorganic materials. Organic membranes are typically made of synthetic polymers such as polyvinylidene difluoride (PVDF), polyethylsulfone (PES), polyethylene (PE) and polypropylene (PP) (Judd, 2006). Inorganic membranes such as ceramic and metallic membranes have been used, although they are not as commonly used as organic membrane. One reason is that the cost of inorganic membranes can be up to ten times higher than that of the organic membrane (Owen *et al*., 1995). However, inorganic membrane can usually tolerate higher temperatures, higher pressure and harsher chemical conditions associated with the feed water or cleaning solutions.

2.2 Membrane Performance

The driving force for membrane filtration is the transmembrane pressure (TMP), defined as the difference between the feed water pressure and the permeate pressure:

$$TMP = P_{feed} - P_{permeate} = \Delta P \qquad (2\text{-}1)$$

Referring to the figure 1-1, the permeate flow obtained during filtration can be described by Darcy's Law (Belfort *et al*., 1994):

$$Q = \frac{(\Delta P - \Delta\pi)A}{\mu R_T} \qquad (2\text{-}2)$$

where Q [m^3 s^{-1}] is the permeate flow rate through the membrane surface, ΔP [Pa] is the TMP, $\Delta\pi$ [Pa] is the osmotic pressure of the solution, A [m^2] is the membrane area, μ [Pa s] is the solution viscosity and R_T [m^{-1}]is the total membrane resistance to the permeate flow. For a dilute solution, the osmotic pressure of the retained material can be calculated using the van't Hoff equation (Belfort *et al*, 1994):

$$\Delta\pi = \frac{vcRT}{M} \qquad (2\text{-}3)$$

where *v* [dimensionless] is the molar fraction of species, c [g L^{-1}] is the solute concentration, R [Pa L mol^{-1} K^{-1}] is the universal gas constant, T [K] is the temperature and M [g mol^{-1}] is the molecular weight of the solute. In microfiltration and ultrafiltration, the molecular weight of the solute in the feed water is usually high as they colloidal in size. As a result, the osmotic pressure is typically negligible in MF and UF.

Viscosity is an important parameter that will affect the performance of the membrane. In wastewater treatment applications, the viscosity of activated sludge can be characterized as shear-thinning and non-Newtonian (Seyssiecq *et al.*, 2003). In water treatment applications, the viscosity of solution is typically similar to that of pure water. Temperature, which significantly affects viscosity, is therefore an important parameter affecting the performance of membranes systems.

The total membrane resistance (R_T) to the permeate flow is the sum of intrinsic membrane resistance and the resistance due to fouling. Membrane fouling is defined as a "process resulting in loss of performance

of a membrane due to the deposition of suspended or dissolved substances on its external surfaces, at its pore openings, or within its pores" (Koros *et al*., 1996). Overtime, as fouling increases and the resistance to the permeate flow becomes too high, the membrane must be physically and/or chemically cleaned to remove the accumulated foulants.

2.3 Membrane Fouling

Membrane fouling is an unavoidable consequence of membrane filtration. It causes an increase of resistance to the permeate flow, which leads to an increase in the TMP or a decrease in permeate flow over time.

2.3.1 Type of fouling

Membrane fouling in general can be divided into two categories – reversible and irreversible. Reversible fouling refers to the resistance that can be removed after hydraulic or chemical cleaning. The main cause of reversible fouling is the accumulation of retained material on the membrane surface or in the membrane pores.

Irreversible fouling is defined as the increase of membrane resistance that is permanent and cannot be removed, even after hydraulic and/or chemical cleaning. Irreversible fouling is caused by the formation of chemical precipitates and/or the permanent damage to the membrane surface due to the biological or chemical agents, which may result in permanent blockage of pores and changes to the membrane's physical/ chemical properties. The extent of irreversible fouling is dependent on the frequency of backwashing, as well as the strength of adhesion of the clogging particles and precipitates on the membrane surfaces (Chang *et al*., 2002). The focus of the remainder of the discussion in this literature review is on the hydraulically reversible fouling.

2.3.2 Particle blocking model

Hermans and Bredée (1935) proposed filtration laws to describe the accumulation of foulants on membranes. Gonsalves (1950) made a critical study of the physical models used to derive these laws. The accumulation of foulants was categorized into four filtration models, namely 1) complete pore

blocking model, 2) intermediate pore blocking model, 3) standard pore blocking model and 4) cake layer formation model. Figure 2-1 illustrates each type of model schematically.

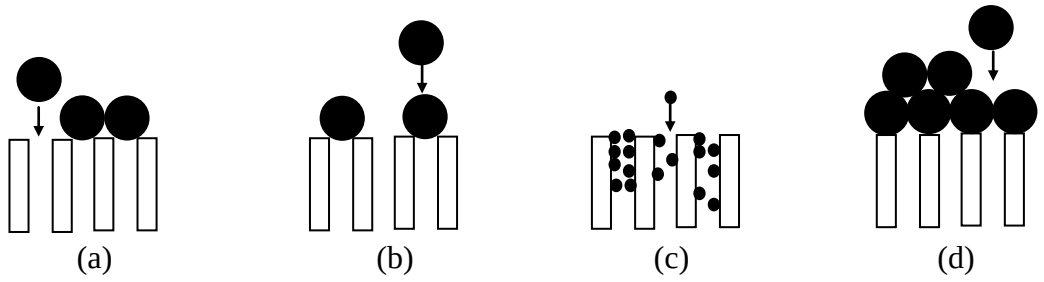

Figure 2-2. The four classical filtration models a) complete pore blocking b) intermediate pore blocking c) standard pore blocking d) cake layer formation.

In the complete pore blocking model, every particle can block one membrane pore when it reaches the membrane surface. This causes a decrease in the available pores and results in an increase in the resistance. In the intermediate pore blocking model, not all of the particles block the membrane pore. Some particles can overlap existing particles. As with partial pore blocking, the available pores is reduced. In the standard blocking model, small particles deposit/adsorb onto the membrane surface as well as on the inner walls of the membrane pores. The deposition/adsorption of the particles on the membrane walls decreases the pore diameter and results in an increase in the resistance. In the cake formation model, particles accumulate, forming a cake layer on the membrane surface and results in an increase in the resistance.

Hermia (1982) developed a mathematical model that describes the fouling of membranes base on the four filtration laws for the constant pressure filtration conditions. The characteristic form of the model is:

$$\frac{d^2t}{dV^2} = k_{i_n}\left(\frac{dt}{dV}\right)^n \qquad (2\text{-}4)$$

where the t [s] and V [m^3] are the filtration time and cumulative permeate volume, dt/dV is the inverse of the permeate flow rate and the rate of variation of the dt/dV with respect to filtrate volume V is defined as the resistance coefficient which is d^2t/dV^2. The n value is different for the different filtration laws: for complete blocking, n = 2; for standard blocking, n = 1.5; for intermediate blocking, n = 1; and for cake layer formation, n = 0. k_{i_n} is the blocking constant and is different for each filtration law.

For a constant flow and variable pressure systems, the Hermia's model yields equations 2-5 to 2-8 for the four different fouling laws.

Cake fouling:

$$P_t = P_0 + k_c V \qquad (2\text{-}5)$$

Intermediate blocking:

$$P_t = P_0 e^{k_i V} \qquad (2\text{-}6)$$

Standard blocking:

$$P_t = \frac{P_0}{(1 + \frac{1}{2} k_s V)^2} \qquad (2\text{-}7)$$

Complete blocking:

$$P_t = \frac{P_0}{1 - k_b V} \qquad (2\text{-}8)$$

where the P_t [Pa] is the TMP at time t and P_0 is the initial pressure, V is the filtered volume and k_c, k_i, k_s, and k_b are the four different blocking constant.

The Hermia's model was developed assuming dead-end filtration with no back transport. Field *et al*. (1995) modified the Hermia's model for the cake formation, intermediate blocking and complete blocking filtration laws, by assuming that under these three laws, the particle can transport back into the bulk solution as presented in equation 2-9.

$$-\frac{dJ}{dt} J^{n-2} = k_{i_n} (J - J^*) \qquad (2\text{-}9)$$

where the J [m^3 m^{-2} s^{-1}] is the permeate flux (dV/dt/A), J^* [m^3 m^{-2} s^{-1}] is the critical flux defined by Field *et al.* (1995) that fouling will not happen when the permeate flux below the critical flux and the k_{i_n} is the blocking constant for different filtration laws.

The back transportation of the particle has been suggested to occur predominantly due to three mechanisms for which models have been designed. In the shear-induced diffusion model, particles subjected to a shear flow randomly "bump into" and tumble over each other as well as the membrane

surface, resulting in net displacement of the particles away from the membrane surface (Zydney and Colton, 1986). In the inertial lift model, particles subjected to a laminar cross-flow velocity distribution near the membrane surface undergoes rotation, and reusling in a lateral movement away from the membrane due to the differential pressure induced by the velocity gradient of the rotating particles (Green and Belfort, 1980). The surface transport models suggest that the particle at the membrane surface roll along the surface due to tangential flow along the membrane surface (Beloft *et al*., 1994).

The three models suggest that particle back transport is strongly affected by the shear rate (as well as the particle size and concentration) (Beloft *et al*., 1994). However, the particle transport models were developed for constant laminar cross-flow conditions at a membrane surface. In a gas sparged membrane systems, the hydrodynamic conditions at the surface are highly variable and turbulent. Therefore, the above models cannot be applied directly to gas sparged membrane systems. Nonetheless, the models do suggest that particle back transport in gas sparged systems is likely to be affected by the share rate.

2.4 Air Sparging for Fouling Control

As previously discussed, shear rate is one of the critical parameters governing the particle transportation and enhancing permeate flux during membrane filtration. Shear rate is related to the viscosity and the shear stress at the membrane surface, which can be controlled by the temperature and the hydrodynamic conditions near the membrane. Gas spraging is typically used to induce favourable hydrodynamic conditions in the water and wastewater application.

The use of air sparging for fouling control in membrane processes has been gaining popularity over the past decade, particularly in the areas of drinking water production and biological wastewater treatment (i.e. membrane bioreactor) and macromolecular separation (Mercier-Bonin *et al*., 2003). Compared to cross-flow filtration (without air sparging), air sparging has been widely acknowledged to reduce the extent of fouling by 30 to 300%, depending on the applications, the operating conditions, membrane configuration (tubular, hollow fiber or flat sheet membranes) and the characteristics of the liquid being filtered (Bellara *et al*., 1996; Ueda *et al*., 1997; Bérubé and Lei, 2006; Cabassud *et al*., 1997; Cheng *et al*., 1998; Cui and Wright, 1994; Li *et al*., 1998).

Unconfined modules (e.g. submerged hollow fibers or flat sheet membranes) are those for which the membranes are submerged in the liquid to be filtered and then the membrane surfaces are scoured by sparged air bubbles. For these modules, the liquid typically permeates through the membrane in an outside-in flow configuration. Confined modules (e.g. tubular cross-flow membranes) are those for which the liquid to be filtered and sparged air bubbles are confined within the membrane. For these modules, the liquid typically permeates through the membrane in an inside-out flow configuration.

Although the surface shear stresses induced by a rising air sparged bubble in a confined vertical duct have been extensively characterized both numerically and experimentally, very limited research has focused on characterizing the hydrodynamics of air sparged bubbles in unconfined systems such as submerged flat sheet or hollow fiber membranes. This is in part due to the extremely complex nature of the geometry and flow path of air sparged bubbles in unconfined systems.

Some researchers have assumed that since the packing density of fibers in a submerged membrane system is relatively high, the shear stresses induced onto membrane surfaces by air-sparged bubbles rising between fibers is similar to that induced by an air slug in a confined system (Cui *et al*., 2003; Busch *et al*., 2007; Chang and Fane, 2000). However, the validity of this assumption is questionable given the complex and ever-changing nature of the hydrodynamic conditions in submerged hollow fiber membrane systems. In submerged hollow fiber membrane systems, the fibers are normally held loosely and typically sway extensively. This irregular fiber configuration continuously changes the flow path of rising air-sparged bubbles.

Bérubé *et al*. (2006) measured the shear stresses on the surface of hollow fibers in a submerged membrane system using a non-directional electrochemical probe. The frequency, duration and amplitude of the shear events were highly variable, and significantly different from the shear profiles of air slugs rising in a confined tubular system. Nagaoka *et al*. (2006) used a two-direction load sensor to record the shear stress profile acting over the entire length of the hollow fiber during gas sparging. Their reported profiles were similar to those observed by Bérubé *et al*. (2006), i.e. highly variable frequency, duration and amplitude of shear events. Yeo *et al*. (2006) used particle image velocimetry (PIV) to measure liquid velocities in an air sparged hollow fiber module. They observed that the axial velocities inside a hollow fiber module were up to ten times lower than those outside of the module where sparged air bubbles were introduced. This observation is similar to those of Bérubé *et al*. (2006) who suggested that *a tightly configured multi-fiber module could potentially shield certain areas of a fiber from both the*

bulk liquid flow and sparged gas bubbles. Fulton *et al.* (2011) used the electrochemical shear probe to map out the shear profile in a pilot scale submeraged hollow fiber membrane module. They found that the distributions of surface shear forces in the sytem were highly affected by the system geometry (e.g. module spacing, tank configuration and diffuser nozzle size). Chan *et al.* (2011) did a comprehensive study of the hydrodynamic conditions in the air sparged hollow fiber membrane modules. The effect of fiber tension, fiber packing density, sparging rate and the location of the aerator on the shear stress at the membrane surface within a bench-scale submerged hollow fiber system was investigated by using an electrochemical shear probe. Chan observed that increasing sparging rate increased both cross-flow velocity ('baseline shear') as well as the frequency of high shear events, while fiber tension and packing density affected both the ability of bubbles to penetrate and stay within the fiber bundle. The closer the bubble was to the membrane surface, the higher were the shear stress observed. In the study, using an electrochemical shear probe together with a high speed camera, they observed that the high shear events caused by the passage of bubbles in a multi-fiber system were approximately 0.02-0.1 seconds in duration. Their results also indicated that shear profiles at short duration and high frequency were preferred for fouling control than those of longer duration and low frequency. However, an optimal frequency was observed above which no additional benefit for fouling control could be observed.

2.5 Knowledge Gap and Research Objective

Base on the recent studies by Bérubé *et al.* (2006), Fulton *et al.* (2011) and Chan *et al.* (2011), air sparging can create different kinds of shear profiles in submerged hollow fiber systems, which will lead to different hydrodynamic conditions around the membrane and affect the fouling control efficiency. In addition, the shielding effect of the membrane bundle can reduce the shear stress inside the membrane. Chan *et al.* (2011) used a mechanical method to create different shear profiles in a bench-scale system and carried out several fouling testes under those conditions. The study by Chan *et al.* (2011) indicated that variable shear conditions were better than constant shear conditions for fouling control. However, in their study, the shear conditions were generated mechanically with an impeller, rater tan with air sparging in full-scale submerged membrane system.

The first objective of the present study is to generate the variable shear conditions identified by Chan *et al.* (2011) to be optimal for fouling control, by using gas sparging. The second objective of the present study is to confirm if these variable shear conditions do in fact result in optimal fouling control in an air

sparging system with full-scale hollow fibers. To achieve the objects, the shear profiles of different air sparging conditions are measured and analyzed by an electrochemical shear method, followed by the fouling test for the selected conditions.

3. MATERIALS AND METHODS

In the present thesis, both shear stress measurements and filtration tests were carried out. This chapter describes the experiment setups and programs used for the shear stress measurements and the filtration tests. In order to create similar conditions during shear stress measurements and filtration tests, similar experiment steups (i.e. membrane modules and air sparging apparatus) were used throughout the study.

3.1 Configuration of Membrane Modules

Since it was essential to create the comparable hydrodynamic conditions for the shear stress measurements and the filtration tests, the configuration of the modules needed to be similar for all experiments. In this section, details of the configurations of the modules, as well as the processes used to construct the modules, are presented.

3.1.1 Membrane modules used for shear stress measurements

The shear probes used in the experiments were similar to those used by Fulton *et al.* (2011). The principle of the shear probe method was presented in Appendix 1. Before the probes were used, they were calibrated as presented in a calibration process in Appendix 2 to 7. Refer to Fulton *et al.* (2011) for more details about the shear probe calibration procedure.

The module was constructed using two test fibers on to which shear probes had been installed as well as 48 full-length (1.8 m) inactive membrane fibers. The module was assembled using the following procedure.

1) Lay all the inactive 48 fibers and two test fibers closely together on a flat surface, as illustrated in Figure 3-1. The two test fibers were placed at the side of the fibers and shear probe was located at the middle of the modules. Electrical tape was used to fix both ends of all the inactive fibers and test fibers as presented in Figure 3-2.

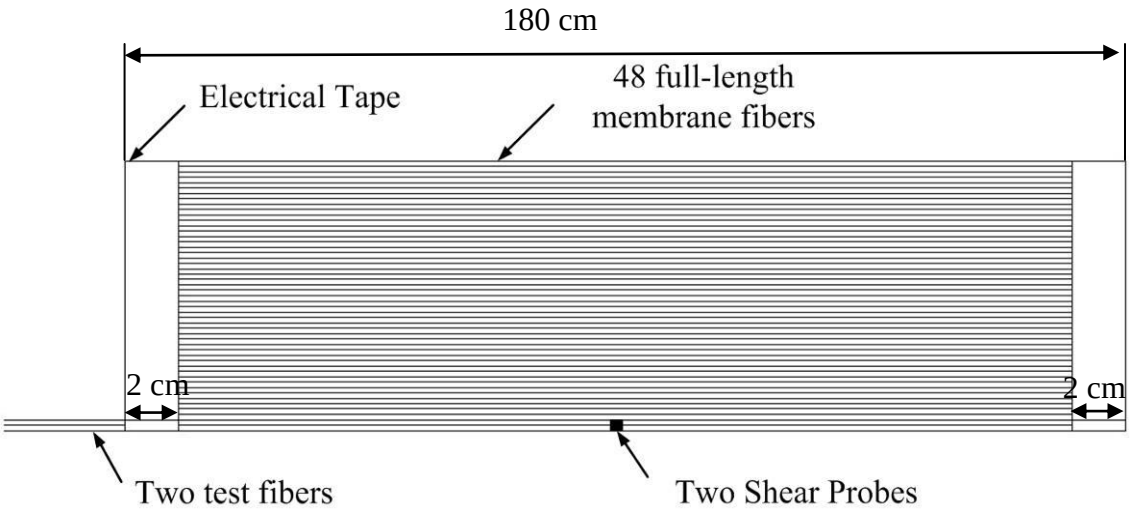

Figure 3-1. The top view of the fibers before roll up.

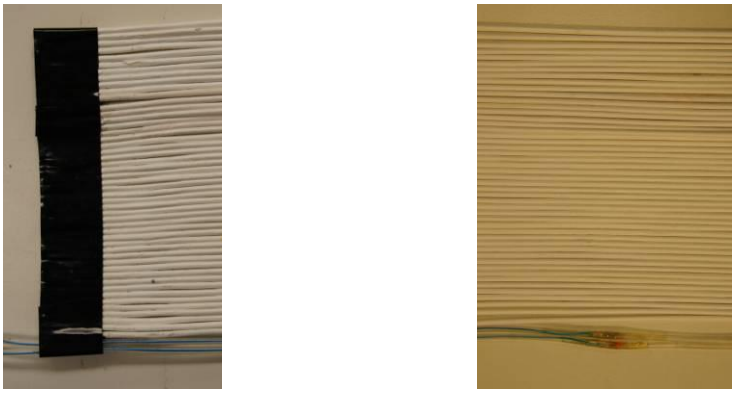

(a) (b)

Figure 3-2. (a) One end of the fiber pad with electrical tap. (b) The middle of the fiber pad with shear probes.

(2) Roll the inactive fibers and test fibers. Secure the ends using electrical tape. The Figure 3-3 and Figure 3-4 illustrates the rolled bundle.

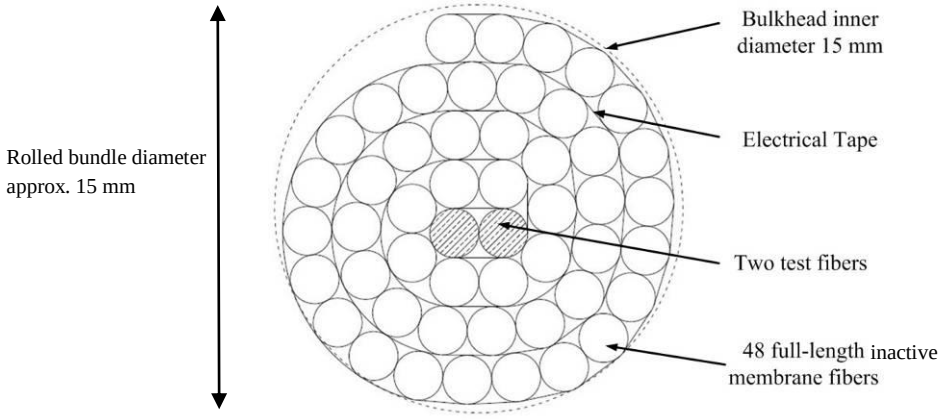

Figure 3-3. Cross-section view of the bundle.

(a)

(b)

(c)

Figure 3-4. (a) Image of the fiber bundle used for shear stress measurements. (b) Image of the top end of the bundle. (c) Image of bottom end of the bundle.

(3) Slide both ends of the bundle into the 15 mm inner diameter bulkheads. The bulkheads were made of PVC as the experiment requires a metal free environment except for the cathode and anode. Zip ties were used to secure the bundle to the bulkheads. Figure 3-5 illustrates the structure of the final membrane module used for shear stress measurements. The test fibers were placed at the center of the module to examine the potential shielding effects of fibers. The shear probes were placed at the middle of the test fibers, where maximum fiber sway is expected.

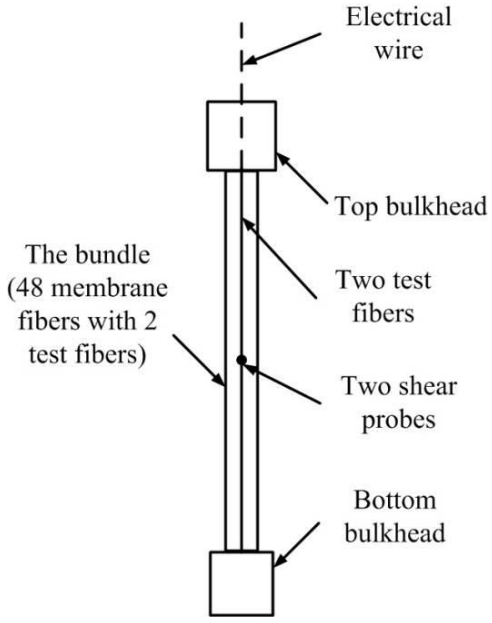

Figure 3-5. The structure of membrane module used for shear stress measurements.

3.1.2 Membrane module used for filtration tests

The configuration of the membrane module used for filtration tests was similar to that of the module used for shear stress measurements. However, instead of placing test fibers at the center of the module active membrane fibers were placed at this location.

Filtration was performed through these three active membrane fibers. The total filtration area for the three fibers was 0.0293 m^2. The end of the three active membrane fibers were potted into quarter inch plastic tubes as presented in Figure 3-6 and 3-7. Epoxy was used for potting the fibers into the tubes. The plastic tube at the top of the membrane fibers was connected to a peristaltic pump (Masterflex®) and a suction pressure was applied during the filtration. The plastic tube at the bottom of the fibers was sealed. Care was taken to keep the active membrane fibers wet during the entire procedure.

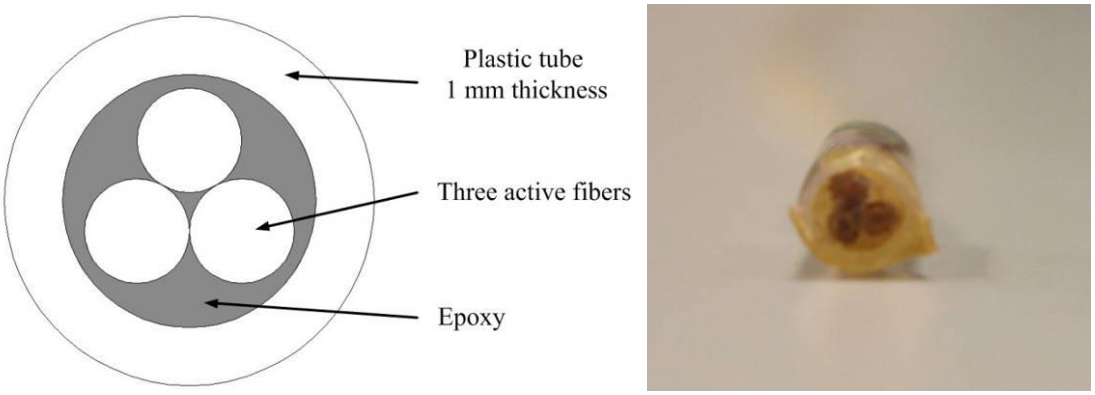

(a) (b)

Figure 3-6. (a) Cross-section view of the active membrane fibers. (b) Image of the section view of the active membrane fibers.

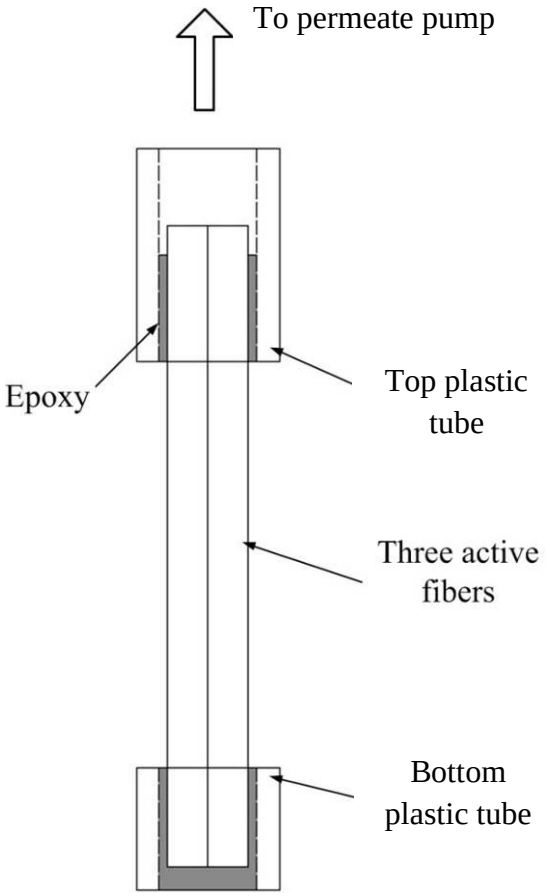

(a)

(b)

Figure 3-7. (a) Schematic of the active membrane fibers. (b) Image of the active membrane fibers.

The process to assemble the fiber bundle for the filtration tests was similar to that used to assemble the fiber bundle for the shear stress measurements. The major difference was that the bundle used for the shear stress measurements contained 50 fibers (2 test fibers + 48 inactive membrane fibers) while the bundle used for the filtration tests was only 40 fibers (3 active membrane fibers + 37 inactive membrane fibers). In both cases, the outer diameter of the bundle was approximately 15 mm. The active membrane fibers were incorporated into the modules as follows.

1) Lay all the 37 inactive fibers and the 3 active membrane fibers close together on a flat surface, fix both end of all the fibers using electrical tape as illustrated in figure 3-8.

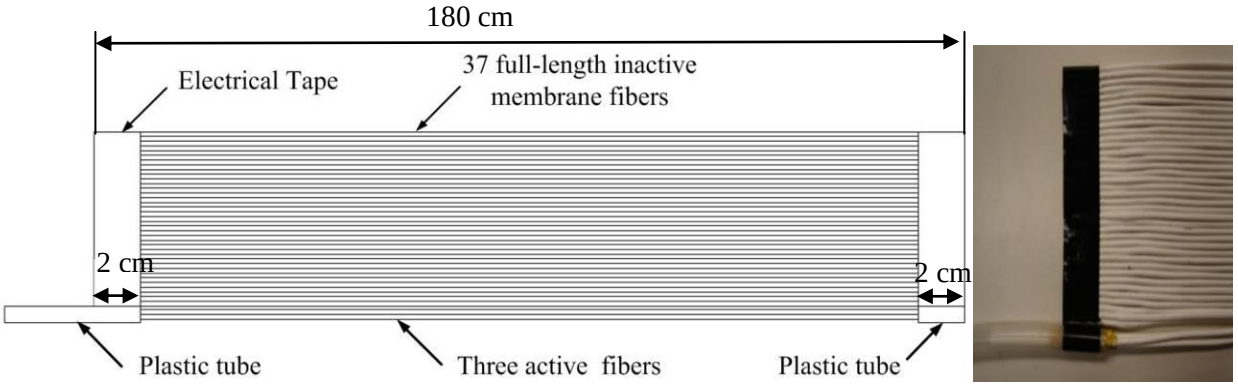

(a) (b)

Figure 3-8. (a) The top view of the fibers before roll up. (b) Image of one end of the fibers before roll up.

(2) Roll the 37 inactive fibers around the active membrane fibers as illustrated in Figure 3-9. Secure both ends using electrical tape.

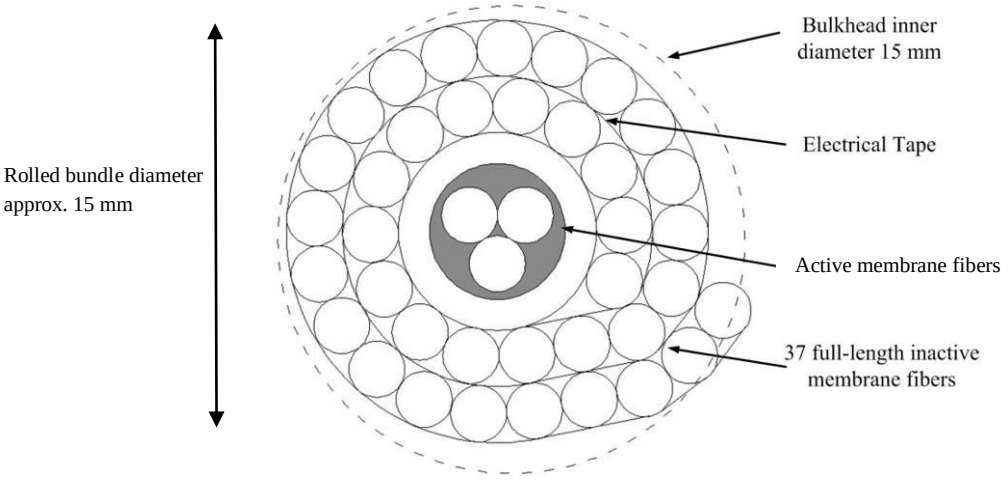

(a)

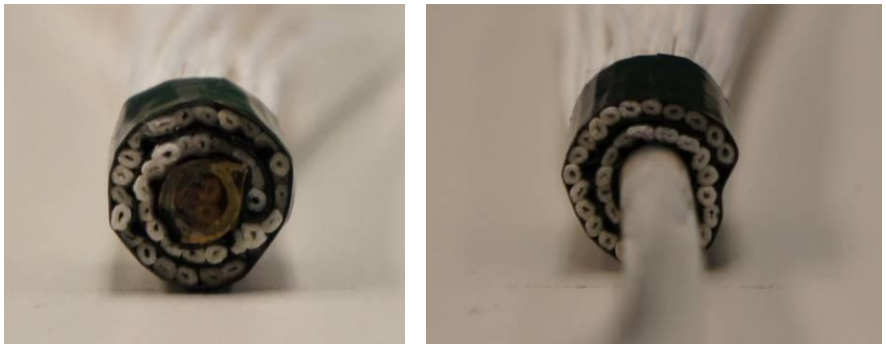

(b) (c)

Figure 3-9. (a) Cross-section view of the membrane bundle. (b) Image of bottom end of the bundle. (c) Image of the top end of the bundle.

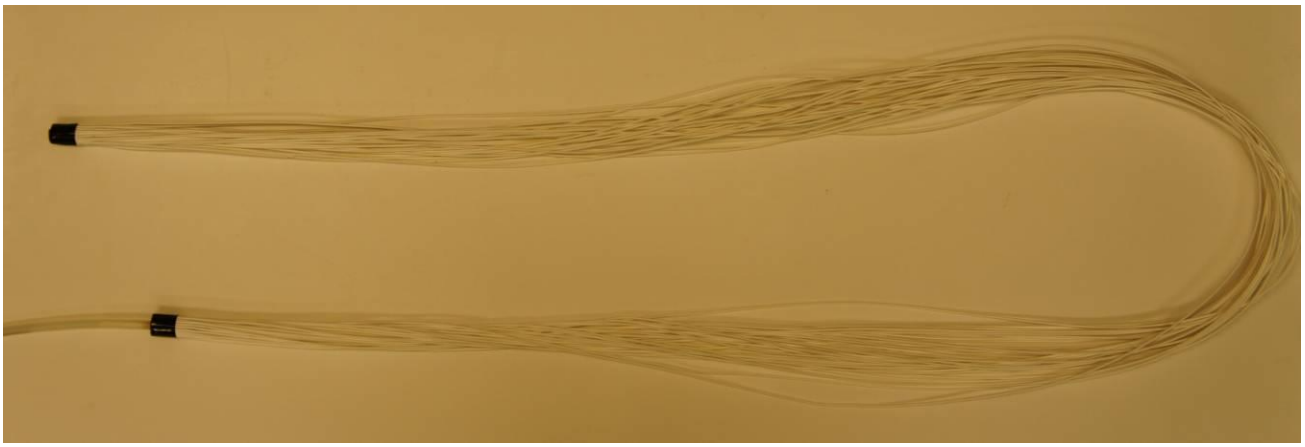

Figure 3-10. Image of the membrane bundles used for filtration tests.

(3) Slide both end of the bundle into the 15 mm inner diameter bulkheads and secure with zip ties as previously discussed. Figure 3-11 illustrates the structure of the membrane module used for the filtration tests. Care was taken to keep the active membrane fibers wet during the entire procedure.

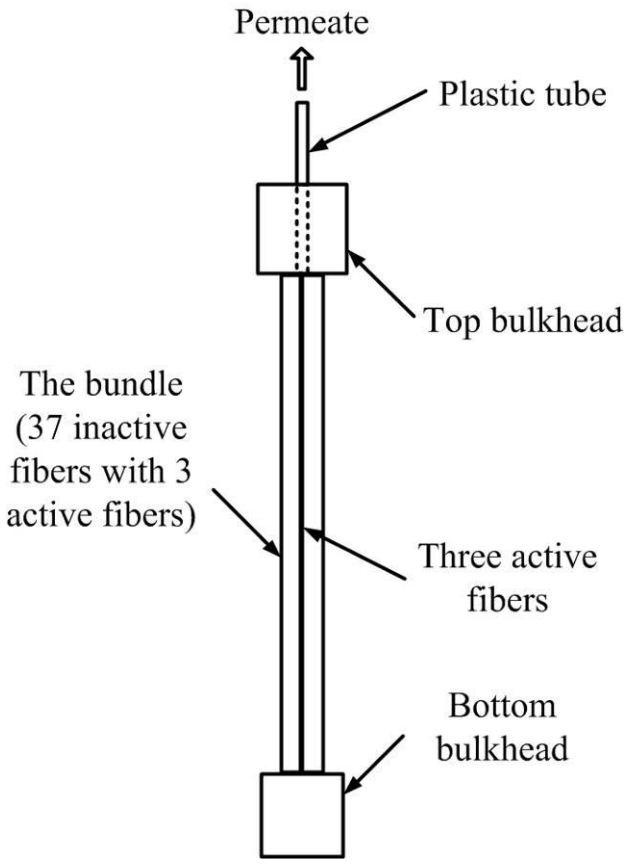

Figure 3-11. The structure of the membrane module used for filtration tests.

3.2 Experimental Apparatus

A similar experimental apparatus was used for both the shear stress measurements and the filtration tests as presented in the following sections.

3.2.1 Experimental apparatus for shear stress measurements

The overall system used for the shear stress measurements is presented in Figure 3-12.

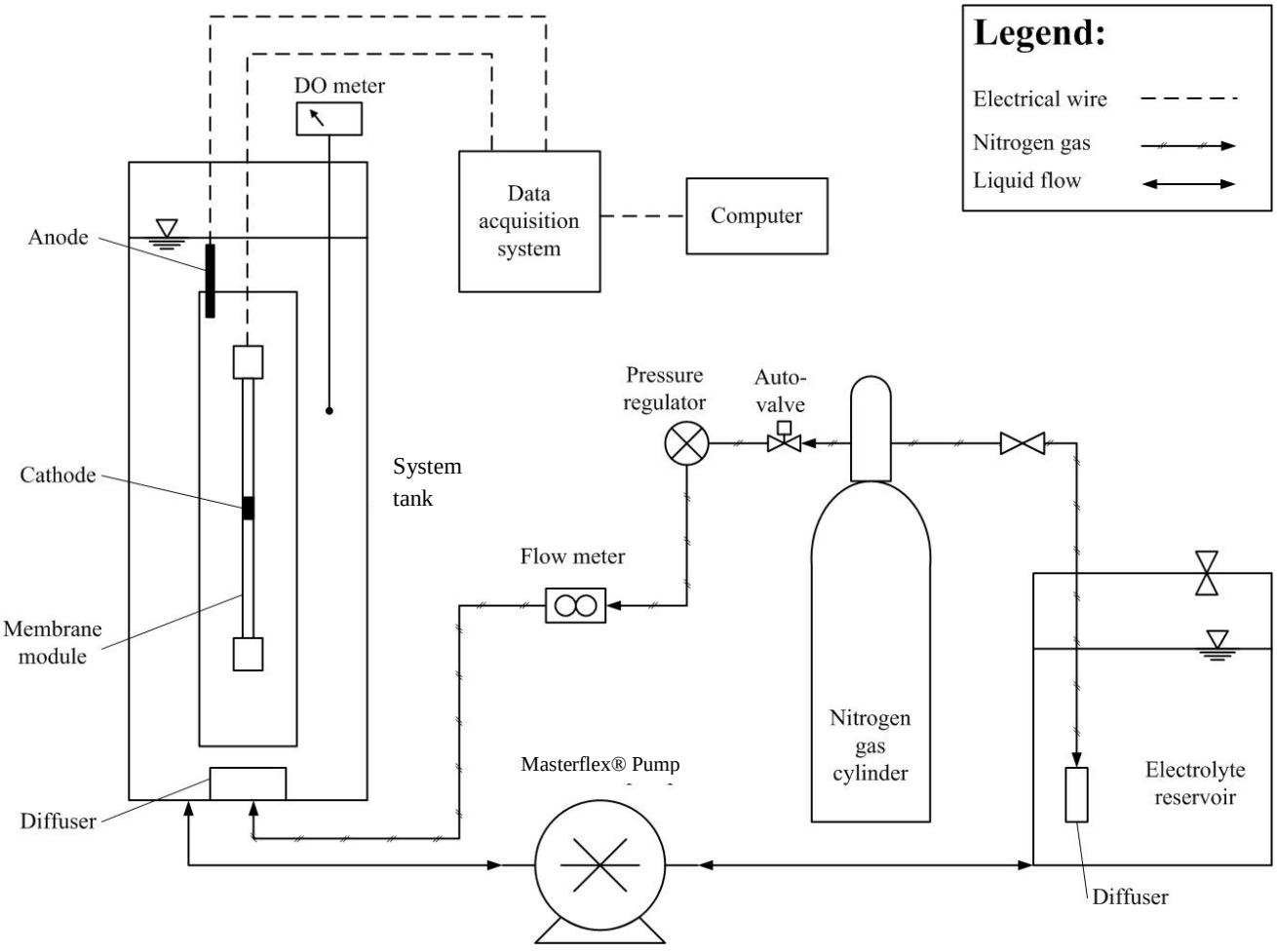

Figure 3-12. The schematic diagram of the shear stress measurements apparatus.

The three types of diffusers used in the shear stress measurements were located at the bottom of the system tank (i.e. fine bubble diffuser, coarse bubble diffuser and pulse bubble diffuser). The fine bubble diffuser had 6 holes of 2 mm diameter each. The coarse bubble diffuser had only one 5 mm diameter hole. The total area of the holes for the above two diffusers were very close to each other so that when

the same flow rate was used, the velocity of air entering the sparging tank was the same for both diffusers. The third type of diffuser was a pulse bubble diffuser. This diffuser is a proprietary system from GE Water and Process Technology (i.e. LEAD system diffuser). This diffuser is able to generate large intermittently released bubbles. The configuration of the pulse bubble diffuser can be modified to generate bubbles of various sizes released at different frequencies. In the present study, two pulse bubble diffuser configurations were tested, one is fast pulse and another one is slow pulse. For similar gas flow rates, the frequency of bubble released from the fast pulse diffuser was approximately 2 times faster than that from the slow pulse diffuser.

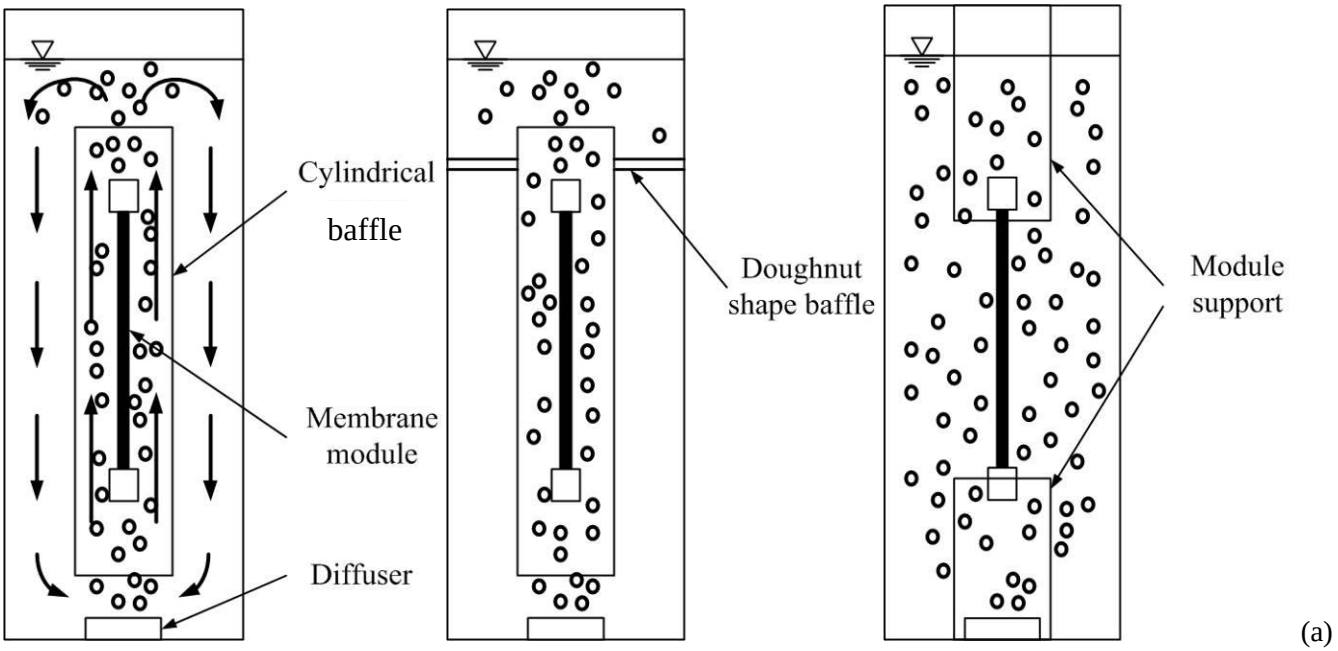

(a) Baffled cross-flow (b) Baffled stagnant (c) Unbaffled

Figure 3-13. Three different system tanks configuration.

Three types of system tanks configurations were used, as presented in Figure 3-13. The first type was the baffled cross-flow as presented in Figure 3-13a. For this configuration, a concentric open-ended cylindrical baffle (diameter 6.5 cm and length 200 cm) was placed in the system tank. This promoted convective flow in the system. The size of the tank was 14 cm in diameter and 260 cm in length. The liquid depth was 220 cm to fully cover the cylindrical baffle. Note that for this configuration the bubble created by the pulse diffuser was larger than the diameter of the cylindrical baffle, and as a result, the bubble behaved as a taylor type slug bubble. To prevent the bubble confinement, a larger system tank with 20 cm in diameter and 260 cm in length was constructed. The larger tank also had a concentric cylindrical baffle which was 14 cm in diameter and 200 cm in length. The larger tank was used only

with the pulse bubble diffuser. In the following discussion, the small tank (diameter 14 cm) will be referred as D14 tank and the larger tank (diameter 20 cm) will be referred as D20 tank. For some of the experiments, a doughnut shape baffled was added to the D14 tank as illustrated in Figure 3-13b to prevent convective flow and promote stagnant conditions. Comparison of the results with stagnant and cross-flow conditions of above two configurations enabled the assessment of the effect of convective flow. The third type of system tank configuration was an unbaffled D14 tank as illustrated in Figure 3-13c. For this configuration, the concentric cylindrical baffle was removed and the membrane module was simply fixed with top and bottom supports. This system tank configuration promoted stagnant conditions and also prevented large pulse bubbles from being confined by a cylindrical baffle.

Nitrogen gas was used for sparging. The flow to the diffusers was monitored using a flow meter and adjusted using a pressure regulator. For shear measurements, three flow rates, low flow rate, medium flow rate and high flow rate with 3500 mL/min, 6000 mL/min and 8000 mL/min respectively, were used in the D14 tank. In the D20 tank, only the low flow rate (3500 mL/min) was considered. All the flow rates were measured under a pressure of 15 psi. For conditions with convective flow (Figure 3-13a), the gas sparging generated a cross-flow in the system tank. The velocity of this cross-flow was estimated by dye testing (Table 3-1).

Table 3-1. Bulk liquid velocity under different air flow rates.

Gas flow rate (ml/min)	Bulk liquid flow rate (cm/s)	
	D14 tank	D20 tank
3500	43	18
6000	50	-
8000	58	-

Two intermittent sparging conditions were considered for the fine and coarse bubble diffusers. For fast intermittent conditions, the sparging flow was on for 3 seconds then off for 3 seconds. For slow intermittent conditions, the sparging flow was on for 6 seconds then off for 6 seconds.

For the shear stress measurements, the current between the anode and cathode was measured and recorded using the Labview® software, similar to that used for the side loop setup in appendix 1. The sampling time was 1 minute for each experimental condition investigated. The cathode was the shear probe located on the test fiber at the center of the membrane module and the anode was located in the system tank with much larger surface area to ensure that the limiting current conditions was achieved.

DO meter was used to measure the dissolve oxygen in system tank and the temperature was also monitored.

The electrolyte solution used for the shear measurement experiments had the same compositions (0.003 M ferricynaide, 0.006 M ferrocyanide and 0.3 M potassium chloride) as that used for the shear calibration in appendix 1. The electrolyte was stored in the reservoir before the experiments as presented in Figure 3-12. Nitrogen gas and a fine diffuser were used to purge the oxygen out of the solution as the experiment required an oxygen free environment. Peristaltic pump (Masterflex®) was used to transfer the electrolyte between the system tank and the reservoir.

The membrane module was located at the center of the system tank. The slackness of the fiber bundle was defined as follows:

$$\text{Bundle slackness} = \left(1 - \frac{\text{Distance between two bulkheads}}{\text{Length of the fiber}}\right) \times 100\% \qquad (3\text{-}1)$$

In the D14 tank, two bundle slackness, 1.3% and 2.2% were used. In the D20 tank, only 1.3% slackness was used.

3.2.2 Experimental apparatus for filtration tests

The overall systems used for the filtration tests are presented in Figure 3-14 and Figure 3-15.

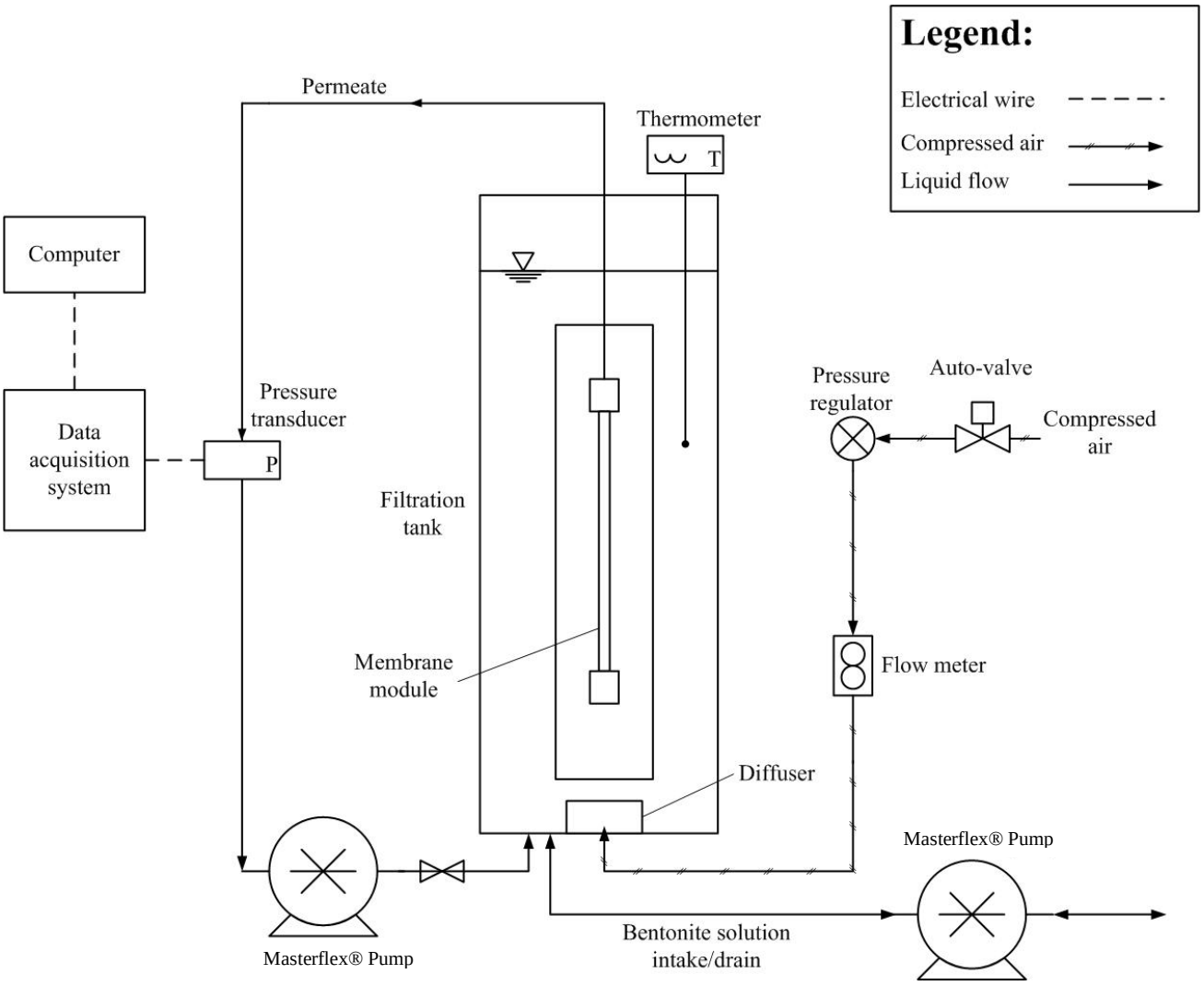

Figure 3-14. Filtering mode of the filtration setup.

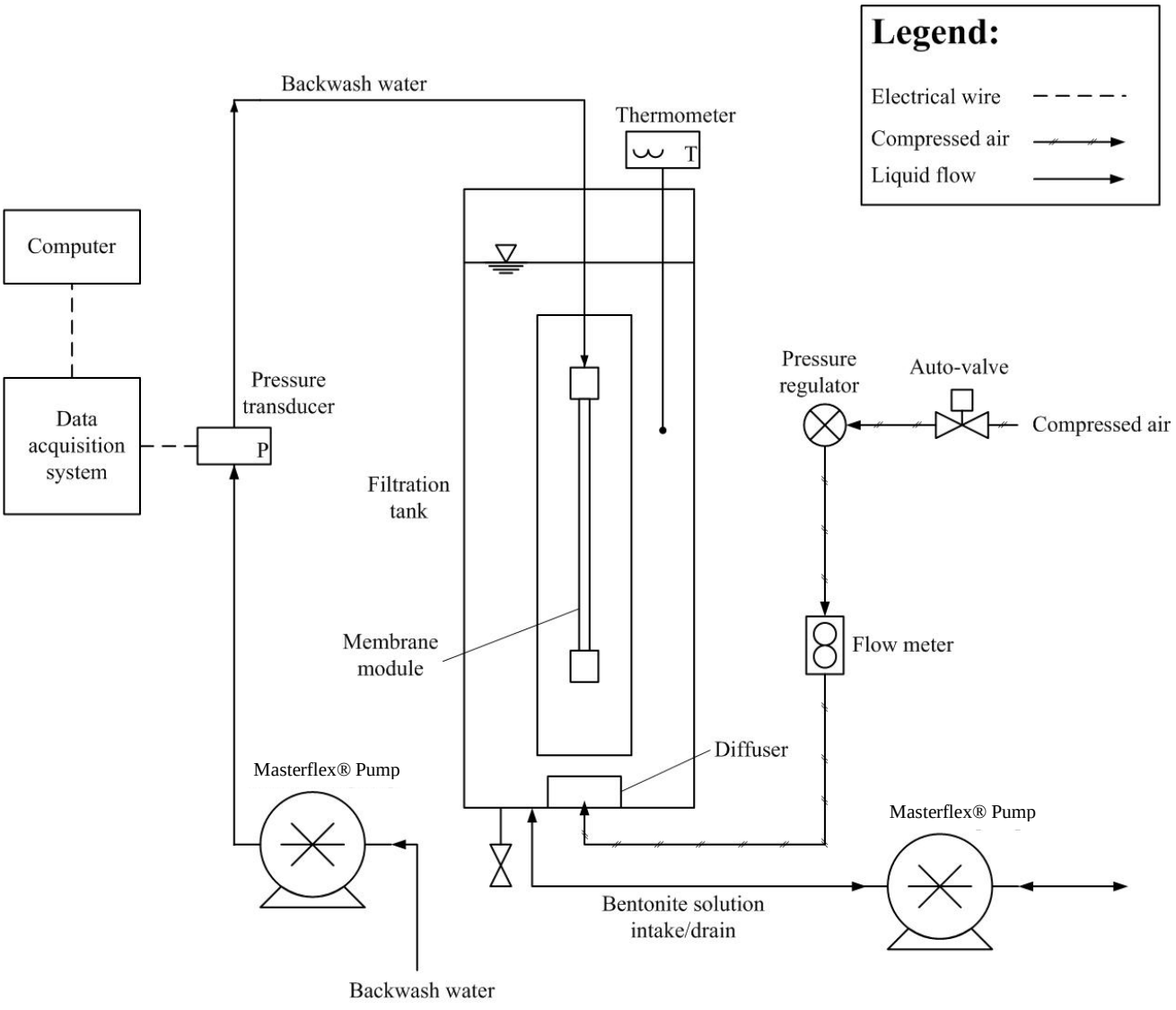

Figure 3-15. Backwash mode of the filtration setup.

The two types of diffusers used in the filtration tests were located at the bottom of the system tank (i.e. coarse bubble diffuser and pulse bubble diffuser), and were the same diffusers as those used during the shear stress measurements. For the pulse bubble diffuser, both fast and slow pulse configurations were investigated.

Two types of system tanks configurations were used as presented in Figure 3-13a and Figure 3-13c. The baffled cross-flow system tank (Figure 3-13a) in filtration tests was only used for the D20 tank and the Unbaffled system tank was only used for D14 tank. The dimensions of the system tanks used during the filtration tests were identical as those used during the shear stress measurements.

Air was used for sparging. The flow to the diffusers was monitored using a flow meter and adjusted using a pressure regulator. In the D14 tank, two flow rates, 7000 mL/min and 3500 mL/min were used. In the D20 tank, three flow rates, 3500 mL/min, 1750 mL/min and 875 mL/min were used to investigate the effect of the coarse and pulse diffusers on membrane fouling.

Two intermittent sparging conditions were considered for the fine and coarse bubble diffusers. For the first condition, sparging flow was on for 3 seconds and off for 3 seconds (i.e. similar to the conditions used in shear stress measurements). For the second condition, sparging flow was on for 2 seconds and off for 2 seconds, to create a similar frequency as the slow pulse diffuser.

A bentonite solution was used as the feed water for the filtration tests. The concentration of bentonite was 250 mg/L and tap water was used to prepare the solution. A peristaltic pump (Masterflex®) was used to transfer the prepared solution or to drain the tank (Figure 3-14 and 3-15).

The membrane module use for the filtration tests (described in section 3.1.2) was also located at the center of the system tank. The bundle slackness was kept constant at 18%. The permeate side was connected to a permeate pump (Masterflex®) which created a vacuum during filtration (Figure 3-14). The vacuum pressure was measured using a pressure transducer and recorded using a Labview® software. The flow rate of the pump was set as 60 mL/min so that the permeate flux used in the experiment was 125 L/m^2/hour. Backwash was performed after every filtration test. During the backwash mode (Figure 3-15), the direction of the permeate pump (Masterflex®) was reversed and a lower flow rate was used so that the backwash pressure was kept below 3 psi. A thermometer was used to monitor the temperature in the system tank.

3.3 Experimental Program

Due to the limited time and resource, only selected combinations of the conditions mentioned in the previous section were considered. For the shear stress measurements, 54 different conditions using the D14 tank and 2 conditions using D20 tank were investigated. For the filtration tests, 4 conditions using the D14 tank and 6 conditions using D20 tank were investigated. All the experiment conditions investigated are summarized in Table 3-2 and 3-3.

Table 3-2. Experimental conditions investigated for shear stress measurements.

A) D14 Tank

Diffuser type	Gas flow rate	Tank setup	Bulk flow pattern	Gas flow pattern	Slackness (%)	Experiment name
Fine Diffuser (F)	3500 mL/min Low (L)	With baffle (W)	Cross-flow (C)	Continuous (C)	1.3	FLWCC1.3
			Stagnant (S)	Continuous (C)	1.3	FLWSC1.3
	6000 mL/min Medium (M)	With baffle (W)	Cross-flow (C)	Continuous (C)	1.3	FMWCC1.3
			Stagnant (S)	Continuous (C)	1.3	FMWSC1.3
	8000 mL/min High (H)	With baffle (W)	Cross-flow (C)	Continuous (C)	1.3	FHWCC1.3
			Stagnant (S)	Continuous (C)	1.3	FHWSC1.3
Coarse Diffuser (C)	3500 mL/min Low (L)	With baffle (W)	Cross-flow (C)	Continuous (C)	1.3	CLWCC1.3
				Fast alter (F)	1.3	CLWCF1.3
				Slow alter (S)	1.3	CLWCS1.3
			Stagnant (S)	Continuous (C)	1.3	CLWSC1.3
				Fast alter (F)	1.3	CLWSF1.3
				Slow alter (S)	1.3	CLWSS.13
		Without baffle (O)	Stagnant (S)	Continuous (C)	1.3	CLOSC1.3
					2.2	CLOSC2.2
				Fast alter (F)	1.3	CLOSF1.3
					2.2	CLOSF2.2
				Slow alter (S)	1.3	CLOSS1.3
					2.2	CLOSS2.2
	6000 mL/min Medium (M)	With baffle (W)	Cross-flow (C)	Continuous (C)	1.3	CMWCC1.3
				Fast alter (F)	1.3	CMWCF1.3
				Slow alter (S)	1.3	CMWCS1.3
			Stagnant (S)	Continuous (C)	1.3	CMWSC1.3
				Fast alter (F)	1.3	CMWSF1.3
				Slow alter (S)	1.3	CMWSS1.3
		Without baffle (O)	Stagnant (S)	Continuous (C)	1.3	CMOSC1.3
					2.2	CMOSC2.2
				Fast alter (F)	1.3	CMOSF1.3
					2.2	CMOSF2.2
				Slow alter (S)	1.3	CMOSS1.3
					2.2	CMOSS2.2
	8000 mL/min High (H)	With baffle (W)	Cross-flow (C)	Continuous (C)	1.3	CHWCC1.3
				Fast alter (F)	1.3	CHWCF1.3
				Slow alter (S)	1.3	CHWCS1.3
			Stagnant (S)	Continuous (C)	1.3	CHWSC1.3
				Fast alter (F)	1.3	CHWSF1.3
				Slow alter (S)	1.3	CHWSS1.3
		Without baffle (O)	Stagnant (S)	Continuous (C)	1.3	CHOSC1.3
					2.2	CHOSC2.2
				Fast alter (F)	1.3	CHOSF1.3
					2.2	CHOSF2.2
				Slow alter (S)	1.3	CHOSS1.3
					2.2	CHOSS2.2
Slow Pulse Diffuser (P)	3500 mL/min Low (L)	With baffle (W)	Cross-flow (C)	Continuous (C)	1.3	PLWCC1.3
			Stagnant (S)	Continuous (C)	1.3	PLWSC1.3
		Without baffle (O)	Stagnant (S)	Continuous (C)	1.3	PLOSC1.3
					2.2	PLOSC2.2
	6000 mL/min Medium (M)	With baffle (W)	Cross-flow (C)	Continuous (C)	1.3	PMWCC1.3
			Stagnant (S)	Continuous (C)	1.3	PMWSC1.3
		Without baffle (O)	Stagnant (S)	Continuous (C)	1.3	PMOSC1.3
					2.2	PMOSC2.2
	8000 mL/min High (H)	With baffle (W)	Cross-flow (C)	Continuous (C)	1.3	PHWCC1.3
			Stagnant (S)	Continuous (C)	1.3	PHWSC1.3
		Without baffle (O)	Stagnant (S)	Continuous (C)	1.3	PHOSC1.3
					2.2	PHOSC2.2

B) D20 Tank

Diffuser type	Gas flow rate	Tank setup	Bulk flow pattern	Gas flow pattern	Slackness (%)	Experiment name
Slow Pulse Diffuser (SP)	3500 mL/min Low (L)	With baffle (W)	Cross-flow (C)	Continuous (C)	1.8	SPLWCC1.8
Fast Pulse Diffuser (FP)	3500 mL/min Low (L)	With baffle (W)	Cross-flow (C)	Continuous (C)	1.8	FPLWCC1.8

Table 3-3. Experimental conditions investigated for filtration tests.

A) D14 Tank

Diffuser type	Gas flow rate	Tank setup	Bulk flow pattern	Gas flow pattern	Slackness (%)
Slow Pulse Diffuser	3500 mL/min	Without baffle	Stagnant	Continuous	1.8
Coarse Diffuser	3500 mL/min	Without baffle	Stagnant	Continuous	1.8
			Stagnant	3 sec on/off	1.8
	7000 mL/min	Without baffle	Stagnant	2 sec on/off	1.8

B) D20 Tank

Diffuser type	Gas flow rate	Tank setup	Bulk flow pattern	Gas flow pattern	Slackness (%)
Slow Pulse Diffuser	3500 mL/min	With baffle	Cross-flow	Continuous	1.8
	1750 mL/min	With baffle	Cross-flow	Continuous	1.8
	875 mL/min	With baffle	Cross-flow	Continuous	1.8
Coarse Diffuser	3500 mL/min	With baffle	Cross-flow	Continuous	1.8
	1750 mL/min	With baffle	Cross-flow	Continuous	1.8
	875 mL/min	With baffle	Cross-flow	Continuous	1.8

For the shear stress measurements, the procedure used was similar to that used for the calibration of the electrochemical probe. The detail procedure is presented in Appendix 8. Refer to Fulton *et al.* (2011) for more details. For the filtration tests, the experiment procedures were developed and presented in detail in Appendix 9 to ensure the stable performance of the membrane. Note that the performance of new fiber modules was very unstable during the first few filtration tests. This was likely due to the presence of residual glycerin. After approx. 4 filtration tests, the performance became stable. Results for the first few filtration tests with new fiber modules were not used in the analysis.

3.4 QA/QC

3.4.1 QA/QC for shear stress measurements

In order to generate reliable data, it was critical to do a proper calibration of the shear probes. Appendices 2 to 7 presents the full processes used to do the shear probe calibration. The shear probes were calibrated by the steady-state calibration approach at the beginning and at the end of the study to make sure the performance of the shear probe was stable. In addition, the voltage step calibration approach was carried out after every four shear stress measurements to monitor the performance of the shear probes. Other factors including temperature, oxygen content and gas flow rate were also monitored, to ensure good performance of the shear probes (Appendices 2 to 8).

For the shear stress measurements in the D14 tank, the experiments were repeated in duplicate, and for those in the D20 tank, the experiments were repeated in triplicate. The repeated data confirmed the reputability of the shear stress measurements. QA/QC results for shear stress measurements are presented in Appendix 10.

3.4.2 QA/QC for filtration tests

In order to generate reliable data, it was critical to do a proper calibration of the pressure transducer. The calibration results of the pressure transducer are presented in Appendix 10. In addition, the particle size distribution of bentonite solution was presented. Other factors including temperature, gas flow rate and integrity test were also monitored to ensure good performance of the filtration tests (Appendix 10).

For the filtration tests in the D14 tank, the experiments were repeated in triplicate, and for those in the D20 tank, the experiments were repeated in duplicate. The repeated data confirmed the reputability of the filtration tests. QA/QC results for filtration tests are presented in Appendix 10.

4. RESULTS AND DISCUSSIONS

4.1 Shear Stress Measurements Results

4.1.1 Shear stress measurements results for D14 tank experiments

A total of 54 experiments were performed using the D14 tank. Typical experimental results are presented in Figure 4-1.

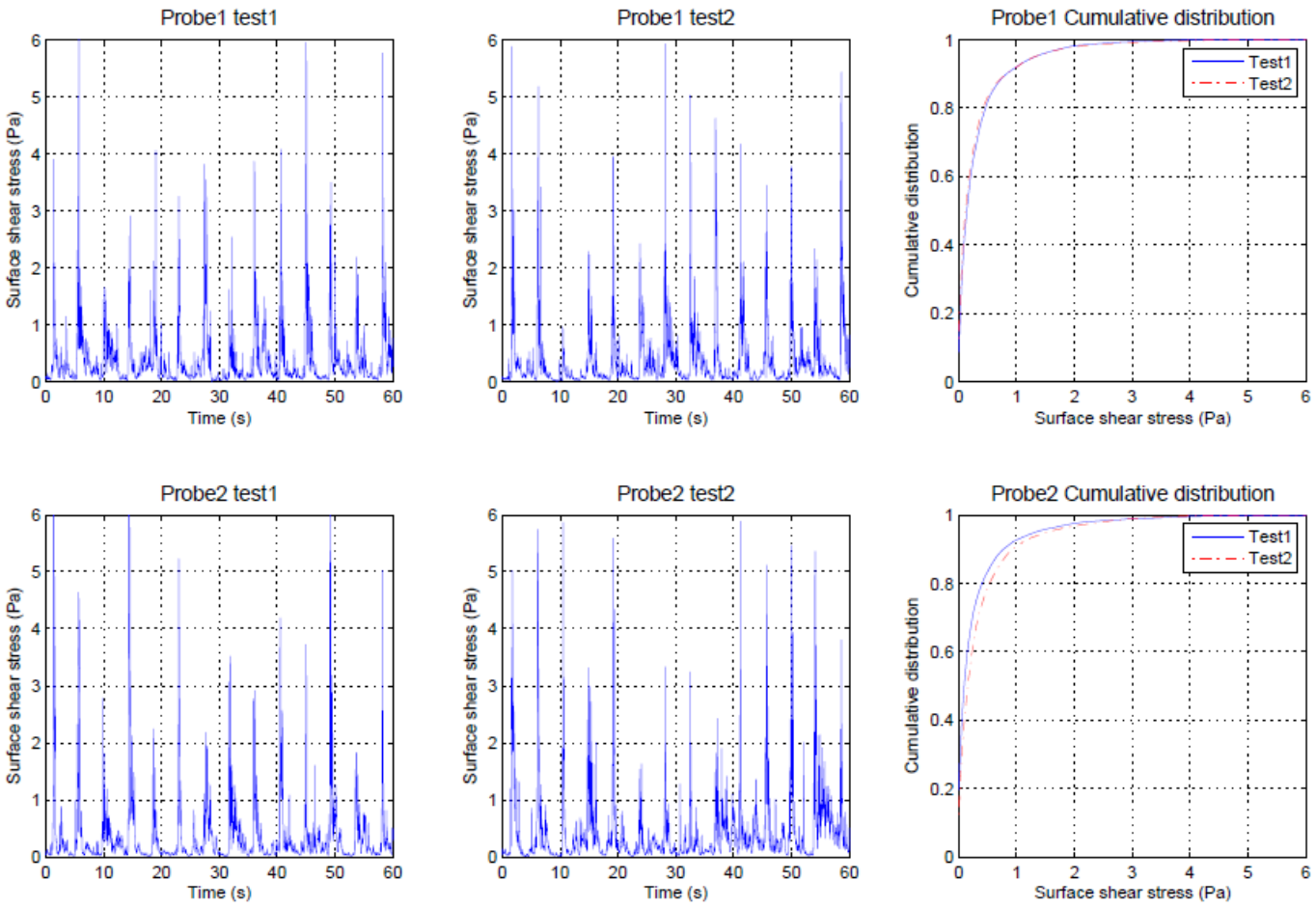

Figure 4-1. Shear stress measurements result of slow pulse diffuser, low gas flow rate, without baffle, stagnant, continuous gas flow and 1.3% slackness in D14 tank.

For each experimental condition, two duplicate tests were performed (test 1 and test 2). Cumulative distributions were used to compare the data between replicate tests. As presented in Figure 4-1, the

overlap of the cumulative distributions indicated that the results from the two experiments were similar. Results for all replicate experiments are presented in Appendix 11.

Although the relationship between surface shear stress and fouling control remain unclear, statistically significant correlations have been reported between the root mean square (RMS) of the surface shear stress over time induced by gas sparging and the extent of fouling in membrane systems (Yeo *et al*., 2006; Chan *et al*., 2011). For this reason, in the following discussion, the results are presented in terms of RMS. The RMS values for all 54 experiments are presented in Table 4-1. The RMS for all replicates are presented in Appendix 12.

Table 4-1. Shear stress measurements results of D14 tank experiments.

Diffuser type	Gas flow rate	Tank setup	Bulk flow pattern	Gas flow pattern	Slackness (%)	Experiment name	Shear stress (Pa)	
							RMS[1]	STD[2]
Fine Diffuser (F)	3500 mL/min Low (L)	With baffle (W)	Cross-flow (C)	Continuous (C)	1.3	FLWCC1.3	1.027	0.090
			Stagnant (S)	Continuous (C)	1.3	FLWSC1.3	0.797	0.095
	6000 mL/min Medium (M)	With baffle (W)	Cross-flow (C)	Continuous (C)	1.3	FMWCC1.3	1.614	0.171
			Stagnant (S)	Continuous (C)	1.3	FMWSC1.3	1.045	0.186
	8000 mL/min High (H)	With baffle (W)	Cross-flow (C)	Continuous (C)	1.3	FHWCC1.3	1.717	0.143
			Stagnant (S)	Continuous (C)	1.3	FHWSC1.3	1.275	0.123
Coarse Diffuser (C)	3500 mL/min Low (L)	With baffle (W)	Cross-flow (C)	Continuous (C)	1.3	CLWCC1.3	1.216	0.226
				Fast alter (F)	1.3	CLWCF1.3	0.904	0.106
				Slow alter (S)	1.3	CLWCS1.3	0.760	0.083
			Stagnant (S)	Continuous (C)	1.3	CLWSC1.3	0.909	0.082
				Fast alter (F)	1.3	CLWSF1.3	0.715	0.065
				Slow alter (S)	1.3	CLWSS.13	0.668	0.075
		Without baffle (O)	Stagnant (S)	Continuous (C)	1.3	CLOSC1.3	0.508	0.082
					2.2	CLOSC2.2	0.629	0.065
				Fast alter (F)	1.3	CLOSF1.3	0.482	0.095
					2.2	CLOSF2.2	0.536	0.043
				Slow alter (S)	1.3	CLOSS1.3	0.465	0.095
					2.2	CLOSS2.2	0.467	0.094
	6000 mL/min Medium (M)	With baffle (W)	Cross-flow (C)	Continuous (C)	1.3	CMWCC1.3	1.231	0.047
				Fast alter (F)	1.3	CMWCF1.3	1.035	0.087
				Slow alter (S)	1.3	CMWCS1.3	0.958	0.071
			Stagnant (S)	Continuous (C)	1.3	CMWSC1.3	1.170	0.169
				Fast alter (F)	1.3	CMWSF1.3	0.963	0.090
				Slow alter (S)	1.3	CMWSS1.3	1.014	0.129
		Without baffle (O)	Stagnant (S)	Continuous (C)	1.3	CMOSC1.3	0.589	0.093
					2.2	CMOSC2.2	0.701	0.118
				Fast alter (F)	1.3	CMOSF1.3	0.585	0.094
					2.2	CMOSF2.2	0.642	0.023
				Slow alter (S)	1.3	CMOSS1.3	0.584	0.139
					2.2	CMOSS2.2	0.631	0.109
	8000 mL/min High (H)	With baffle (W)	Cross-flow (C)	Continuous (C)	1.3	CHWCC1.3	1.430	0.074
				Fast alter (F)	1.3	CHWCF1.3	1.265	0.075
				Slow alter (S)	1.3	CHWCS1.3	1.139	0.019
			Stagnant (S)	Continuous (C)	1.3	CHWSC1.3	1.310	0.191
				Fast alter (F)	1.3	CHWSF1.3	1.058	0.194

Diffuser type	Gas flow rate	Tank setup	Bulk flow pattern	Gas flow pattern	Slackness (%)	Experiment name	Shear stress (Pa)	
							RMS[1]	STD[2]
Coarse Diffuser (C)	8000 mL/min High (H)	With baffle (W)	Stagnant (S)	Slow alter (S)	1.3	CHWSS1.3	1.168	0.122
		Without baffle (O)	Stagnant (S)	Continuous (C)	1.3	CHOSC1.3	0.755	0.099
					2.2	CHOSC2.2	0.814	0.060
				Fast alter (F)	1.3	CHOSF1.3	0.708	0.115
					2.2	CHOSF2.2	0.720	0.090
				Slow alter (S)	1.3	CHOSS1.3	0.605	0.034
					2.2	CHOSS2.2	0.714	0.078
Slow Pulse Diffuser (P)	3500 mL/min Low (L)	With baffle (W)	Cross-flow (C)	Continuous (C)	1.3	PLWCC1.3	0.997	0.091
			Stagnant (S)	Continuous (C)	1.3	PLWSC1.3	0.926	0.065
		Without baffle (O)	Stagnant (S)	Continuous (C)	1.3	PLOSC1.3	0.685	0.050
					2.2	PLOSC2.2	0.824	0.173
	6000 mL/min Medium (M)	With baffle (W)	Cross-flow (C)	Continuous (C)	1.3	PMWCC1.3	1.286	0.099
			Stagnant (S)	Continuous (C)	1.3	PMWSC1.3	1.002	0.188
		Without baffle (O)	Stagnant (S)	Continuous (C)	1.3	PMOSC1.3	0.840	0.030
					2.2	PMOSC2.2	0.910	0.041
	8000 mL/min High (H)	With baffle (W)	Cross-flow (C)	Continuous (C)	1.3	PHWCC1.3	1.464	0.035
			Stagnant (S)	Continuous (C)	1.3	PHWSC1.3	1.135	0.139
		Without baffle (O)	Stagnant (S)	Continuous (C)	1.3	PHOSC1.3	1.013	0.053
					2.2	PHOSC2.2	0.857	0.095

[1]RMS value presented is the average from the four experiments (duplicates from Probe 1 and 2).

[2]STD is calculated from the four RMS mentioned in [1].

4.1.2 Shear stress measurements results for D20 tank experiments

2 experiments were performed using the D20 tank. Experiment results are presented in Figure 4-2 and 4-3. For each experimental condition, three replicate tests were performed (test 1, test 2 and test 3). Cumulative distributions were used to compare the data between replicate tests. As presented in Figure 4-2 and 4-3, the overlap of the cumulative distributions indicated that the results from the replicate experiments were similar.

The RMS values for the 2 experiments are presented in Table 4-1. The RMS for all replicates are presented in Appendix 12.

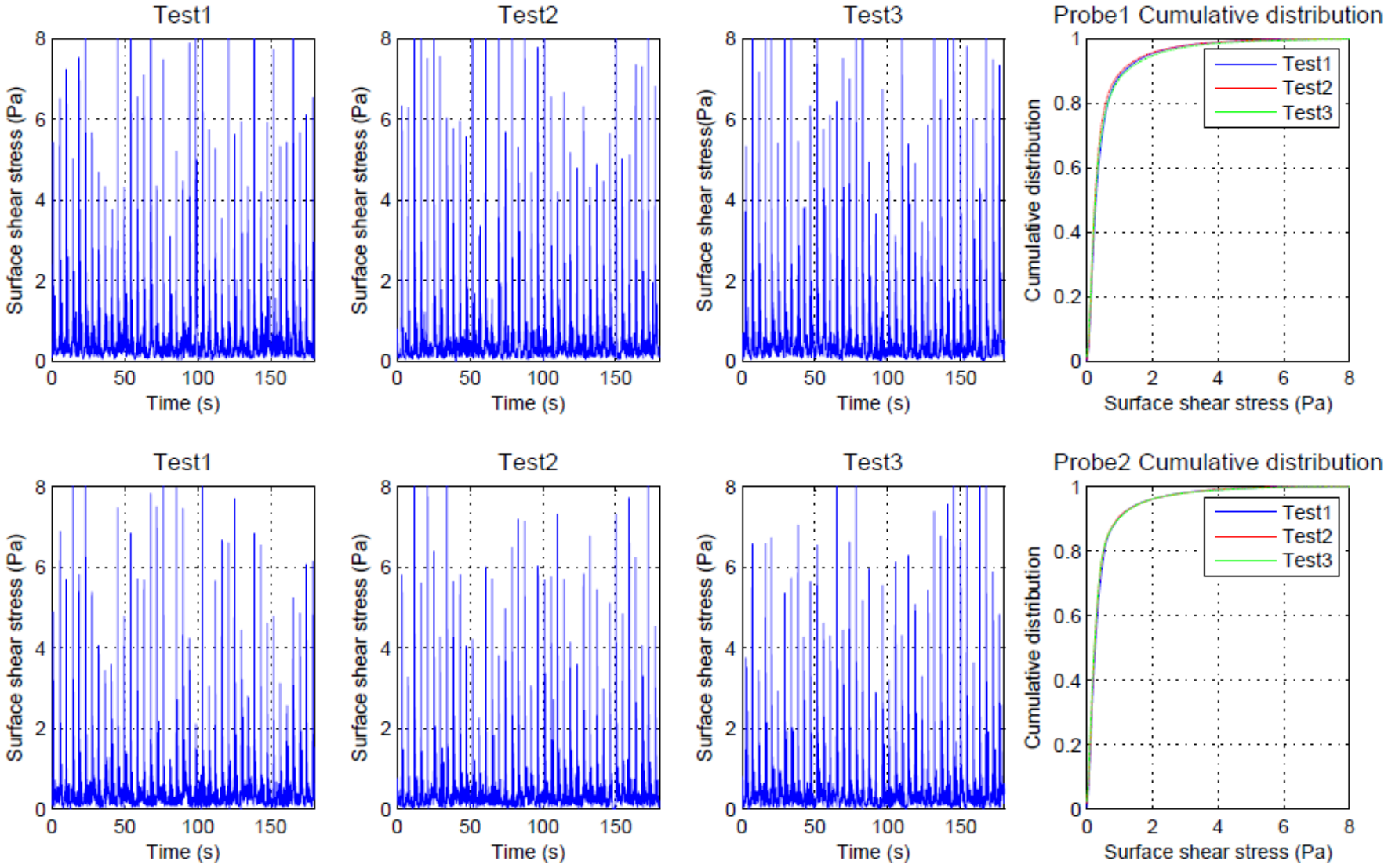

Figure 4-2. Shear stress measurements result of slow pulse diffuser, 3500 mL/min gas flow rate, with baffle, cross-flow, continuous gas flow and 1.8% slackness in D20 tank.

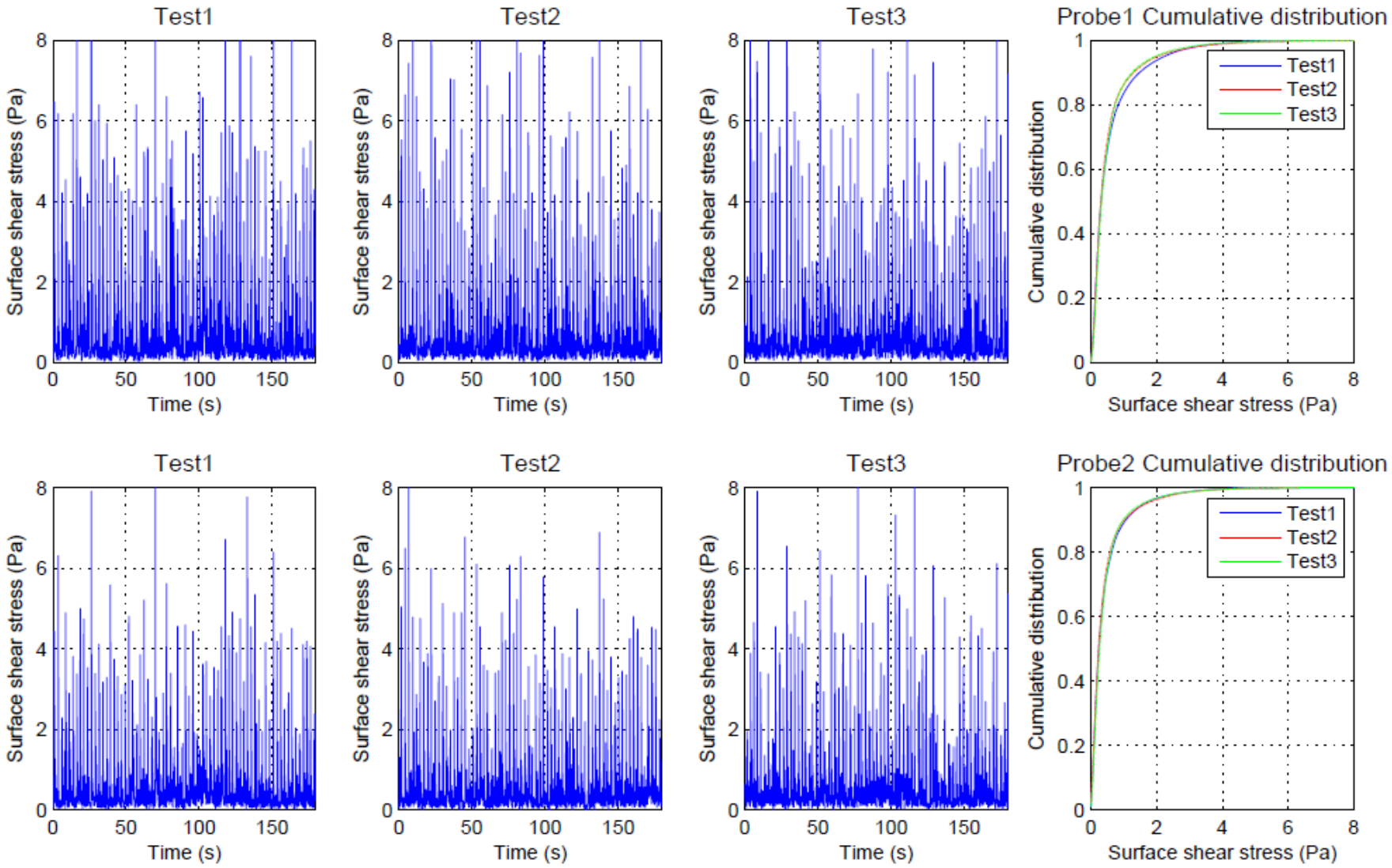

Figure 4-3. Shear stress measurements result of fast pulse diffuser, 3500 mL/min gas flow rate, with baffle, cross-flow, continuous gas flow and 1.8% slackness in D20 tank.

Table 4-2. Shear stress measurements results of D20 tank experiments.

Diffuser type	Gas flow rate	Tank setup	Bulk flow pattern	Gas flow pattern	Slackness (%)	Experiment name	Shear stress (Pa)	
							RMS[1]	STD[2]
Slow Pulse Diffuser (SP)	3500 mL/min Low (L)	With baffle (W)	Cross-flow (C)	Continuous (C)	1.8	SPLWCC1.8	0.916	0.072
Fast Pulse Diffuser (FP)	3500 mL/min Low (L)	With baffle (W)	Cross-flow (C)	Continuous (C)	1.8	FPLWCC1.8	0.883	0.112

[1]RMS value presented is the average from the six experiments (replicates from Probe 1 and 2).

[2]STD is calculated from the four RMS mentioned in [1].

4.2 Shear Stress Measurements Discussions

In the following sections, the effects of the different experimental conditions investigated on the RMS are compared.

4.2.1 Effect of diffuser type

4.2.1.1 Fine bubble diffuser vs. Coarse bubble diffuser

A total of 6 experimental condition sets were considered for which fine bubble and coarse bubble diffusers were used and all other experimental conditions were similar (Table 4-3). The data presented in Table 4-3 is summarized in Figure 4-4.

Table 4-3. Fine bubble diffuser vs. coarse bubble diffuser.

Series Number	Fine Bubble	Shear stress (Pa)		Coarse bubble	Shear stress (Pa)	
		RMS	STD		RMS	STD
1	FLWCC1.3	1.027	0.090	CLWCC1.3	1.216	0.226
2	FLWSC1.3	0.797	0.095	CLWSC1.3	0.909	0.082
3	FMWCC1.3	1.614	0.171	CMWCC1.3	1.231	0.047
4	FMWSC1.3	1.045	0.186	CMWSC1.3	1.170	0.169
5	FHWCC1.3	1.717	0.143	CHWCC1.3	1.430	0.074
6	FHWSC1.3	1.275	0.123	CHWSC1.3	1.310	0.191

(Note: Data presented is from Table 4-1 and/or Table 4-2)

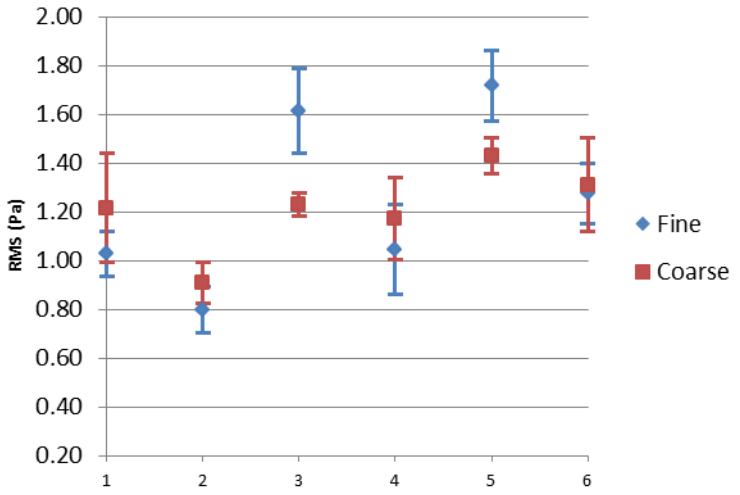

Figure 4-4. Fine bubble diffuser vs. coarse bubble diffuser (Error bar corresponds to the STD).

No consistent and statistically significant difference was observed between the RMS for fine bubble and coarse bubble diffusers. However, in general, the RMS was higher for the fine bubble diffuser than for the coarse bubble diffuser for conditions with the cross-flow and higher sparging rates. It is likely that the greater number of fine bubbles than coarse bubbles at a given gas sparging rate resulted in a higher entrained cross-flow velocities. However, the effect of the speed of cross-flow velocity on the RMS was not investigated as part of the present study.

4.2.1.2 Coarse bubble diffuser vs. Pulse bubble diffuser

A total of 12 experimental condition sets were considered for which coarse bubble and pulse bubble diffusers were used and all other experimental conditions were similar (Table 4-4). The data presented in Table 4-4 is summarized in Figure 4-5.

Table 4-4. Pulse bubble diffuser vs. coarse bubble diffuser.

Series Number	Pulse Bubble	Shear stress (Pa)		Coarse bubble	Shear stress (Pa)	
		RMS	STD		RMS	STD
1	PLWCC1.3	0.997	0.091	CLWCC1.3	1.216	0.226
2	PLWSC1.3	0.926	0.065	CLWSC1.3	0.909	0.082
3	PLOSC1.3	0.685	0.050	CLOSC1.3	0.508	0.082
4	PLOSC2.2	0.824	0.173	CLOSC2.2	0.629	0.065
5	PMWCC1.3	1.286	0.099	CMWCC1.3	1.231	0.047
6	PMWSC1.3	1.002	0.188	CMWSC1.3	1.170	0.169
7	PMOSC1.3	0.840	0.030	CMOSC1.3	0.629	0.093
8	PMOSC2.2	0.910	0.041	CMOSC2.2	0.701	0.118
9	PHWCC1.3	1.464	0.035	CHWCC1.3	1.430	0.074
10	PHWSC1.3	1.135	0.139	CHWSC1.3	1.310	0.191
11	PHOSC1.3	1.013	0.053	CHOSC1.3	0.755	0.099
12	PHOSC2.2	0.857	0.095	CHOSC2.2	0.814	0.060

(Note: Data presented is from Table 4-1 and/or Table 4-2)

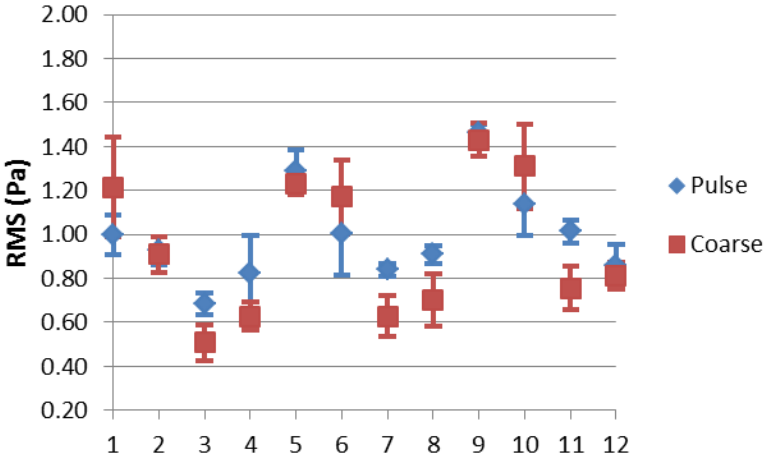

Figure 4-5. Pulse bubble diffuser vs. coarse bubble diffuser (Error bar corresponds to the STD).

No consistent and statistically significant difference was observed between the RMS for coarse bubble and pulse bubble diffusers. However, in general, the RMS was higher for the pulse bubble diffuser than for the coarse bubble diffuser when the system tank was operated with an unbaffled configuration (Figure 3-13c). This difference is likely due to the fact that without a baffle, the coarse bubbles were not confined to a zone that was close to the fibers and therefore could rise in the tank without contacting the fibers. On the other hand, the pulse bubbles were generally always in contact with the fibers. Typical results for coarse bubble and pulse bubble diffusers for the unbaffled system tank are presented in Figure 4-6.

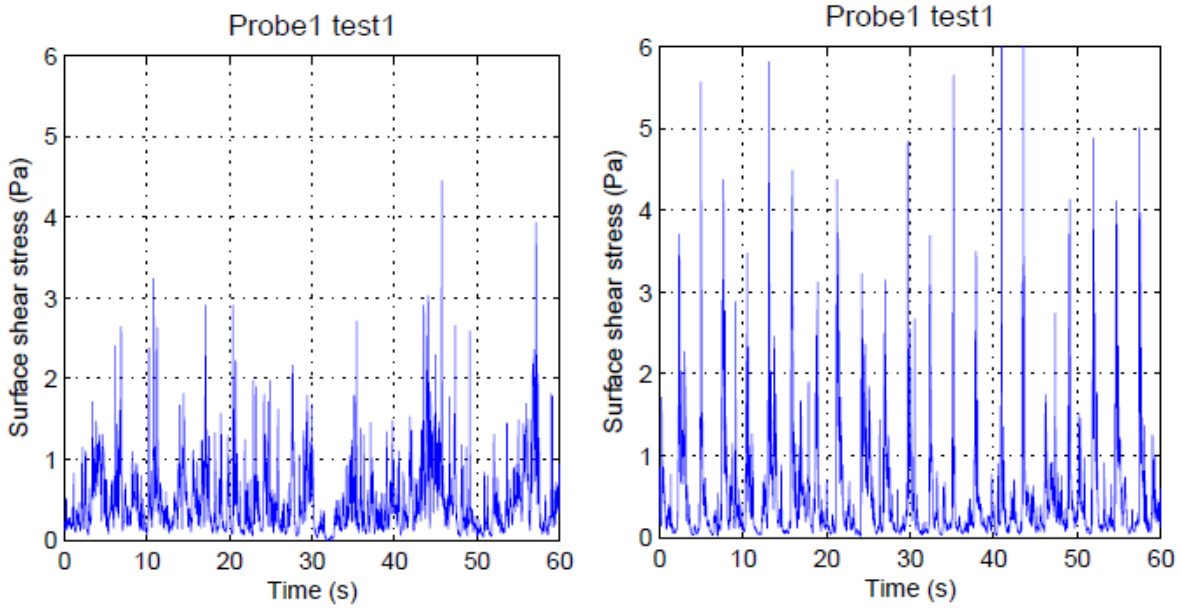

(a) (b)

Figure 4-6. (a) Probe1 test 1 shear profile of CMOSC1.3. (b) Probe1 test 1 shear profile of PMOSC1.3.

4.2.1.3 Slow pulse diffuser vs. Fast pulse diffuser

Only one experimental condition set was considered for which slow pulse and fast pulse diffusers were used and all other experimental conditions were similar (Table 4-5). The data presented in Table 4-5 is summarized in Figure 4-7.

Table 4-5. Slow pulse diffuser vs. fast pulse diffuser.

Series Number	Slow Pulse Diffuser	Shear stress (Pa)		Fast pulse diffuser	Shear stress (Pa)	
		RMS	STD		RMS	STD
1	SPLWCC1.8	0.916	0.072	FPLWCC1.8	0.883	0.112

(Note: Data presented is from Table 4-1 and/or Table 4-2)

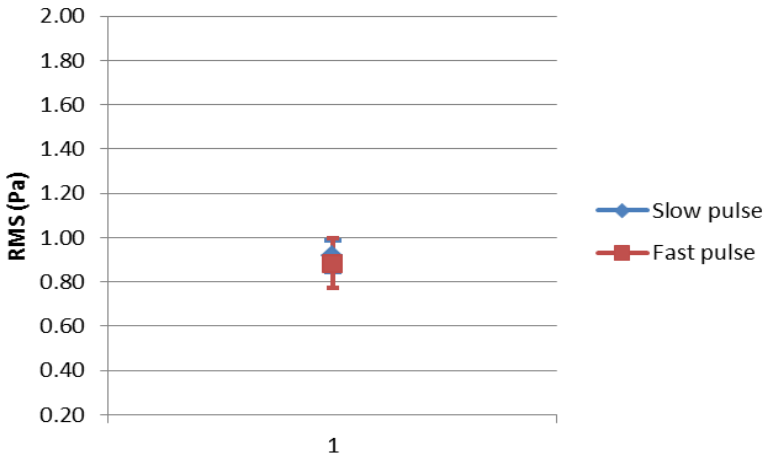

Figure 4-7. Slow pulse diffuser vs. fast pulse diffuser (Error bar corresponds to the STD).

No consistent and statistically significant difference was observed between the RMS for slow pulse and fast pulse diffusers. Ongoing research by others is investigating the effect of pulse bubble frequency on the RMS values.

4.2.2 Effect of system tank configuration

4.2.2.1 Baffled system tank v.s. Unbaffled system tank

A total of 12 experimental condition sets were considered for which baffled and unbaffled system tanks were used and all other experimental conditions were similar (Table 4-6). The data presented in Table 4-6 is summarized in Figure 4-8. For each series, all experimental conditions other than the tank setup are similar.

Table 4-6. Baffled vs. unbaffled system tank.

Series Number	Baffle	Shear stress (Pa)		Unbaffle	Shear stress (Pa)	
		RMS	STD		RMS	STD
1	CLWSC1.3	0.909	0.082	CLOSC1.3	0.508	0.082
2	CLWSF1.3	0.715	0.065	CLOSF1.3	0.482	0.095
3	CLWSS1.3	0.668	0.075	CLOSS1.3	0.465	0.095
4	CMWSC1.3	1.170	0.169	CMOSC1.3	0.629	0.093
5	CMWSF1.3	0.963	0.090	CMOSF1.3	0.585	0.094
6	CMWSS1.3	1.014	0.129	CMOSS1.3	0.584	0.139
7	CHWSC1.3	1.310	0.191	CHOSC1.3	0.755	0.099
8	CHWSF1.3	1.058	0.194	CHOSF1.3	0.708	0.115
9	CHWSS1.3	1.168	0.122	CHOSS1.3	0.605	0.034
10	PLWSC1.3	0.926	0.065	PLOSC1.3	0.685	0.050
11	PMWSC1.3	1.002	0.188	PMOSC1.3	0.840	0.030
12	PHWSC1.3	1.135	0.139	PHOSC1.3	1.013	0.053

(Note: Data presented is from Table 4-1 and/or Table 4-2)

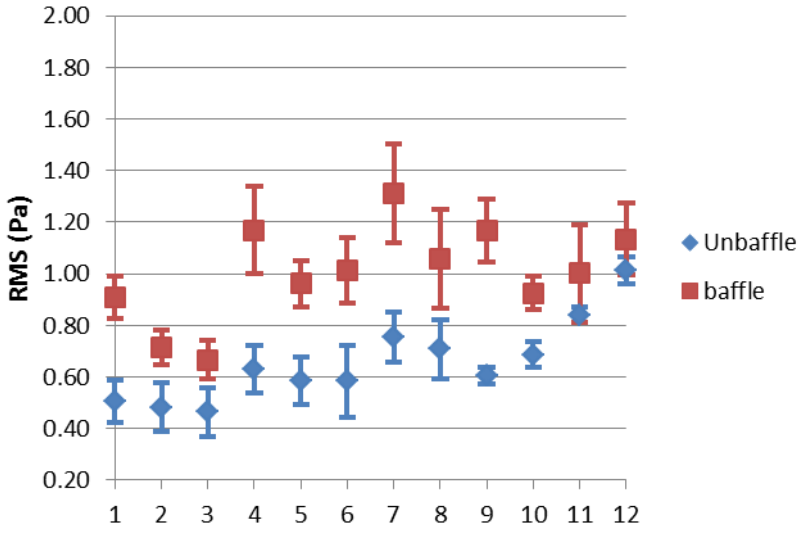

Figure 4-8. Baffle vs. unbaffle system tank (Error bar corresponds to the STD).

A consistant and generally statistically significant difference was observed between the RMS for baffled and unbaffled conditions. This was expected because the baffle confined thte sparged bubbles to a zone closer to the fibers, promoting greater contact between the bubbles and fibers.

4.2.2.2 Cross-flow vs. Stagnant

A total of 16 experimental condition sets were considered for which cross-flow and stagnant bulk liquid patterns were used and all other experimental conditions were similar (Table 4-7). The data presented in Table 4-7 is summarized in Figure 4-9.

Table 4-7. Cross-flow vs. stagnant.

Series Number	Cross-flow	Shear stress (Pa)		Stagnant	Shear stress (Pa)	
		RMS	STD		RMS	STD
1	FLWCC1.3	1.027	0.090	FLWSC1.3	0.797	0.095
2	FMWCC1.3	1.614	0.171	FMWSC1.3	1.045	0.186
3	FHWCC1.3	1.717	0.143	FHWSC.13	1.275	0.123
4	CLWCC1.3	1.216	0.226	CLWSC1.3	0.909	0.082
5	CLWCF1.3	0.904	0.106	CLWSF1.3	0.715	0.065
6	CLWCS1.3	0.760	0.083	CLWSS1.3	0.668	0.075
7	CMWCC1.3	1.231	0.047	CMWSC1.3	1.170	0.169
8	CMWCF1.3	1.035	0.087	CMWSF1.3	0.963	0.090
9	CMWCS1.3	0.958	0.071	CMWSS1.3	1.014	0.129
10	CHWCC1.3	1.430	0.074	CHWSC1.3	1.310	0.191
11	CHWCF1.3	1.265	0.075	CHWSF1.3	1.058	0.194
12	CHWCS.13	1.139	0.019	CHWSS1.3	1.168	0.122
13	PLWCC1.3	0.997	0.091	PLWSC1.3	0.926	0.065
14	PMWCC1.3	1.286	0.099	PMWSC1.3	1.002	0.188
15	PHWCC1.3	1.464	0.035	PHWSC1.3	1.135	0.139
16[1]	SPLWCC1.8	0.916	0.072	PLOSC2.2	0.824	0.173

(Note: Data presented is from Table 4-1 and/or Table 4-2)

[1]This condition set compared the different conditions between D14 and D20 tank. As D20 tank has a 14 cm diameter baffle, the effect of baffled (W) or unbaffled (O) tank setup is considered as similar.

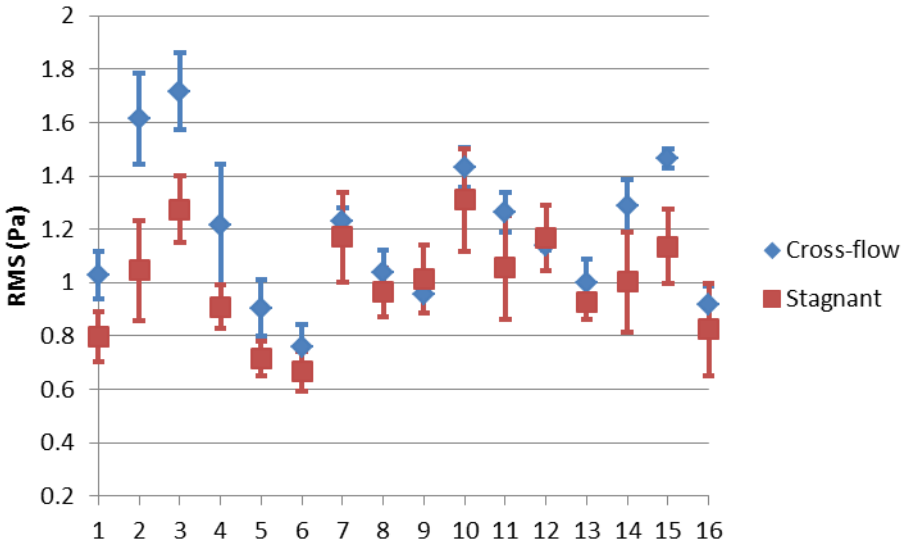

Figure 4-9. Cross-flow vs. stagnant (Error bar corresponds to the STD).

No consistent and statistically significant difference was observed between the RMS for cross-flow and stagnant bulk liquid. However, in general, the RMS was higher for the cross-flow than stagnant bulk liquid in most of the conditions. It is likely that, although the shear stresses generated by cross-flow are

relatively small compare to those generate by gas bubbles, they still contribute to the overall magnitude of the shear stresses.

4.2.3 Effect of gas flow rate

A total of 18 experimental condition sets were considered for which low, medium and high gas flow rates were used and all other experimental conditions were similar (Table 4-8). The data presented in Table 4-8 is summarized in Figure 4-10.

Table 4-8. Gas flow rate: low vs. medium vs. high.

Series Number	Low	Shear stress (Pa)		Medium	Shear stress (Pa)		High	Shear stress (Pa)	
		RMS	STD		RMS	STD		RMS	STD
1	FLWCC1.3	1.027	0.090	FMWCC1.3	1.614	0.171	FHWCC1.3	1.717	0.143
2	FLWSC1.3	0.797	0.095	FMWSC1.3	1.045	0.186	FHWSC.13	1.275	0.123
3	CLWCC1.3	1.216	0.226	CMWCC1.3	1.231	0.047	CHWCC1.3	1.430	0.074
4	CLWCF1.3	0.904	0.106	CMWCF1.3	1.035	0.087	CHWCF1.3	1.265	0.075
5	CLWCS1.3	0.760	0.083	CMWCS1.3	0.958	0.071	CHWCS.13	1.139	0.019
6	CLWSC1.3	0.909	0.082	CMWSC1.3	1.170	0.169	CHWSC1.3	1.310	0.191
7	CLWSF1.3	0.715	0.065	CMWSF1.3	0.963	0.090	CHWSF1.3	1.058	0.194
8	CLWSS1.3	0.668	0.075	CMWSS1.3	1.014	0.129	CHWSS1.3	1.168	0.122
9	CLOSC1.3	0.508	0.082	CMOSC1.3	0.629	0.093	CHOSC1.3	0.755	0.099
10	CLOSC2.2	0.629	0.065	CMOSC2.2	0.701	0.118	CHOSC2.2	0.814	0.060
11	CLOSF1.3	0.482	0.095	CMOSF1.3	0.585	0.094	CHOSF1.3	0.708	0.115
12	CLOSF2.2	0.536	0.043	CMOSF2.2	0.642	0.023	CHOSF2.2	0.720	0.090
13	CLOSS1.3	0.465	0.095	CMOSS1.3	0.584	0.139	CHOSS1.3	0.605	0.034
14	CLOSS2.2	0.467	0.094	CMOSS2.2	0.631	0.109	CHOSS2.2	0.714	0.078
15	PLWCC1.3	0.997	0.091	PMWCC1.3	1.286	0.099	PHWCC1.3	1.464	0.035
16	PLWSC1.3	0.926	0.065	PMWSC1.3	1.002	0.188	PHWSC1.3	1.135	0.139
17	PLOSC1.3	0.685	0.050	PMOSC1.3	0.840	0.030	PHOSC1.3	1.013	0.053
18	PLOSC2.2	0.824	0.173	PMOSC2.2	0.910	0.041	PHOSC2.2	0.857	0.095

(Note: Data presented is from Table 4-1 and/or Table 4-2)

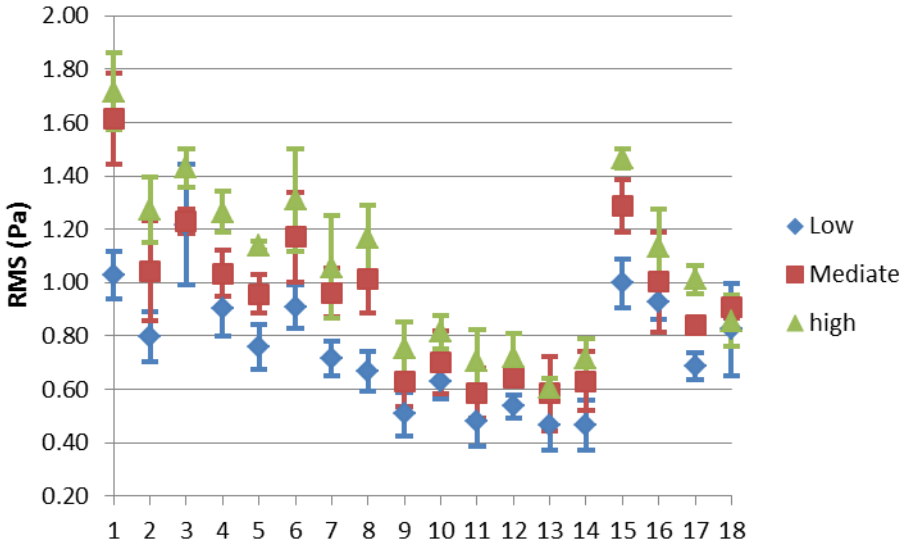

Figure 4-10. Gas flow rate: low vs. medium vs. high (Error bar corresponds to the STD).

No consistently and statistically significant difference was observed between the RMS for low, medium and high gas flow rate. However, for all conditions investigated, the RMS was generally highest for the high gas flow rate and lowest for the low gas sparging rate.

4.2.4 Effect of gas flow pattern

A total of 12 experimental condition sets were considered for which continuous, fast intermittent and slow intermittent were used and all other experimental conditions were similar (Table 4-9). The data presented in Table 4-9 is summarized in Figure 4-11.

Table 4-9. Gas flow pattern: continuous vs. fast intermittent vs. slow intermittent.

Series Number	Continuous	Shear stress (Pa)		Fast intermittent	Shear stress (Pa)		Slow intermittent	Shear stress (Pa)	
		RMS	STD		RMS	STD		RMS	STD
1	CLWCC1.3	1.216	0.226	CLWCF1.3	0.904	0.106	CLWCS1.3	0.760	0.083
2	CLWSC1.3	0.909	0.082	CLWSF1.3	0.715	0.065	CLWSS1.3	0.668	0.075
3	CLOSC1.3	0.508	0.082	CLOSF1.3	0.482	0.095	CLOSS1.3	0.465	0.095
4	CLOSC2.2	0.629	0.065	CLOSF2.2	0.536	0.043	CLOSS2.2	0.467	0.094
5	CMWCC1.3	1.231	0.047	CMWCF1.3	1.035	0.087	CMWCS1.3	0.958	0.071
6	CMWSC1.3	1.170	0.169	CMWSF1.3	0.963	0.090	CMWSS1.3	1.014	0.129
7	CMOSC1.3	0.629	0.093	CMOSF1.3	0.585	0.094	CMOSS1.3	0.584	0.139
8	CMOSC2.2	0.701	0.118	CMOSF2.2	0.642	0.023	CMOSS2.2	0.631	0.109
9	CHWCC1.3	1.430	0.074	CHWCF1.3	1.265	0.075	CHWCS.13	1.139	0.019
10	CHWSC1.3	1.310	0.191	CHWSF1.3	1.058	0.194	CHWSS1.3	1.168	0.122
11	CHOSC1.3	0.755	0.099	CHOSF1.3	0.708	0.115	CHOSS1.3	0.605	0.034
12	CHOSC2.2	0.814	0.060	CHOSF2.2	0.720	0.090	CHOSS2.2	0.714	0.078

(Note: Data presented is from Table 4-1 and/or Table 4-2)

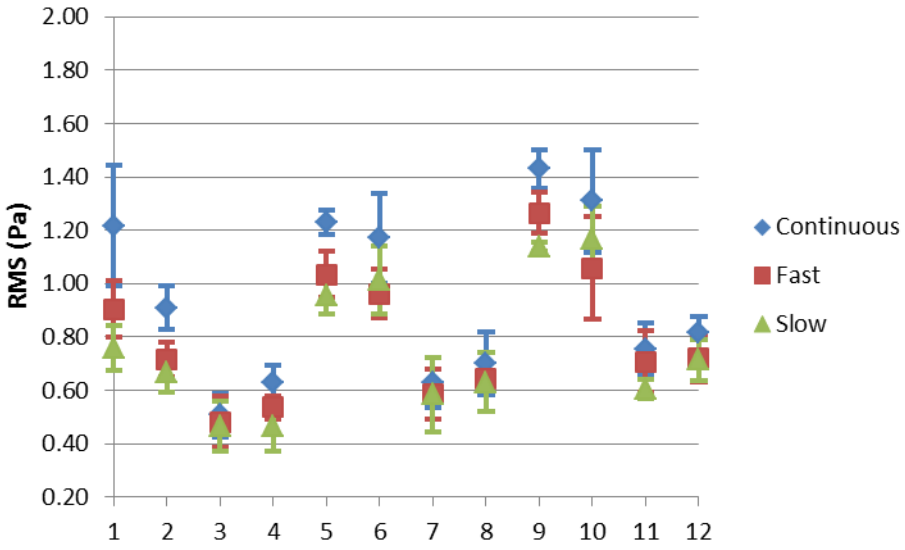

Figure 4-11. Gas flow pattern: continuous vs. fast intermittent vs. slow intermittent (Error bar corresponds to the STD).

No consistent and statistically significant difference was observed between the RMS for continuous, fast intermittent and slow intermittent gas flow pattern. However, in general, the RMS was higher for continuous than intermittent (fast and slow) gas flow pattern. This was expected since, at a given gas flow rate, because sparging flow is alterated between on and off, only half of the volume of gas is added to the system for intermittent compared to continuous gas sparging.

4.2.5 Effect of bundle slackness

A total of 12 experimental conditions were considered for which 1.3% and 2.2% bundle slackness were used and all other experimental conditions were similar (Table 4-10). The data presented in Table 4-10 is summarized in Figure 4-12.

Table 4-10. Bundle slackness: 1.3% vs. 2.2%.

Series Number	1.3%	Shear stress (Pa)		2.2%	Shear stress (Pa)	
		RMS	STD		RMS	STD
1	CLOSC1.3	0.508	0.082	CLOSC2.2	0.629	0.065
2	CLOSF1.3	0.482	0.095	CLOSF2.2	0.536	0.043
3	CLOSS1.3	0.465	0.095	CLOSS2.2	0.467	0.094
4	CMOSC1.3	0.629	0.093	CMOSC2.2	0.701	0.118
5	CMOSF1.3	0.585	0.094	CMOSF2.2	0.642	0.023
6	CMOSS1.3	0.584	0.139	CMOSS2.2	0.631	0.109
7	CHOSC1.3	0.755	0.099	CHOSC2.2	0.814	0.060
8	CHOSF1.3	0.708	0.115	CHOSF2.2	0.720	0.090
9	CHOSS1.3	0.605	0.034	CHOSS2.2	0.714	0.078
10	PLOSC1.3	0.685	0.050	PLOSC2.2	0.824	0.173
11	PMOSC1.3	0.840	0.030	PMOSC2.2	0.910	0.041
12	PHOSC1.3	1.013	0.053	PHOSC2.2	0.857	0.095

(Note: Data presented is from Table 4-1 and/or Table 4-2)

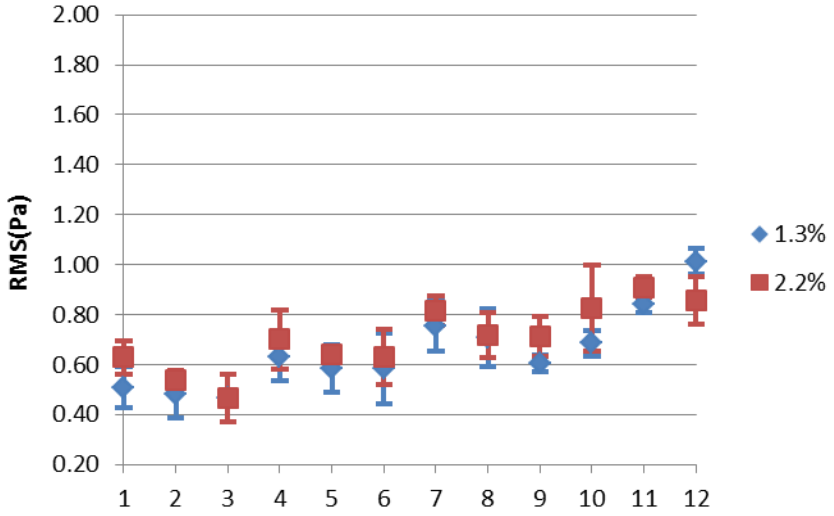

Figure 4-12. Bundle slackness: 1.3% vs. 2.2% (Error bar corresponds to the STD).

No consistent and statistically significant difference was observed between the RMS for 1.3 % and 2.2 % bundle slackness. However, in general, the RMS was higher for the module with looser fibers (2.2%), compared to those with tighter fibers (1.3%). This is consistent with results from previous studies that indicate that looser fiber will have higher shear stress than tighter fiber (Fulton *et al.*, 2011).

4.2.6 Summary of observations

1) A fine bubble diffuser is able to create higher shear stress than a coarse bubble diffuser, when baffle was in use, while the pulse bubble diffuser is able to create a higher shear stress than the coarse bubble

when the baffle was not in use. The difference between slow pulse and fast pulse diffuser was not significant.

2) The cylindrical baffle in the system tank can significantly increase the shear stress on the membrane surface. Cross-flow liquid, in general, was able to generate higher shear stress than the stagnant liquid.

3) Gas flow rate had a significant effect on the shear stress, the higher the flow rate, the higher the shear stress. Continuous flow can generate higher shear stress than the intermittent flow, due to the fact that only half of the volume of gas is added to the system for intermittent compared to continuous gas sparging.

4) Looser fiber (2.2%) will have a slightly higher shear stress than the tighter fiber (1.3%). However, the results were not statistically significant.

4.3 Filtration Tests Results

A total of 10 different experimental conditions were considered. The results of each filtration test (including replicate) are presented in Appendix 13. The time average (i.e. from replicate experiments) results for each condition are presented in Figures 4-13 and 4-14.

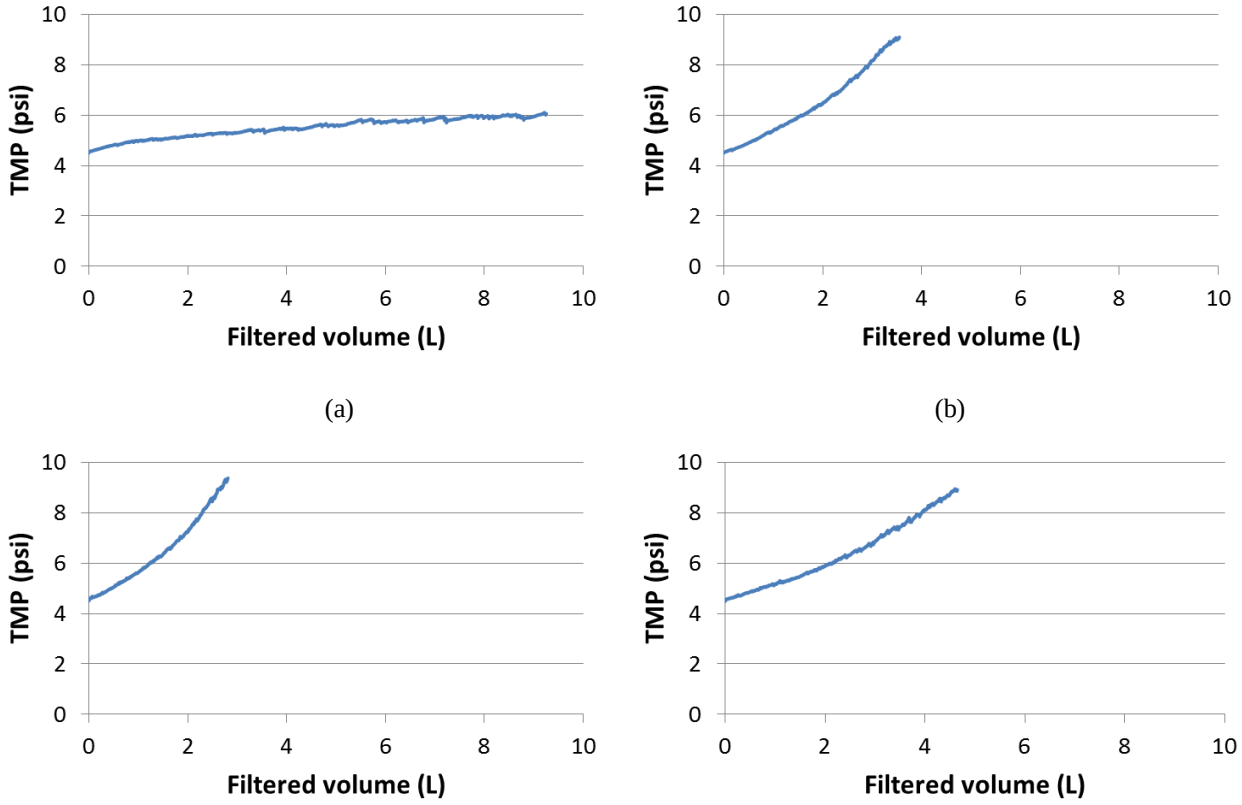

(a) (b)

(c) (d)

Figure 4-13. Averaged filtration results in D14 tank: (a) Slow pulse diffuser, stagnant bulk liquid and 3500 mL/min continuous gas flow; (b) Coarse bubble diffuser, stagnant bulk liquid and 3500 mL/min continuous gas flow; (c) Coarse bubble diffuser, stagnant bulk liquid and 3500 mL/min 3 sec on 3 sec off gas flow; and (d) Coarse bubble diffuser, stagnant bulk liquid and 7000 mL/min 2 sec on 2 sec off gas flow.

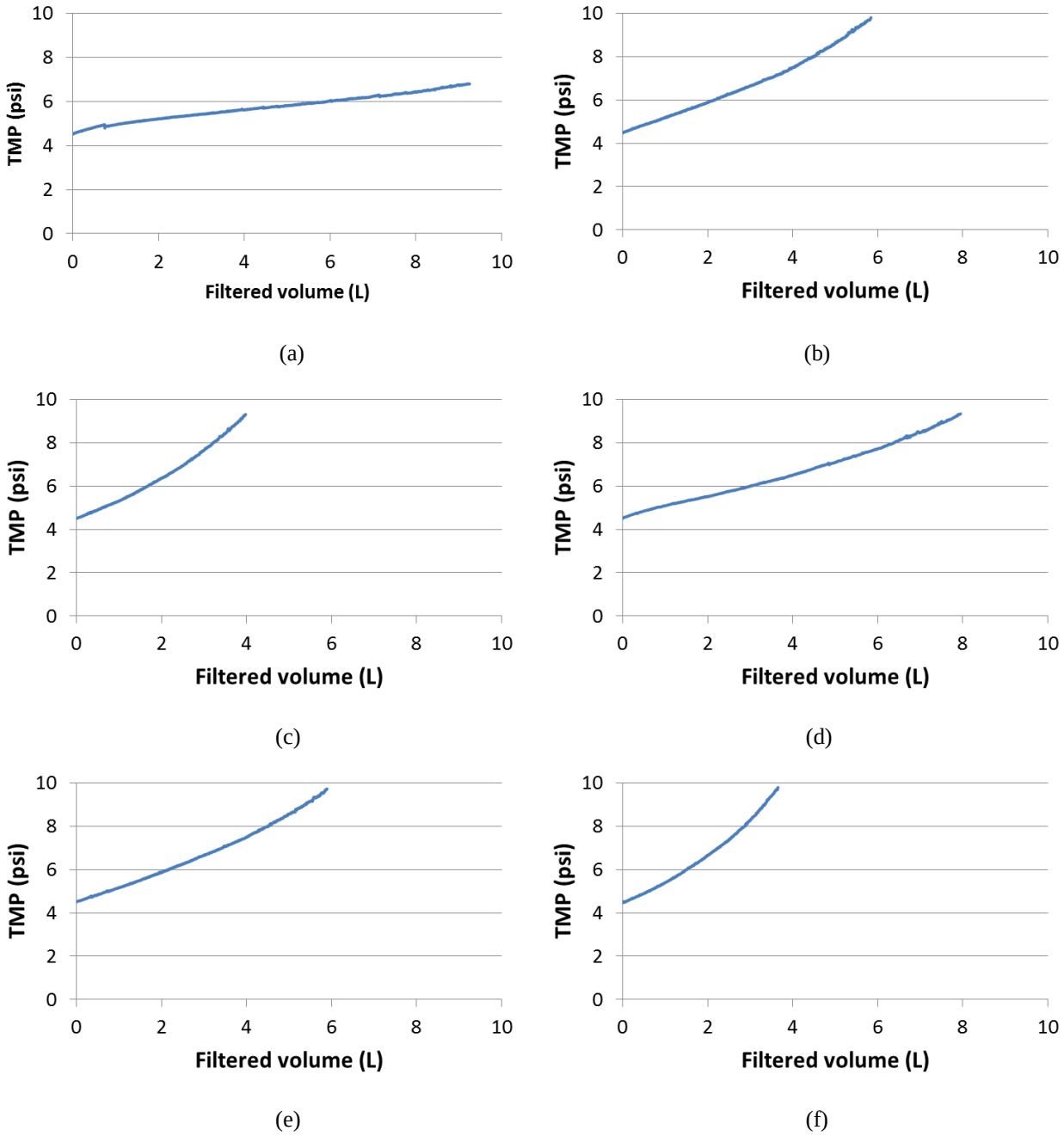

Figure 4-14. Averaged filtration results in D20 tank: (a) Slow pulse diffuser, cross-flow bulk liquid and 3500 mL/min continuous gas flow; (b) Slow pulse diffuser, cross-flow bulk liquid and 1750 mL/min continuous gas flow; (c) Slow pulse diffuser, cross-flow bulk liquid and 875 mL/min continuous gas flow; (d) Fast pulse diffuser, cross-flow bulk liquid and 3500 mL/min continuous gas flow; (e) Fast pulse diffuser, cross-flow bulk liquid and 1750 mL/min continuous gas flow; and (f) Fast pulse diffuser, cross-flow bulk liquid and 875 mL/min continuous gas flow.

The filtration laws (see section 2.3.2) were fitted to the filtration tests data. The complete blocking, the intermediate blocking and the cake fouling laws could all model the filtration data relatively well (see Appendix 13). However, for some cases, the cake fouling law could model the filtration data more

comprehensively than the other blocking models (see Appendix 13). For this reason, in the discussion that follows, the fouling rate for the cake fouling law is used to compare the results from the different filtration tests (Table 4-11).

Table 4-11. Fouling rates of the filtration tests under different conditions.

A) In D14 Tank

Diffuser type	Gas flow rate	Tank setup	Bulk flow pattern	Gas flow pattern	Slackness (%)	Fouling rate (psi/L)	
						Mean[1]	STD[2]
Slow Pulse Diffuser	3500 mL/min	Without baffle	Stagnant	Continuous	1.8	0.1966	0.0575
Coarse Diffuser	3500 mL/min	Without baffle	Stagnant	Continuous	1.8	1.1946	0.1022
			Stagnant	3 sec on/off	1.8	1.5298	0.1108
	7000 mL/min	Without baffle	Stagnant	2 sec on/off	1.8	0.8783	0.1539

B) In D20 Tank

Diffuser type	Gas flow rate	Tank setup	Bulk flow pattern	Gas flow pattern	Slackness (%)	Fouling rate (psi/L)	
						Mean[1]	STD[2]
Slow Pulse Diffuser	3500 mL/min	With baffle	Cross-flow	Continuous	1.8	0.3088	0.0139
	1750 mL/min	With baffle	Cross-flow	Continuous	1.8	0.7940	0.0213
	875 mL/min	With baffle	Cross-flow	Continuous	1.8	1.0826	0.0853
Fast Pulse Diffuser	3500 mL/min	With baffle	Cross-flow	Continuous	1.8	0.5388	0.0054
	1750 mL/min	With baffle	Cross-flow	Continuous	1.8	0.7974	0.0457
	875 mL/min	With baffle	Cross-flow	Continuous	1.8	1.2290	0.0098

[1]Mean value presented is the averaged cake fouling constant from replicate tests (Appendix 13).

[2]STD is calculated from the replicate mean values mentioned in [1].

4.4 Filtration Tests Discussions

4.4.1 RMS and fouling rate

For six of the experimental conditions investigated, both shear stress measurements and filtration data are available. The RMS of surface shear stress and the fouling rate for these experimental conditions are summarized in Table 4-12 and Figure 4-15.

Table 4-12. The filtration results and the corresponding[1] shear stress measurements results.

A) In D14 tank

Diffuser type	Gas flow rate	Tank setup	Bulk flow pattern	Gas flow pattern	Slackness[2] (%)	Fouling rate (psi/L)		Shear stress (Pa)	
						Mean	STD	RMS	STD
Slow Pulse Diffuser	3500 mL/min	Without baffle	Stagnant	Continuous	1.8	0.1966	0.0575	0.824	0.173
Coarse Diffuser	3500 mL/min	Without baffle	Stagnant	Continuous	1.8	1.1946	0.1022	0.629	0.065
			Stagnant	3 sec on/off	1.8	1.5298	0.1108	0.536	0.043
	7000 mL/min[3]	Without baffle	Stagnant	2 sec on/off[4]	1.8	0.8783	0.1539	0.720	0.090

B) In D20 tank

Diffuser type	Gas flow rate	Tank setup	Bulk flow pattern	Gas flow pattern	Slackness[2] (%)	Fouling rate (psi/L)		Shear stress (Pa)	
						Mean	STD	RMS	STD
Slow Pulse Diffuser	3500 mL/min	With baffle	Cross-flow	Continuous	1.8	0.3088	0.0139	0.916	0.072
Fast Pulse Diffuser	3500 mL/min	With baffle	Cross-flow	Continuous	1.8	0.5388	0.0054	0.883	0.112

(Note: Data presented is from Table 4-11, Table 4-1, and/or Table 4-2)

[1]As the conditions in the filtration tests and shear stress measurements were not exactly the same, the shear stress results were selected by the closest conditions as explained in follows.

[2]1.8% slackness was only used in filtration tests. The data of 2.2% slackness in shear stress measurements were selected for comparison.

[3]7000 mL/min gas flow rate was only used in filtration tests. The data of 8000 mL/min gas flow rate in shear stress measurements was selected for comparison.

[4]2 sec on/off gas flow pattern was only used in filtration tests. The data of 3 sec on/off gas flow pattern in shear stress measurement was selected for comparison.

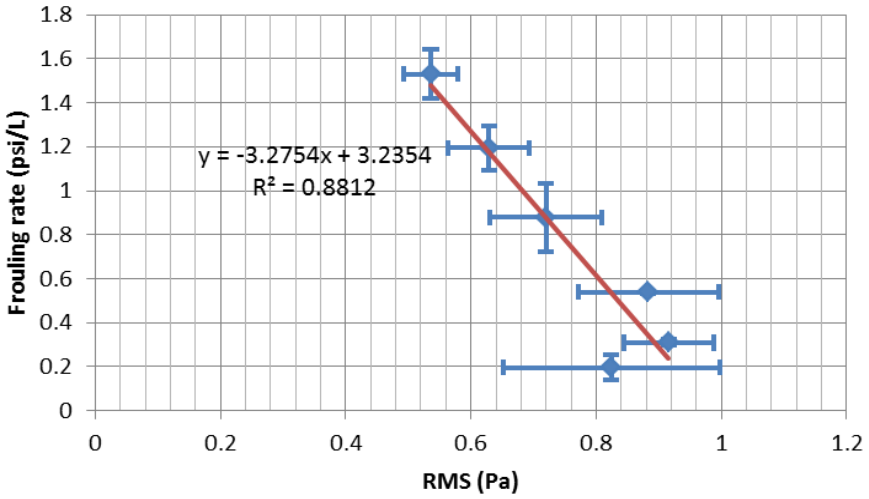

Figure 4-15. RMS vs. fouling rate (Error bar corresponds to the STD).

From Figure 4-15, it can be observed, that when the RMS values increases, the fouling rate decreases. The results are consistent with those from previous studies (Yeo *et al.*, 2006; Fulton *et al.*, 2011) and indicate that RMS can be used to provide an estimate of the extent of fouling control that can be achieved when inducing a given amount of shear stress using gas sparging.

4.4.2 Effect of diffuser type

4.4.2.1 Coarse bubble diffuser vs. Pulse bubble diffuser

The RMS and fouling rate were obtained for a total of 4 experimental conditions, for which coarse bubble diffuser and pulse bubble diffuser were used (Table 4-13). The average filtration results of replicate experiments for these experimental conditions are summarized in Figure 4-16.

Table 4-13. The RMS and filtration results of foarse bubble diffuser vs. pulse bubble diffuser.

Diffuser type	Gas flow rate	Tank setup	Bulk flow pattern	Gas flow pattern	Slackness (%)	Fouling rate (psi/L)		Shear stress (Pa)	
						Mean	STD	RMS	STD
Coarse Diffuser	3500 mL/min	Without baffle	Stagnant	Continuous	1.8	1.1946	0.1022	0.629	0.065
Slow Pulse Diffuser	3500 mL/min	Without baffle	Stagnant	Continuous	1.8	0.1966	0.0575	0.824	0.173
	875 mL/min	With baffle	Cross-flow	Continuous	1.8	1.0826	0.0853	-	-
Fast Pulse Diffuser	875 mL/min	With baffle	Cross-flow	Continuous	1.8	1.2290	0.0098	-	-

(Note: Data presented is from Table 4-11, Table 4-1, and/or Table 4-2)

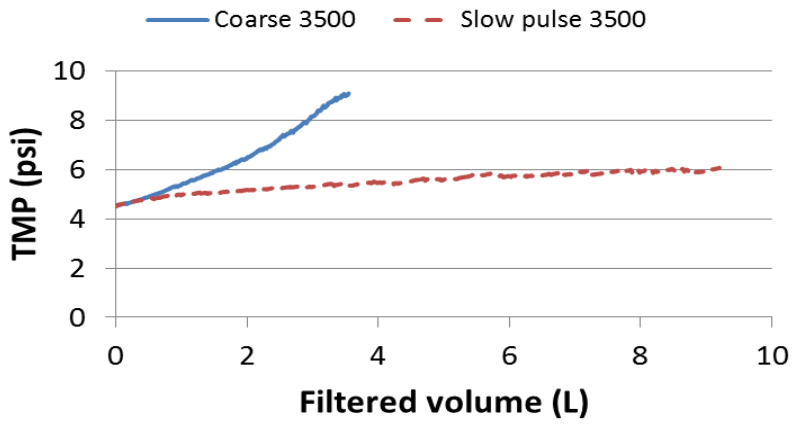

(a)

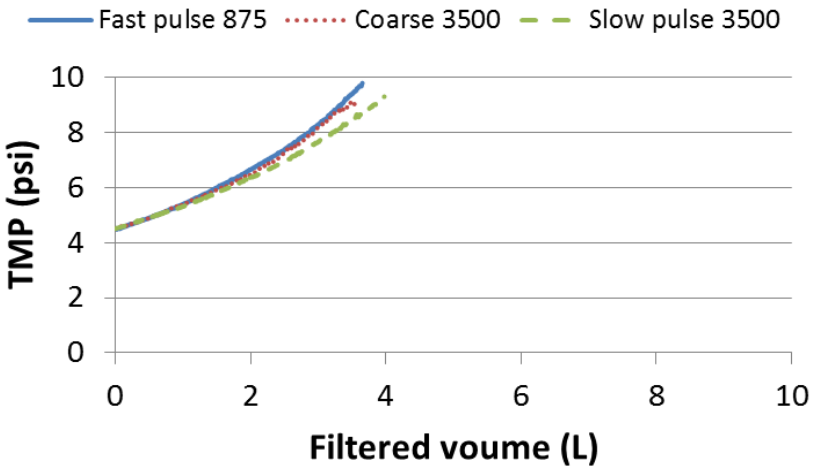

(b)

Figure 4-16. Filtration results of coarse bubble diffuser vs. pulse bubble diffuser: (a) Conditions with the same gas flow rate. (b) Conditions with the similar fouling rate.

For a given gas flow rate, pulse sparging resulted in a 10 fold reduction in the rate of fouling, compared to the rate of fouling achieved with coarse bubble sparging (Table 4-13 and Figure 4-16a). To achieve a given rate of fouling control, Approximately 25% of the gas flow rate required for continuous sparging was needed for pulse sparging (Table 4-13 and Figure 4-16b). These results clearly indicate that a significantly lower gas flow rate is required to achieve a given fouling rate with pulse sparging, compared to continuous coarse bubble sparging.

4.4.2.2 Slow pulse diffuser vs. Fast pulse diffuser

The RMS and fouling rate were obtained for a total of 6 experimental conditions, for which slow pulse diffuser and fast pulse diffuser were used (Table 4-14). The average filtration results of replicate experiments for these experimental conditions are summarized in Figure 4-17.

Table 4-14. The RMS and filtration results of slow pulse diffuser vs. fast pulse diffuser.

Diffuser type	Gas flow rate	Tank setup	Bulk flow pattern	Gas flow pattern	Slackness (%)	Fouling rate (psi/L)		Shear stress (Pa)	
						Mean	STD	RMS	STD
Slow Pulse Diffuser	3500 mL/min	With baffle	Cross-flow	Continuous	1.8	0.3088	0.0139	0.916	0.072
	1750 mL/min	With baffle	Cross-flow	Continuous	1.8	0.7940	0.0213	-	-
	875 mL/min	With baffle	Cross-flow	Continuous	1.8	1.0826	0.0853	-	-
Fast Pulse Diffuser	3500 mL/min	With baffle	Cross-flow	Continuous	1.8	0.5388	0.0054	0.883	0.112
	1750 mL/min	With baffle	Cross-flow	Continuous	1.8	0.7974	0.0457	-	-
	875 mL/min	With baffle	Cross-flow	Continuous	1.8	1.2290	0.0098	-	-

(Note: Data presented is from Table 4-11, Table 4-1, and/or Table 4-2)

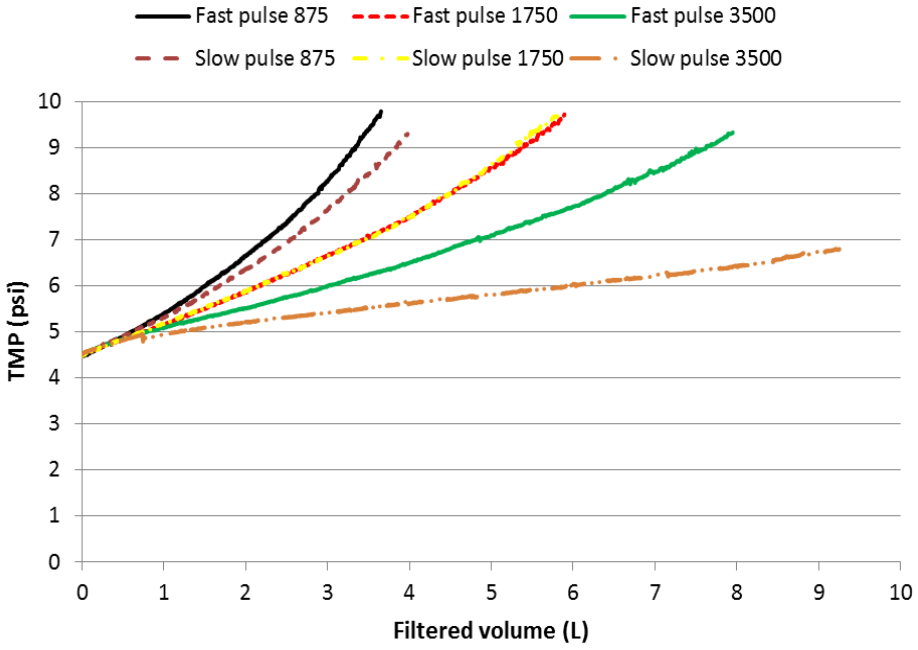

Figure 4-17. Filtration results of slow pulse diffuser vs. fast pulse diffuser.

For a relatively high gas flow rate (i.e. 3500 mL/min), the fouling rate for the fast pulse diffuser was about 44% higher than that for the slow pulse diffuser. This was expected because the size of the bubble generated by the slow pulse bubble diffuser was approximately twice the size of that generated by the fast bubble diffuser. For lower gas flow rates (i.e. 1750 and 875 mL/min), no significant difference was observed between the slow and fast pulse diffusers. These results indicate that, in addition to the

magnitude of the shear stress, the frequency of shear events also likely affect fouling control. Further research is required to confirm this hypothesis.

4.4.3 Effect of bulk liquid flow pattern

The RMS and fouling rate were obtained for a total of 2 experimental conditions, for which stagnant and cross-flow bulk liquid flow pattern were used (Table 4-15). The average filtration results of replicate experiments for these experimental conditions are summarized in Figure 4-18.

Table 4-15. The RMS and filtration results of stagnant vs. cross-flow.

Diffuser type	Gas flow rate	Tank setup	Bulk flow pattern	Gas flow pattern	Slackness (%)	Fouling rate (psi/L)		Shear stress (Pa)	
						Mean	STD	RMS	STD
Slow Pulse Diffuser	3500 mL/min	Without baffle	Stagnant	Continuous	1.8	0.1966	0.0575	0.824	0.173
	3500 mL/min	With baffle	Cross-flow	Continuous	1.8	0.3088	0.0139	0.916	0.072

(Note: Data presented is from Table 4-11, Table 4-1, and/or Table 4-2)

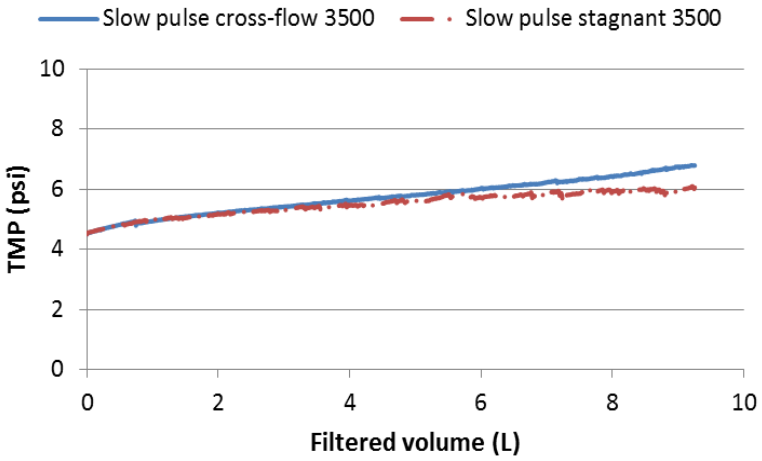

Figure 4-18. Filtration results of stagnant vs. cross-flow.

For a given sparging flow rate, the fouling rate for stagnant bulk liquid was slightly lower than that for a bulk liquid with cross-flow. Future experiments are required to verify the result.

4.4.4 Effect of gas flow pattern

The RMS and fouling rate were obtained for a total of 4 experimental conditions for which continuous and intermittent gas flow pattern were used (Table 4-16). The average filtration results of replicate experiments for these experimental conditions are summarized in Figure 4-18.

Table 4-16. Continuous gas flow pattern vs. intermittent gas flow pattern.

Diffuser type	Gas flow rate	Tank setup	Bulk flow pattern	Gas flow pattern	Slackness (%)	Fouling rate (psi/L)		Shear stress (Pa)	
						Mean	STD	RMS	STD
Coarse Diffuser	3500 mL/min	Without baffle	Stagnant	Continuous	1.8	1.1946	0.1022	0.629	0.065
			Stagnant	3 sec on/off	1.8	1.5298	0.1108	0.536	0.043
	7000 mL/min	Without baffle	Stagnant	2 sec on/off	1.8	0.8783	0.1539	0.720	0.090
Slow Pulse Diffuser	3500 mL/min	Without baffle	Stagnant	Continuous	1.8	0.1966	0.0575	0.824	0.173

(Note: Data presented is from Table 4-11, Table 4-1, and/or Table 4-2)

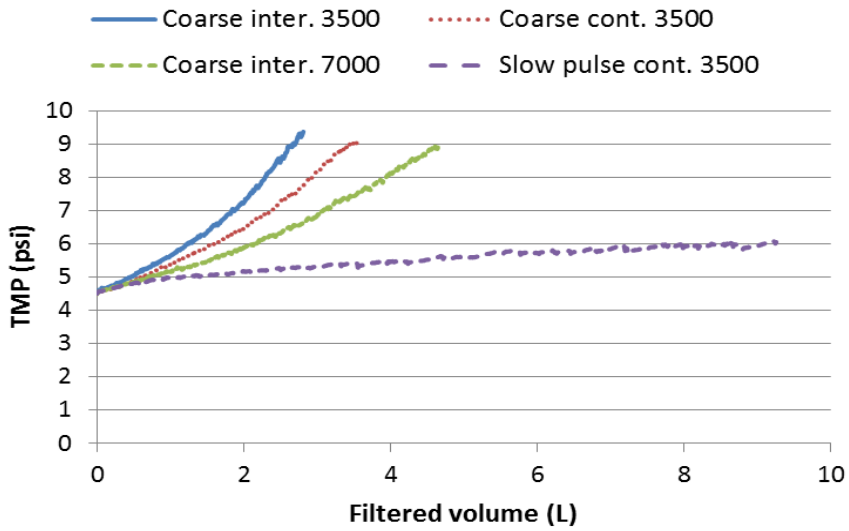

Figure 4-19. Filtration results of continuous gas flow pattern vs. intermittent gas flow pattern.

For a given gas flow rate, continuous coarse bubble sparging was significantly better at fouling control than intermittent coarse bubble sparging. However, since the gas flow rate is added during the on cycle for intermittent sparging, the amount (i.e. volume) of gas delivered to the system is approximatly half of the amount delivered when using continuous sparging. When the same amount of gas is delivered, better fouling control was achieved with intermttent coarse bubble sparging (7000 mL/min with flow turn off 50% of time) than conitnuous coarse bubble sparging (3500 mL/min continuously). The pulse diffuser,

which can be considered as an extreme intermittent sparging device because air is actually only added periodically when the large bubbles are released, resulted in better fouling control than either continuous coarse bubble or intermittent coarse bubble sparging. These results clearly indicate that for a given volume of sparged gas applied, better fouling control can be achieved with intermittent sparging than continous sparging.

4.4.5 Summary of observations

1) The RMS shear stress had a strong correlation with the fouling rate, which can be used to provide an estimate of the extent of fouling control.
2) Pulse sparging had a very significant reduction in the rate of fouling, compared to the rate of fouling achieved with coarse bubble sparging. A significantly lower gas flow rate is required to achieve a given fouling rate with pulse sparging, compared to continuous coarse bubble sparging.
3) Slow pulse diffuser had a better fouling control than the fast pulse diffuser, when the gas flow rate was relatively high; however, when the flow rate reduced, the difference between slow pulse and fast pulse diffuser was reduced. The frequency of shear events also likely affected fouling control.
4) For a given sparging flow rate, the fouling rate for stagnant bulk liquid was slightly lower than that for a bulk liquid with cross-flow.
5) For a given volume of sparged gas applied, better fouling control can be achieved with intermittent sparging than continuous sparging.

5. CONCLUSIONS

5.1 Overall Conclusions

In this thesis, the relationship between the shear stress and the fouling control was investigated in a comprehensive manner. Shear stresses induced by different gas sparging conditions were measured and the effect of these sparging conditions on membrane fouling was quantified. The following are the main conclusions from this study.

Shear stress measurements

For the six sparging conditions used in the shear stress measurements, flow rate and tank setup can significantly increase the shear stress on the membrane surface. The ideas of these two conditions were similar, which are increasing the volume of gas close to the membrane fibers (by either increasing sparging rate or by adding baffle to concentrate the gas) to promote shear. However, these two conditions required high energy input and high capital cost, which is not preferred in industrial applications.

For the rest of the four conditions, diffuser type, bulk liquid flow pattern, gas flow pattern and bundle slackness are more preferable to optimize the gas sparging, since they don't required much capital and operational cost. The results indicated that:

1) The pulse bubble diffuser presented to be a better sparger than coarse bubble diffuser when a baffle was not in use.
2) Cross-flow liquid in general was able to generate higher shear stress than the stagnant liquid.
3) Continuous flow can generate higher shear stress than the intermittent flow due to the fact that only half of the volume of gas is added to the system for intermittent, compared to continuous gas sparging.
4) Looser fiber (2.2%) will have a slightly higher shear stress than the tighter fiber (1.3%). However, the results were not statistically significant.

Filtration tests

The filtration tests were designed to firstly examine the relationship between the shear stress and fouling rate and also to investigate the effect of different sparging conditions. Due to this reason, the tank setup and bundle slackness were fixed as constants in the filtration tests. The results indicate that:

1) The RMS shear stress had a strong correlation with the fouling rate, which can be used to provide an estimate of the extent of fouling control.
2) Pulse sparging was overall better than the conventional coarse sparging. A 10 fold reduction was observed when applying the same gas flow to pulse diffuser than the coarse diffuser. Only one quarter of the gas was required to achieve the same fouling control when using a pulse diffuser.
3) For a given sparging flow rate, the fouling rate for stagnant bulk liquid was slightly lower than that for a bulk liquid with cross-flow.
4) For a given volume of sparged gas applied, better fouling control can be achieved with intermittent sparging than continuous sparging.

5.2 Contribution and Engineering Significance

This research successfully created the variable shear conditions identified by Chan et al. (2011) using the gas sparging. The different shear profiled was recorded by the electrochemical shear method. In addition, filtration tests examine the different sparging conditions to the fouling rate to further confirm which sparging approach can actually improve the fouling control in a submerged hollow fiber system.

Pulse bubble diffuser proved to be a very effective way to introduce the gas into the sparging system. A 10 fold reduction was observed when applying the same gas flow to pulse diffuser than the coarse diffuser. Only one quarter of the gas was required to achieve the same fouling control when using a pulse diffuser. By using the pulse diffuser, the energy input of gas sparging can be significantly reduced. In addition, the backwash cycle can be prolonged during the filtration, which can also significantly reduce the operational costs.

REFERENCES

Belfort, G., Davis, R.H. and Zydney, A.L. (1994) The behavior of suspensions and macromolecular solutions in cross-flow microfiltration. *Journal of Membrane Science* ***96(1-2)****, 1-58*

Bellara, S.R., Cui, Z.F. and Pepper, D.S. (1996) Gas sparging to enhance permeate flux in ultrafiltration using hollow fibre membranes. *Journal of Membrane Science* ***121(2)****, 175-184*

Berger, F.P. and Ziai, A. (1983) Optimisation of experimental conditions for electrochemical mass transfer measurements. *Chemical Engineering Research and Design* ***61a****, 377 – 382*

Bérubé, P.R., Afonso, G., Taghipour, F. and Chan, C.C.V. (2006) Quantifying the shear at the surface of submerged hollow fiber membranes. *Journal of Membrane Science* ***279(1-2)****, 495-505*

Bérubé, P.R. and Lei, E. (2006) The effect of hydrodynamic conditions and system configurations on the permeate flux in a submerged hollow fiber membrane system. *Journal of Membrane Science* ***271(1-2)****, 29-37*

Busch, J., Cruse, A. and Marquardt. W. (2007) Modeling submerged hollow-fiber membrane filtration for wastewater treatment. *Journal of Membrane Science* ***288(1-2)****, 94-111*

Cabassud, C., Laborie, S. and Laine, J.M. (1997) How slug flow can improve ultrafiltration flux in organic hollow fibres. *Journal of Membrane Science* ***128(1)****, 93-101*

Chan, C.C.V., Bérubé, P.R. and Hall, E.R. (2011) Relationship between types of surface shear stress profiles and membrane fouling. *Water Research* ***45****, 6403-6416*

Chan, C.C.V., Berube, P.R. and Hall, E.R. (2007) Shear profiles inside gas sparged submerged hollow fiber membrane modules. *Journal of Membrane Science* ***297 (1-2)****, 104-120*

Chang, S. and Fane, A.G. (2000) Characteristics of microfiltration of suspensions with inter-fiber twophase flow. *Journal of Chemical Technology and Biotechnology* ***75(7)****, 533-540*

Chang, I.S., Le Clech, P., Jefferson, B. and Judd, S. (2002) Membrane fouling in membrane bioreactors for wastewater treatment. *Journal of Environmental Engineering-Asce* ***128(11)****, 1018-1029*

Cheng, T.W., Yeh, H.M. and Gau, C.T. (1998) Enhancement of permeate flux by gas slugs for crossflow ultrafiltration in tubular membrane module. *Separation Science and Technology* ***33(15)****, 2295-2309*

Cui, Z.F., Chang, S. and Fane, A.G. (2003) The use of gas bubbling to enhance membrane processes. *Journal of Membrane Science* ***221(1-2)****, 1-35*

Cui, Z.F. and Wright, K.I.T. (1994) Gas-Liquid 2-Phase Cross-Flow Ultrafiltration of Bsa and Dextran Solutions. *Journal of Membrane Science* ***90(1-2)****, 183-189*

Field, R.W., Wu, D., Howell, J.A. and Gupta, B.B. (1995) Critical flux concept for microfiltration fouling. *Journal of Membrane Science* ***100(3)****, 259-272*

Fulton, B.G., Redwood, J., Tourais, M. and J. Berube, P.R. (2011) Distribution of surface shear forces and bubble characteristics in full-scale gas sparged submerged hollow fiber membrane modules. *Desalination* ***281****, 128-141*

Gaucher, C., L., P., Jaouen, P., Comiti J. and Pruvost, J. (2002) Hydrodynamics study in a plane ultrafiltration module using an electrochemical method and particle image velocimetry visualization. *Experiments in Fluids* ***32(3)****, 283-293*

Govan, A.H., Hewitt, G.F., Owen, D.G, Burnett, G. (1989) Wall shear stress measurements in vertical air-water annular two-phase flow. *Journal of Multiphase Flow* ***15(3)****, 307-325*

Gonsalves, V.E. (1950) A criťical investigation on the viscose filtration process. *Recueil des Travaux Chimiques des Pays-Bas* **69(7)**, 873–903

Green, G., and Belfort, G. (1980) Fouling of ultrafiltration membranes: lateral migration and the particle trajectory model. *Desalination* ***35****, 129-147*

Hermans, P.H. and Bredée, H.L. (1935) Zur Kenntnis der Filtrationsgesetze. *Recueil des Travaux Chimiques des Pays-Bas* ***54 (9)*** *680–700*

Hermia, J. (1982) Constant pressure blocking filtration laws - application to ower-law non-newtonian fluids. *Transactions in Chemical Engineering* ***60****, 183-187*

Judd., S. (2006) *The MBR Book: Principles and Applications of Membrane Bioreactors for Water and Wastewater Treatment.* Elsevier Science

Kissinger, P. T. and Heineman, W. R. (1996) *Laboratory techniques in electroanalytical chemistry (2nd ed.).* Mercel Dekker Inc. New York

Koros, W.J., Ma, Y.H., and Shimidzu, T. (1996) Terminology for membranes and membrane processes (IUPAC Recommendation 1996). *Journal of Membrane Science* ***120(2)****, 149-159*

Legrand, J., Dumont, E., Comiti, J. and Fayolle, F. (2000). Diffusion coefficients of ferricyanide ions in polymeric solutions — comparison of different experimental methods. *Electrochimica Acta* ***45(11)****, 1791-1803*

Li, Q.Y., Ghosh, R., Bellara, S.R., Cui, Z.F. and Pepper, D.S. (1998) Enhancement of ultrafiltration by gas sparging with flat sheet membrane modules. *Separation and Purification Technology* ***14(1-3)****, 79-83*

Mercier-Bonin, M., Gesan-Guiziou, G. and Fonade, C. (2003) Application of gas/liquid two-phase flows during crossflow microfiltration of skimmed milk under constant transmembrane pressure conditions. *Journal of Membrane Science* ***218(1-2)****, 93-105*

Metcalf and Eddy, Inc. et al. (1991) *Wastewater engineering, treatment, disposal, and reuse*. McGraw-Hill, New York, NY

Metcalf and Eddy, Inc. et al. (2003) *Wastewater Engineering Treatment and Reuse* (*4th Edition).* McGraw-Hill, New York, NY

Nagaoka, H., Kurosaka, M., Shibata, N. and Kobayashi, M. (2006) Effect of bubble flow velocity on drag-force and shear stress working on submerged hollow fibre membrane. *Water Science and Technology* ***54(10)****, 185-192*

Nakoryakov, V. E., Kashinsky, O. N., Burdukov, A. P. and Odnoral, V. P. (1981) Local characteristics of upward gas-liquid flows. *International Journal of Multiphase Flow* ***7(1)****, 63-81.*

Nakoryakov, V.E., Kashinsky, O.N. and Kozmenko, B.K. (1986) Experimental study of gas-liquid slug flow in a small diameter vertical pipe. *Journal of Multiphase Flow* ***12(3)****, 337-355*

Owen, G., Bandi, M., Howell, J.A. and Churchouse, S.J. (1995) Economic assessment of membrane processes for water and waste water treatment. *Journal of Membrane Science* ***102****, 77-91*

Reiss, P.L. and Hanratty, T.J. (1962) Measurement of instantaneous rates of mass transfer to a small sink on a wall. *American Institute of Chemical Engineers Journal* ***8(2)****, 245-247*

Reiss, L. P. and Hanratty, T. J. (1963) An experimental study of the unsteady nature of the viscous sublayer. *American Institute of Chemical Engineers Journal* ***9(2)****, 154-160*

Rode, S., Midoux, N., Latifi, M.A. and Storck, A. (1994) Hydrodynamic and liquid-solid mass transfer mechanisms in packed beds operating in cocurrent gas-liquid downflow: an experimental study using electrochemical shear rate sensors. *Chemical Engineering Science* ***49(9)****, 1383-1401*

Rosant, J.M. (1994) Liquid-wall shear stress in stratified liquid/gas flow. *Journal of Applied Electrochemistry* ***24(7)****, 612-618*

Selman, J.R. and Tobias, C.W. (1978) Mass-transfer measurements by the limiting-current technique. *Advances in Chemical Engineering*, ***10****, 211-318*

Seyssiecq, I., Ferrasse, J.-H. and Roche, N. (2003) State of the art: rheological characterisation of wastewater treatment sludge, *Biochem. Eng. J* ***16****, 41–56*

Sobolik, V., Tihon, J., Wein, O. and Wichterle K. (1998) Calibration of electrodiffusion friction probes using a voltage-step transient. *Journal of Applied Electrochemistry* ***28(3)****, 329-335*

Taama, W. M., Plimley, R. E. and Scott, K. (1996) Influence of supporting electrolyte on ferricyanide reduction at a rotating disc electrode. *Electrochimica Acta* ***41(4)****, 549-551*

Ueda, T., Hata, K., Kikuoka, Y. and Seino, O. (1997) Effects of aeration on suction pressure in a submerged membrane bioreactor. *Water Research* ***31(3)****, 489-494*

Yeo, A.P.S., Law, A.W.K. and Fane, A.G. (2006) Factors affecting the performance of a submerged hollow fiber bundle. *Journal of Membrane Science* ***280(1-2)****, 969-982*

Zabaras, G., Dukler, A.E. and Moalemmaron, D. (1986) Vertical upward cocurrent gas-liquid annular flow. *Aiche Journal* ***32(5)****, 829-843*

Zydney, A.L. and Colton, C.K. (1986) A concentration polarization model for the filtrate flux in cross-flow microfiltration of particulate suspensions. *Chemical Engineering Communications* ***47(1-3)****, 1-21*

APPENDIX 1. PRINCIPLE OF ELECTROCHEMICAL SHEAR PROBE

As membrane surface shear stress has been recognized as playing a significant role in fouling reduction within membrane systems, many methods have been used to examine and quantify this parameter. Electrochemical shear probes are not only uniquely well suited for measuring shear stress within two-phase flow systems, but have the additional benefits of rapid response and relatively simple construction. The measurement of the shear stress using electrochemical methods was first performed by Reiss and Hanrraty (1962), and has been used extensively by other researchers to study mass transfer and local hydrodynamic properties in fluidized reactors, two phase pipe flows etc. (Zabaras, 1986; Govan, 1989; Nakoryakov, 1986; Rode, 1994). The principle of the electrochemical method for the shear stress measurement is that the current between cathode and anode in an electrochemical cell depends on the change of flow rate. Usually, in a cell the shear probe is operated as the cathode which is also the controlling electrode to determine the current strength. In the following sections, the principle of electrochemical shear method and the theory using for shear probe measurement and calibration would be discussed.

A1.1 Limiting Current Condition

Figure A1-1 shows the relationship between measured current density and the applied potential in an electrochemical cell. In Zone I, the redox reaction rate at the shear probe is less than the rate of arrival of the reacting species to the shear probe. Increasing applied potential results in an increase in the reaction rate at the shear probe, and therefore an increase in the current density. In Zone II, the reaction rate at the shear probe is greater than the rate of arrival of the reacting species to the shear probe. The reaction rate at the shear probe is so high that the concentration of the reacting species at the shear probe surface is zero. Under this condition, the current is not a function of applied potential. Further increase in the applied potential does not have any effect on the reaction rate. The measured current is dependent only on the diffusion and migration of the reacting species from the bulk solution to the shear probe. This condition is called limiting current condition, or the limiting diffusion condition. In Zone III, the applied

potential exceeds the discharge potential of the solvent, causing the secondary reaction (such as hydrogen evolution) at the shear probe, therefore the current increases.

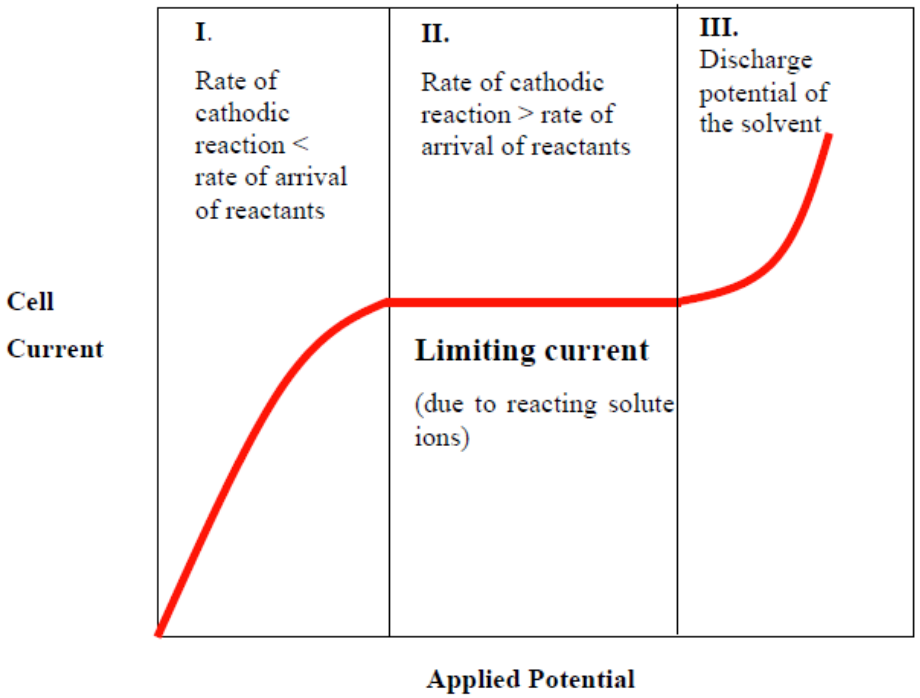

Figure A1-1. Typical current-potential relationship in an electrochemical cell when a potential is applied between two electrodes.

The limiting current condition defined in Zone II is the region where the electrochemical shear method is applicable. Under the limiting current condition, the magnitude of the current passing through the shear probe is a consequence of just three variables: (1) the diffusion rate of ions to/from the shear probe surface, (2) the shear probe surface area, and (3) the concentration of the active ionic species within the solution (Kissinger and Heineman, 1996). To prevent the reaction at the probe surface from being limited by the reaction rate at its counter-electrode, the counter-electrode (anode) must have a much larger active surface area than the probe (Nakoryakov *et al.*, 1981; Reiss and Hanratty, 1963). In addition, the range of Zone II depends on the Reynolds number in the system. The larger the Reynolds number, the smaller the range of plateau. As a result, limiting current test of the system is required before the electrochemical measurement to make sure that the applied potential is the right range to create limiting current condition.

A1.2 The Leveque Equation and Steady-state Calibration

As the measured current is dependent on the probe surface area and it is difficult to fabricate a probe with an area of an exact value, to compare the measured value between two probes or two different experiments, the calibration of the shear probe is essential.

The limiting current (I) can be calculated using the theory of convective diffusion of a single species. If the Péclet number is so high that the effects of longitudinal and transverse diffusion can be neglected, the equation of convective diffusion under steady state can be solved. The resulting Leveque equation to calculate the limiting current I is presented in equation A1-1 (Sobolik *et al*., 1998).

$$I = K_{Lev}\gamma^{1/3} \qquad \text{(A1-1)}$$

where the K_{Lev} [A $s^{1/3}$] is the Leveque coefficient and γ [s^{-1}] is the shear rate or velocity gradient on the probe surface. Leveque coefficient can be estimated from the following equation if the shear probe is circular:

$$K_{Lev} = nFAckD^{2/3}d^{-1/3} \qquad \text{(A1-2)}$$

where n is a dimensionless number indicate the amount of electrons involved in reaction, F [96485C mol^{-1}] is the Faraday constant, A [m^2] is the area of the shear probe surface, c [mol m^{-3}] is the mol concentration of bulk solution, k [0.862 for circular probe] is a dimensionless represent the shape factor of the shear probe, D [m^2 s^{-1}] is the diffusion coefficient and d [m] is the diameter of the shear probe. If the electrochemical solution is a Newtonian fluid, applying the Newtonian law of viscosity, the shear rate can be calculated by equation A1-3 and A1-4.

$$\tau = \mu \frac{\delta v_x}{\delta y} = \mu\gamma \qquad \text{(A1-3)}$$

$$\gamma = \frac{\tau}{\mu} \qquad \text{(A1-4)}$$

where τ [Pa] is the shear stress and μ [Pa·s] is the dynamic viscosity. Combining equations A1-1 to A1-4 we can get the equation A1-5 (Sobolik *et al*., 1998).

$$I = K_{Lev}\mu^{1/3}\tau^{1/3} \qquad \text{(A1-5)}$$

Although the exact probe diameter and area are not known, the K_{Lev} can be estimated experimentally for a given probe by inducing a known shear stress and measuring the resulting current through the probe (for a given electrochemical solution and temperature). Knowing K_{Lev}, the shear stress can be estimated based on the current measurements through the probe.

A1.3 The Cottrell Equation and Voltage Step Calibration

As an alternative, an in-situ voltage step calibration approach can be used to convert the measured current I to a shear stress. The calibration starts from the zero-current state with the corresponding equilibrium voltage. At t = 0 a constant voltage V is applied which is high enough to guarantee the limiting diffusion regime under the ultimate steady-state condition. If the additional transport (ohmic and faradaic) resistances are negligible at any moment of the transient process, the applied voltage step causes a step change of the surface depolarizer concentration from bulk concentration zero (or a negligible fraction of bulk concentration).The transient current for a very short time after this step, can be fitted to Cottrell equation (Sobolik *et al*., 1998) to determine K_{Cot} (equation A1-6), from which the probe area can be derived using equation A1-7.

$$I = K_{Cot} t^{1/2} \qquad \text{(A1-6)}$$

$$K_{Cot} = nFAcD^{1/2}\pi^{-1/2} \qquad \text{(A1-7)}$$

where K_{Cot} is [A $s^{-1/2}$] the Cottrell coefficient and t [s] is the time after the voltage is applied. Other variables n, F, A, c and D is the same as in equation A1-2. However, the estimated area of the shear probe is highly depends on the current measured in the short time interval so that the noise may have significant effect. Sampling frequency will also affect the results.

Applying the theory and the equation that mentioned above, the electrochemical method can be used to measure the shear stress on the membrane surface, which would be the key parameter of the hydrodynamic conditions in the submerged hollow fiber system.

APPENDIX 2. SHEAR PROBE CALIBRATIONS

Before the shear probes were, they were calibrated in a side loop setup. The side loop set up was able to create a controlled hydrodynamic condition, which is required for the steady-state calibration process. This setup has been used by Fulton *et al*. (2011) for the probe calibration.

A2.1 Structure of Electrochemical Shear Probe

Electrochemical probes have been used extensively by other researchers to study mass transfer and hydrodynamic properties in fluidized reactors. The surface area of a shear probe is usually very small as measurements reflect the average of the shear stresses experienced across the entire probe surface, which for large probes may prevent an accurate reading of the real shear stresses experienced at any specific point (Reiss and Hanratty, 1963). Nickel and platinum have both commonly been used as electrode materials with the ferri-ferrocyanide couple for mass transfer measurements, but results of Taama *et al*. (1996) indicate that platinum is far superior for this purpose, as it requires less frequent cleaning to maintain its ability to provide accurate readings.

The electrochemical shear probes used in the present study were essentially the same as those used by Fulton *et al*. (2011), a 0.5 mm diameter round platinum wire sanded flush with the outer surface of a 1.8 mm hollow Teflon tube (see Figure A2-1). Once completed, test fibers were similar in shape and flexibility to Zeeweed-500 PVDF membrane fibers (see Figure A2-2) (Fulton *et al*., 2011).

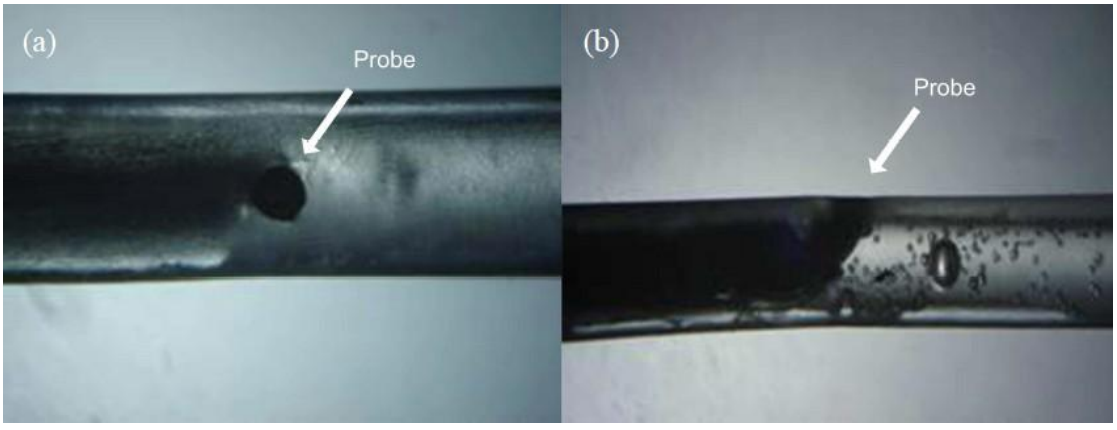

Figure A2-1 Top (a) and side (b) views of a shear probe on a test fiber.

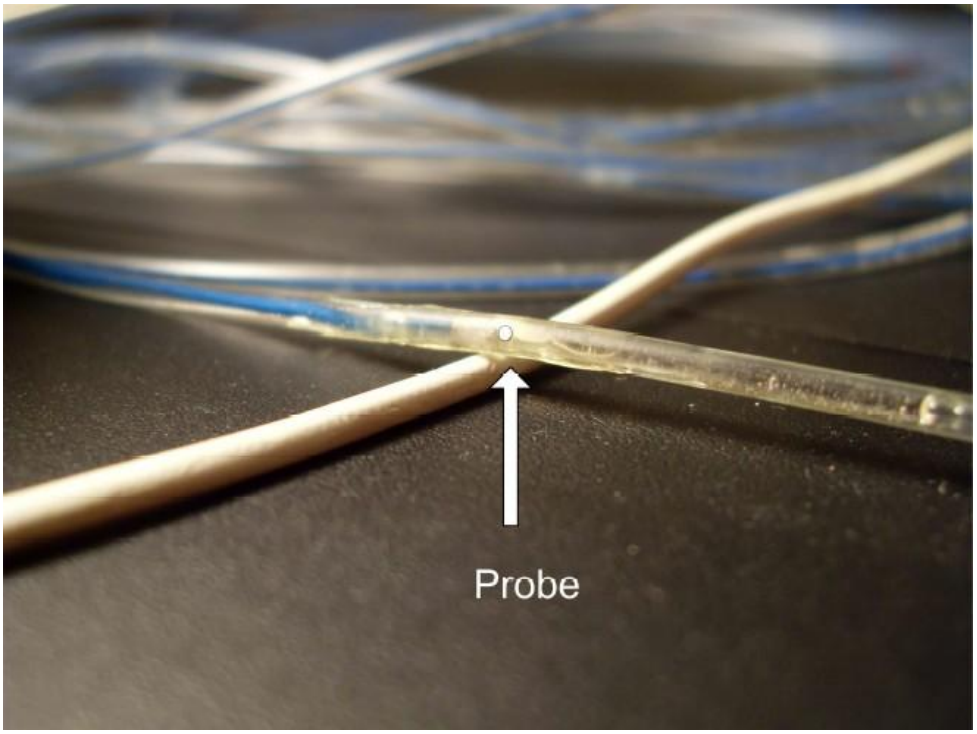

Figure A2-2. A test fiber shown with a Zeeweed-500 PVDF membrane fiber.

A1.2 Choice of Electrolyte

Ferri-ferrocynaide couple. There are four criteria determining the choice of electrolyte in the electrochemical shear measurement: 1) chemical stability, 2) high solubility, 3) electrode potential different from hydrogen, and 4) low cost (Selman and Tobias, 1978). The ferri-ferrocyanide electrolytic couple is commonly used with nickel or platinum since both metals are sensitive to the present of cyanide ions. The reaction at the working electrode (cathode) is:

$$Fe(CN)_6^{3-} + e^- \rightarrow Fe(CN)_6^{4-}$$

As there is no precipitation in the product of the reaction, this electrolytic couple is better than other couple that can produce precipitation on the probe surface, such as copper, which may cause the change of the shear probe surface area.

Concentration of inner salt. One of the assumptions in the limiting current equation is that the current generated by the migration effect due to the applied potential can be eliminated. For this reason, inert

salts such as NaCl, KCl are normally added in excess to reduce/eliminate the migration effect. The following equation can be used to determine the concentration of the salt solution required for a 1% migration current relative to the total migration current (Berger and Ziai, 1983):

$$I_{mig} = \frac{1}{2}\frac{C_i}{C_{salt}} I_t \quad \text{(A1-1)}$$

where I_{mig} is the migration current, I_t is the total current, C_i is the concentration of reacting species and C_{salt} is the concentration of inner salt. For example, for a 0.01M ferri and ferrocyanide solution, a concentration of 0.5M of salt solution is sufficient to reduce the migration current to 1% of the total current.

Special considerations during experiment. Special considerations are needed when preparing the electrolyte solution and during experiment, as discussed below,

i. Photochemical decomposition

Ferricyanide and ferrocyanide are sensitive to light and will undergo photochemical decomposition when exposed to light:

$$Fe(CN)_6^{4-} + H_2O \xrightarrow{light} Fe(CN)_5^{3-} + CN^- + H_2O$$

$$CN^- + H_2O \xrightarrow{light} HCN + OH^-$$

The decomposition byproduct, hydrogen cyanide (HCN), may poison the electro surface (Berger and Ziai, 1983). The decomposition of the ferri/ferrocyanide will also change the measured current and cause the error during the measurement. It is recommended that the solution not be exposed to light, and the solution be stored overnight in opaque container.

ii. Exposure to oxygen

Oxygen can oxdize ferricyanide and ferrocyanide if these are exposed to air. The oxidized ferricyanide and ferrocyanide byproducts may also poison the electrode surface (Berger and Ziai, 1983). In addition, the oxygen in the solution can react with the ferri/ferrocyanide. Isolation of the electrochemical system from air is recommended throughout the experiment and nitrogen gas can use to purge out the oxygen in the solution.

iii. Exposure to acid

The ferricyanide and ferrocyanide have very low toxicity. However, under strongly acidic conditions, highly toxic hydrogen cyanide gas can be released. This is possible to happen during the preparation of the solution in the lab where the strong acid can accidentally mix with the ferri/ferrocyanide solution. Make sure the absent of strong acid from the chemical throughout the experiment.

iv. Effect of temperature

Diffusivity of ferricyanide is sensitive to temperature changes. Berger and Ziai (1983) showed that a 3 ℃ temperature increase can result in a 20% increase in the limiting current of the system. It is important to monitor the temperature of the measurement system and keep the time of the measurement short enough to prevent significant change of the temperature.

Rosant (1994) showed that the 0.003 M ferricynaide and 0.006 M ferrocyanide had been successfully applied in electrochemical shear measurements. According to the equation 3-6 by applying the value of ferrocyanide concentration, 0.006 M, the 0.3 M potassium chloride was used as the inner salt. The actual chemical used to provide the ferrocyanide ion was potassium ferrocyanide trihydrate. Solvent used for the experiment is Reverse Osmosis water and three liters of solution was used in total. The physical properties of the electrolytes for the shear probe calibration were shown in Table A2-1.

Table A2-1. Physical properties of the electrolyte solution.

Compound	**Concentration (M)**	**Molecular weight (g/mol)**	**Amount**
Potassium ferricyanide ($K_3[Fe(CN)_6]$)	0.003	329.26	2.936g
Potassium ferrocyanide trihydrate ($K[Fe(CN)_6]\cdot 3H_2O$)	0.006	422.41	7.603g
Potassium chloride (KCl)	0.3	74.56	67.104g
Reverse Osmosis water	-	-	3L

Other physical properties at 20 ^{o}C (Rosant, 1994):

Density = 1016 kg/m^3

Viscosity = 0.001 kg/m/s

Ferricyanide diffusivity = 7.14 $\times 10^{-10}$ m^2/s

A1.3 Side Loop System Setup

The side loop membrane setup was built to create the well-controlled shear rate on the shear probe surface. Figure A2-3 and A2-4 presents an overview of the side loop system. There was a Plexiglas cylinder 1.2 m in length with an inner diameter of 0.025 m, within which ferri/ferrocyanide solution could be circulated using a Masterflex peristaltic pump. The flow could be varied from 0 - 3.5 liters/min, though only flow rates of 0.5 - 2.0 liters/min were used (equal to cross-flow velocities of 0.017 - 0.065 m/sec) to ensure laminar flow conditions. The Plexiglas cylinder was constructed such that a single test fiber (with shear probe) could be accurately placed at the centreline of the cylinder, resulting in an annular type geometry. The shear probe was located at the middle of the cylinder during the measurement. Figure A2-5 presents a the front view and the cross section view of the Plexiglas cylinder and the test fiber.

Nitrogen gas was used to purge out the oxygen from the solution before the calibration. A fine bubble diffuser was placed inside the electrolyte reservoir to increase the efficiency of the purging. The dissolve oxygen (DO) meter was used to monitor the temperature and the oxygen content of the electrolyte solution. The electrical circuit in the system is discussed in section A1.4.

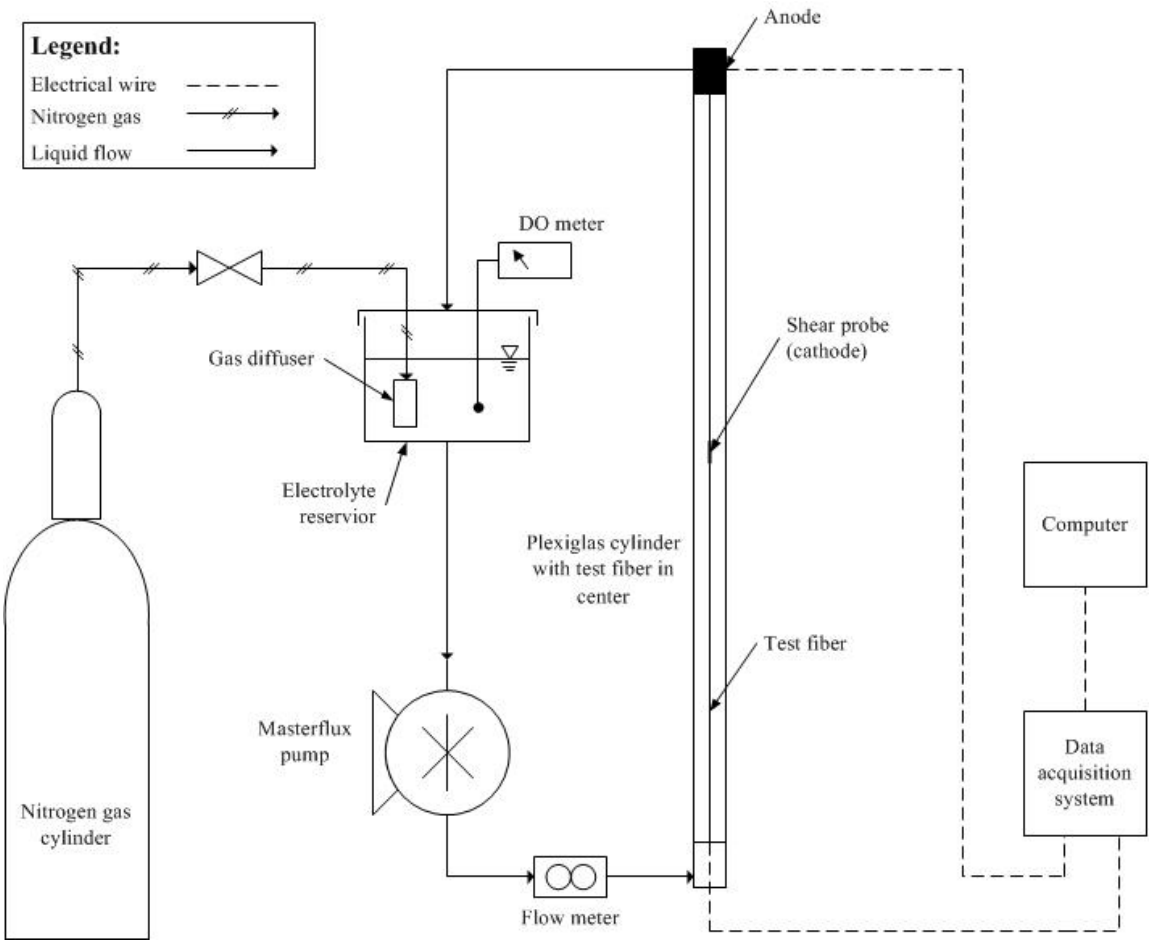

Figure A2-3. The schematic diagram of the side loop system setup.

Figure A2-4. Photo of the Plexiglas column used in the side loop setup.

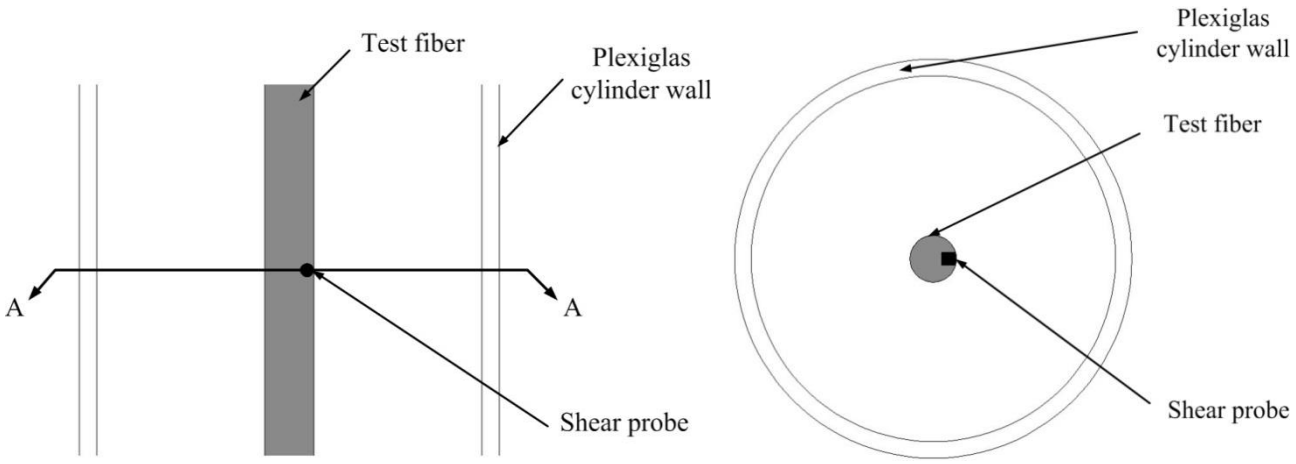

Figure A2-5. (a) Side view of the Plexiglas cylinder with the test fiber and shear probe. (b) Cross section A-A of the Plexiglas cylinder with the test fiber and shear probe.

A1.4 Electrical Circuit

The cathode of the electrochemical system was the shear probe, and the anode was a piece of stainless steel pipe fitting located on one end of the Plexiglas cylinder (Figure A2-3). The surface area of the stainless steel fitting was much larger than the surface area of the probes to insure the limiting diffusion conditions only occured on the shear probe surface. The power supply between the anode and cathode was adjustable. Before the calibration, limiting current test was carried out to make sure that the applied voltage was in Zone II as discussed before. The test result showed that the current didn't change when voltage increase from 400 mV to 600 mV. As a result, the voltage was set to 500 mV for the calibration test. During the measurement, the current in the circuit passed through a 100 Ω resistor. The voltage drop across the resistor was measured and amplified (gain =1000). The data acquisition system acquired the signals and recorded real time using a custom Labview application. Data acquisition frequency was adjustable and 1000 Hz acquisition frequency was used for the steady-stay calibration of the two test fibers. Figure A2-6 presents a schematic diagram of the electrical circuit in the side loop setup.

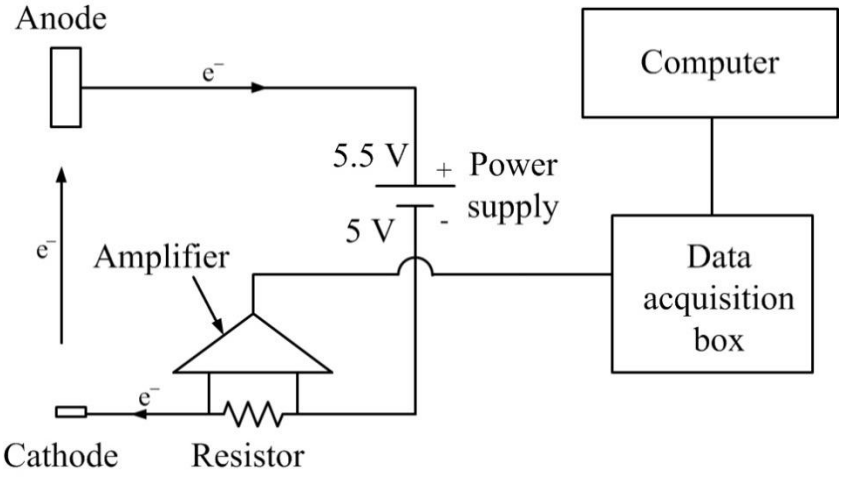

Figure A2-6. The schematic diagram of the electrical circuit in the side loop setup.

A1.5 Calibration Procedure and Results

Before the shear stress measurements were taken, the prepared electrolyte solution was purging by nitrogen gas for about 15 minutes until the oxygen saturation of the solution reduced to less than 7% to minimize the effect of oxygen. The two shear probes were thoroughly washed using de-ionized water and Kimwipes® (non-abrasive laboratory-grade paper towel) to ensure their cleanliness. As each time only one test fibre can be placed in the Plexiglas cylinder, the measurement of the actual limiting current was carried out sequentially. In addition, the four different flow rates (0.5, 1.0, 1.5, 2.0 L/min) of the pump were calibrated by a stop watch and a measurement cylinder.

During the measurement, steady-state calibration was carried out first. Four corrected flow rates were used and the data for each flow rate was recorded. Each flow rate was operated for about 1 min to ensure the steady state condition and the sampling period was about 10 seconds. Temperature was closely monitored as it can significantly affect the value of limiting current. Appendix 3 presents the relationship between the temperature and the theoretical coefficient of the limiting current. Appendix 4 presents the detail of the calculations and results. After the steady-state calibration, the voltage-step calibration was also carried out. This was done by switching off the applied voltage first, and then began the signal recording. About 3 seconds later, the applied voltage was switched back on. The measured voltage will have a sudden increase and then decrease to stable value. This transient behavior was recorded for 5 seconds. The conversion between the steady-state calibration coefficient and voltage-step calibration coefficient is presented in Appendix 6.

After the measurements, the shear probe was washed using de-ionized water and Kimwipes® immediately. The corrected data was analysed and the average calibration factor for each probe was obtained. Then the two test fibres were ready for the shear measurement in the full length membrane module. The results of steady-state calibration are presented in Appendix 5. The results of the voltage-step calibration were presented in Appendix 7.

Calibration was done again after the shear stress measurements were completed to examine if the properties of the shear probes had changed over time.

As one of the quality control method, voltage-step calibrations were performed in the large scale system.

APPENDIX 3. THE EFFECT OF TEMPERATURE TO LIMITING CURRENT

Temperature will affect the viscosity of the water as well as the diffusion rate of the ion. It is important to correct the temperature effect of the system to avoid error in the experiment. In this thesis, two assumptions were made for correcting the temperature effect. The first one is that viscosity changes linearly with the temperature. As the temperature range of all the experiments is quite small (17-23 ℃), we assume that viscosity changes linearly in this range. The second one is that the value of the product between the diffusion coefficient and the dynamic viscosity overs the temperature is constant (Legrand *et al.*, 2000),

$$\frac{D\mu}{T} = \text{constant} \qquad \text{(A3-1)}$$

The data from Gaucher *et al*. (2002) was used as a standard value at 30 ℃ and we assume the solution at 20 ℃ has a same viscosity as water. The shear probe diameter is assumed as 0.0005 m and the concentration is 3 mol/m^3. The theoretical coefficient values of a ferri/ferrocyanide solution were calculated in the Table A3-1.

Table A3-1. Theoretical coefficient values of the electrochemical solution under different temperatures

Temperature (℃)	Temperature (K)	Viscosity (Pas)	Diffusion Coefficient (m^2/s)	Leveque coefficient K_{Lev}	Cottrell coefficient K_{Cot}
30	303.15	8.1300E-04	8.3600E-10	5.4777E-07	9.2713E-07
29	302.15	8.3190E-04	8.1431E-10	5.3826E-07	9.1502E-07
28	301.15	8.5080E-04	7.9359E-10	5.2908E-07	9.0330E-07
27	300.15	8.6970E-04	7.7376E-10	5.2024E-07	8.9195E-07
26	299.15	8.8860E-04	7.5478E-10	5.1169E-07	8.8094E-07
25	298.15	9.0750E-04	7.3659E-10	5.0344E-07	8.7026E-07
24	297.15	9.2640E-04	7.1914E-10	4.9546E-07	8.5989E-07
23	296.15	9.4530E-04	7.0239E-10	4.8773E-07	8.4982E-07
22	295.15	9.6420E-04	6.8630E-10	4.8025E-07	8.4003E-07
21	294.15	9.8310E-04	6.7083E-10	4.7301E-07	8.3050E-07
20	293.15	1.0020E-03	6.5594E-10	4.6598E-07	8.2123E-07
19	292.15	1.0209E-03	6.4160E-10	4.5917E-07	8.1221E-07
18	291.15	1.0398E-03	6.2778E-10	4.5255E-07	8.0341E-07
17	290.15	1.0587E-03	6.1445E-10	4.4612E-07	7.9484E-07
16	289.15	1.0776E-03	6.0160E-10	4.3988E-07	7.8648E-07

With this table, after we measured the limiting current and the corresponding shear stress, we would be able to calibrate the shear probe.

APPENDIX 4. SHEAR RATE IN THE SIDE LOOP SETUP

The flow condition in the side loop column is an annulus flow from bottom to top (Figure A2-5). Figure A4-1 shows the cylindrical coordination for the annulus flow in the side loop column.

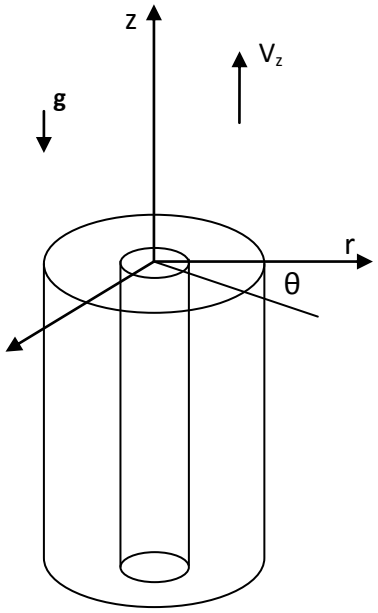

Figure A4-1. Cylindrical coordination for the annulus flow

We assume the flow is parallel with the wall and flow is in steady state, so $V_r = V_\theta = 0$ and $\partial V_z / \partial z = 0$. Also, for steady, axisymmetric flow, V_z is not a function of θ. So the velocity, V_z, is only a function of the radial position within the tube, that is $V_z = V_z(r)$. Under these conditions, the Navier–Stokes equations become

$$0 = -\frac{\partial p}{\partial r} \qquad \text{(A4-1)}$$

$$0 = -\frac{1}{r}\frac{\partial p}{\partial \theta} \qquad \text{(A4-2)}$$

$$0 = -\frac{\partial p}{\partial z} - \rho g + \mu\left[\frac{1}{r}\frac{\partial}{\partial r}\left(r\frac{\partial V_z}{\partial r}\right)\right] \qquad \text{(A4-3)}$$

Equation (A4-1) and (A4-2) indicate that pressure is not a function of r or θ, and the pressure is constant at any particular cross section, and the z component of the pressure gradient, $\partial p / \partial z$, is not a function of

r or θ as well. So now we can integrate equation (A4-3) and treat $\partial p/\partial z$ as constant in the integration. The result of the integration is:

$$V_z = \frac{1}{4\mu}\left(\frac{\partial p}{\partial z} + \rho g\right) + C_1 \ln r + C_2 \qquad \text{(A4-4)}$$

where C_1 and C_2 are integration constant. By applying the boundary condition that, at the wall r_o, the velocity is zero and at the fiber surface r_i, the velocity is also zero. The equation will become:

$$V_z = \frac{1}{4\mu}\left(\frac{\partial p}{\partial z} + \rho g\right)\left[r^2 - r_o^2 + \frac{r_i^2 - r_o^2}{\ln\frac{r_o}{r_i}} \ln\frac{r}{r_o}\right] \qquad \text{(A4-5)}$$

Integrating V_z from the r direction; we get the flow rate:

$$Q = -\frac{\pi}{8\mu}\left(\frac{\partial p}{\partial z} + \rho g\right)\left[r_o^4 - r_i^4 - \frac{(r_o^2 - r_i^2)^2}{\ln\frac{r_o}{r_i}}\right] \qquad \text{(A4-6)}$$

The shear rate is defined as the change of the velocity, so $\gamma = \frac{\partial V_z}{\partial r}$. We can differentiate equation (A4-5) respected to r and get:

$$\gamma = \frac{\partial V_z}{\partial r} = \frac{1}{4\mu}\left(\frac{\partial p}{\partial z} + \rho g\right)\left[2r + \frac{r_i^2 - r_o^2}{r \ln\frac{r_o}{r_i}}\right] \qquad \text{(A4-7)}$$

If we know the flow rate Q, we can use equation (A4-6) to fine the pressure drop $\frac{\partial p}{\partial z} + \rho g$ and then calculate the shear rate from equation (A4-7). And the Shear rate γ can be calculated as

$$\gamma = -\frac{2Q}{\pi} \frac{\left[2r + \frac{r_i^2 - r_o^2}{r \ln\frac{r_o}{r_i}}\right]}{\left[r_o^4 - r_i^4 - \frac{(r_o^2 - r_i^2)^2}{\ln\frac{r_o}{r_i}}\right]} \qquad \text{(A4-8)}$$

In the side loop system, r_o = 0.025 m and r_i = 0.0018 m. As we only interested in the shear rate at the probe surface, we let the $r = r_i$ in equation (A4-8). For a given flow rate Q, we would be able to find out

the theoretical γ. In the experiment, four different flow rates were used, 0.5, 1.0, 1.5 and 2 L/min. As the flow rate is critical to calculate the shear rate, the four flow rates were calibrated by a stop watch and a measurement cylinder. Table A4-1 shows the corresponding shear rate of the given flow rate.

Table A4-1. Shear rate γ under given flow rate.

Designed flow rate (m^3/s)	Measured flow rate (m^3/s)	Shear rate (s^{-1})
8.33E-06	8.28E-06	22.09
1.67E-05	1.67E-05	44.44
2.50E-05	2.46E-05	65.76
3.33E-05	3.26E-05	87.02

One thing to note that all the assumption is based on the laminar flow condition. By checking the Relynos number in the system, the maximum flow rate to maintain laminar flow in the cylinder is about 21.5 L/min, which would be ten times larger than the flow rate used in the experiment. So the laminar flow assumption is valid.

APPENDIX 5. SIDE LOOP STEADY-STATE CALIBRATION RESULTS

Combing the theoretical value of shear rate and Leveque coefficient, we can use equation A1-5 to calculate the theoretical limiting current. For example, if the flow rate is 3.26E-05 m^3/s and the temperature is 20 ℃, the shear rate would be 87.02 s^{-1} and K_{Lev} = 4.6598E-07 A $s^{1/3}$. Applying equation A2-5,

$$I_{standard} = 4.6598E\text{-}07 \times (87.02^{1/3}) = 2.065E\text{-}06 \text{ A}.$$

What we measured in the experiments was not the current but the voltage. Referring to figure A2-6, the voltage we get was the current times the resistant 100 Ω and times the amplifier gain 1000,

$$V_{standard} = IR \times 1000 = 2.065E\text{-}06 \times 100 \times 1000 = 0.2065 \text{ V}.$$

Under four different flow rates we will get four measured value, then we can get the ratio between the theoretical value and the measurement value called α, so that $V_{standard} = \alpha V_{measure}$. The α was also called steady state calibration coefficient in this thesis. The calibration experiments were done in triplicate and averaged value of α before and after the experiments are presented in Table A5-1.

Table A5-1. Steady-state calibration results of the shear probe before and after the experiments.

Q (m^3/s)	Probe 1 α		Probe 2 α	
	Before	After	Before	After
8.28E-06	8.413E-01	8.667E-01	7.060E-01	7.088E-01
1.67E-05	8.300E-01	8.978E-01	7.002E-01	6.928E-01
2.46E-05	8.127E-01	8.926E-01	6.726E-01	6.711E-01
3.26E-05	7.950E-01	8.989E-01	6.506E-01	6.780E-01
Average value	8.197E-01	8.890E-01	6.823E-01	6.877E-01

The results showed that two probes remained consistent conditions throughout the study. This gave us the confidence that the experiment data is reliable.

APPENDIX 6. CONVERSION BETWEEN STEADY-STATE CALIBRATION COEFFICIENT AND VOLTAGE-STEP CALIBRATION COEFFICIENT

The different between the measured voltage and the theoretical voltage is due to the difference in probe area if other conditions are all the same, referring to the equation A1-1 and A1-2, the steady state calibration coefficient α can be expressed as:

$$\alpha = \frac{V_{standard}}{V_{measure}} = \frac{I_{standard}}{I_{measure}} = \frac{nFAckD^{2/3}d^{-1/3}\gamma^{1/3}}{nFA'ckD^{2/3}d'^{-1/3}\gamma^{1/3}} = \frac{Ad^{-1/3}}{A'd'^{-1/3}} = \frac{1/4\pi d^{5/3}}{1/4\pi d'^{5/3}} = \frac{d^{5/3}}{d'^{5/3}} \qquad \text{(A6-1)}$$

where d' is the actual diameter of the probe. Referring to the equation A1-6 and A1-7, the voltage-step calibration coefficient β can be expressed as:

$$\beta = \frac{K_{Cot\text{-}standard}}{K_{Cot\text{-}measure}} = \frac{nFAcD^{1/2}\pi^{-1/2}}{nFA'cD^{1/2}\pi^{-1/2}} = \frac{A}{A'} = \frac{1/4\pi d^2}{1/4\pi d'^2} = \frac{d^2}{d'^2} \qquad \text{(A6-2)}$$

Combining equation A6-1 and A6-2, we can easily get that $\alpha = \beta^{5/6}$. This helps us to compare the calibration result between steady-state calibration and voltage-step calibration.

APPENDIX 7. VOLTAGE-STEP CALIBRATION RESULTS

The voltage-step calibration was periodically performed throughout the study to monitor the property of the electrolyte. When there was a change of the sparging tank and the electrolyte needed to be drained and refilled, the calibration would be done. In the following table, all the voltage-step calibration results were presented.

Table A7-1. Voltage-step calibration results.

	Probe 1		Probe 2	
	β	α	β	α
Side loop(before)	0.951	0.959	0.779	0.812
Throughout the entire experiment	1.199	1.163	0.832	0.858
	1.095	1.079	0.694	0.738
	1.004	1.003	0.619	0.671
	1.004	1.003	0.833	0.859
	0.988	0.990	0.711	0.753
	1.147	1.121	0.811	0.840
	1.024	1.020	0.723	0.763
	1.067	1.055	0.797	0.828
	1.052	1.043	0.755	0.792
	1.119	1.098	0.734	0.773
	1.113	1.093	0.791	0.823
	0.998	0.998	0.714	0.755
	0.999	0.999	0.748	0.785
Side loop(after)	0.983	0.986	0.714	0.755
Average	1.049	1.041	0.751	0.787

The two averaged α value from the voltage-step calibration results are slightly larger than from the steady-state calibration results. The voltage-step calibration helps to exam the condition of the probes and the electrolyte throughout the entire experiment.

APPENDIX 8. EXPERIMENTAL PROCEDURES FOR THE SHEAR STRESS MEASUREMENT

The volume of the electrolyte required in the D14 tank was about 32 L and for the D20 tank was about 60 L. Slightly more electrolyte solution was prepared to cover the volume of the pipe and in case of any leakage. The concentration of each chemical was the same as listed in Appendix 2. Due to the large amount of water required, the solute used in the D20 tank was tap water instead of RO water. Because there were a lot of solution and many experimental runs to be carried on, it was important to monitor the condition of the solution. The following experiment procedure was developed to ensure the quality of measurement results.

1) Clean the two shear probes using de-ionized water and Kimwipes® before put the membrane module into the sparging tank.
2) Open the valve on top of the electrolyte reservoir, and then open the nitrogen gas line connected to the diffuser in the reservoir. Use the master flux pump to pump the solution into the reservoir.
3) Keep the nitrogen gas going for about 10 mins to purge out the oxygen in the water. After that, turn on the nitrogen gas line connected to the sparging tank, and then turn on the pump to start pumping the electrolyte to the sparging tank.
4) When the tank was filled, turn off the both line nitrogen gas line as well as the pump. Turn off the valve on top of the electrolyte reservoir. Use the DO meter to check the oxygen saturation. If the oxygen saturation is larger than 7%, turn on the nitrogen gas line connected to the sparging tank again. Monitor the DO value until it reaches less than 7%.
5) After turn on the nitrogen gas line connected to the sparging tank, adjust the pressure regulator to 15 psi and set the flow rate to 8000 ml/min. After that, do the limiting current test under the higher flow rate condition and make the necessary adjustment.
6) Do the voltage-step test. After that start sampling. The sampling period for each experiment run would be 1 min. Change the air flow pattern and air flow rate and do the test again. These two conditions can easily be changed without empty the sparging tank. Keep the pressure at 15 psi all the time. In addition, there was also not requirement to empty the sparging tank if want to switch between fine bubble diffuser and coarse bubble diffuser.

7) When there is a need to change conditions of the tank setup, bulk flow pattern, bundle slackness as well as the switch of pulse diffuser, the electrolyte need to be pumped back to reservoir. Open the valve on top of the electrolyte reservoir and turn on the nitrogen gas line connected to the diffuser in the reservoir. Use the master flux pump to pump back the solution into the reservoir. After that, turn off the valve on top of the electrolyte reservoir and the nitrogen gas line connected to the diffuser in the reservoir.
8) When changing the setup of the sparging tank, use the de-ionized water and Kimwipes® to wash the shear probes.
9) After change the setup of the sparging tank, turn on the valve on top of the electrolyte reservoir and the nitrogen gas line connected to the diffuser in the reservoir. Turn on the nitrogen gas line connected to the sparging tank and then turn on the pump to start pumping the electrolyte to the sparging tank.
10) Repeat the step (4), (6), (7), (8) and (9) until all the conditions were tested (step (5) only do once at the beginning of the experiment).

The electrolyte solution was stored in an opaque reservoir when not in use. The voltage-step was carried out when there was a change of the sparging tanks setup or when it was felt necessary.

After the measurements, the shear probe was washed by de-ionized water and Kimwipes® immediately. The corrected data was analyzed and the average calibration factor for each probe was obtained. Then the two test fibres would be removed from the membrane module, and moved back to the side loop setup to do the calibration again. This was to examine the quality of the shear probes. The results of the voltage-step calibration were shown in Appendix 7. With those results, we were able to track the quality of the shear probes as well as the quality of electrolyte.

APPENDIX 9. EXPERIMENTAL PROCEDURE FOR FILTRATION TEST

For the filtration test, the following procedures were developed to ensure the stable performance of the membrane.

1) After the active membrane fibers were assembled (see section 3.1.2), an integrity test was performed. This was done by submerging the active membrane fibers into a water tank, and using the permeate pump (in a reverse flow direction) to slowly add air into the fibers to achieve a pressure of 3 psi. If the pressure drop inside the active membrane fibers was less that 2 % in 5 mins, the membrane fibers will be considered not to be breached. If the pressure drops significantly, new active membrane fibers need to be assembled.
2) If the active membrane fibers pass the integrity test, the membrane module can be assembled (section 3.1.2). After the module is assembled, a second integrity test is performed to ensure that the active membrane fibers were not damaged.
3) Place the membrane module in the system tank and turn on the permeate pump. Set the flow rate of the pump to 60 mL/min and measure the initial TMP of the membrane. At the room temperature of approximately 22 ℃, the TMP for clean water should be approximately 4.5 psi.
4) Prepare the bentonite solution. Measure the amount required for the filtration test. For the D14 tank, 8 g bentonite is required and for the D20 tank 15 g is required. Use a small container of approx. 3 L to prepare a bentonite slurry and make sure that all the bentonite power is dispersed. Hot water can be used to accelerate the dispersing process. Approximately 10 – 15 mins are required before the bentonite becomes fully disperse.
5) Use the tap water to rinse the container and then transfer the rinse water to the tank. Do this 3 times to make sure that all bentonite has been transferred into the tank. Fill up the tank with tap water. Turn on the air to mix the solution and make sure that the temperature of water in the tank is approx. 22 -27 ℃.
6) When the bentonite solution is ready, the filtration test can be started. Use the pressure regulator and the flow meter to adjust the flow rate of the sparging air. The pressure regulator was set to 15 psi. And the air flow rate is adjusted for different experiment conditions. The flow rate of the permeate pump is set to 60 mL/min. Use the pressure transducer and data logger to record the

pressure change in the permeate line. Stop the filtration when the TMP reach 10 psi. If after 160 mins and the TMP still doesn't reach the 10 psi, the experiment will also stop.

7) After the membrane is fouled (i.e. at the end of the filtration test), a backwash is performed. The bentonite solution is drained from the tank which is then fill up with clean water from hot water tap (temperature 40 ℃). The system is then backwashed. A relatively low flow rate is used during backwash so that the pressure does not exceed 3 psi. An air flow rate of 10000 mL/min is used during the backwash. After 10 mins, the tank is drained and it is then filled up again with hot water. A second backwash is then performed and tank is drained after.
8) The tank is then filled up with tap water and a clean water test is performed. A mixture of cold and hot tap water is used to achieve a water temperature of approximately 22-27 ℃ in the tank. In filtration mode, monitor the TMP when filtering clean water. If the TMP is larger than 4.5 psi, clean the membrane again. If the TMP is significantly less than 4.5 psi, do the integrity test to check any leakage. When the TMP is approx.. 4.5 psi, the membrane is considered to be clean and next filtration test can begin.
9) As the filtration experiments lasted for a few weeks, there was the possibility that bacterial growth occurred in/on the membrane. If the clean water TMP is greater than 4.5 psi and backwash could not reduce it, a chemical cleaning was performed. This was done by soaking the membrane module in a bleach solution with a concentration of 1000 ppm for 16 hours. After 16 hours, a 100 ppm bleach solution was filtered for 30 mins. The fibers were then rinsed by filtering with clean water for another 30 mins. A chemical cleaning was usually performed every other week.
10) Integrity tests were done every other week as well as at the end of the filtration test to ensure the membrane integrity was not compromised.

APPENDIX 10. QA/QC RESULTS

A10.1 QA/QC Results for Shear Stress Measurement

Calibration was one of the most important quality control methods during the shear stress measurement. It helped to monitor the quality of the shear probe as well as the electrolyte. The calibrations for the shear probes in D14 and D20 experiments were done separately due to the different time and location of these two experiments. A parameter, α, was introduced as the calibration coefficient which indicated the different value between the measured value and the standard value. For the full definition of α, please refer to appendix 5. The calibration results for D14 and D20 were presented separately.

A10.1.1 Calibration results of the shear probes in D-140 tank experiments

Referring to appendix 5 table A5-1, under different flow rate the α value remained relatively constant. As α did not relate to the change of flow rate, this result gave us the confidence that the system and the shear probe was in stable conditions. Compared the α between probe 1 and probe 2, probe 1 has a bigger α than probe 2, which means that, probe 2 has a larger diameter than probe 1. The results between before and after the shear measurement showed that, there was a small increase of α. For probe 1 was 8.5% and for probe 2 was 0.8%. This may due to the different bulk chemical concentration or some effect of electro-field in the surrounding environment. But according to equation A1-1, the limiting current is the product of the K_{Lev} and $\gamma^{1/3}$. For the calibration, we try to calibrate the effect of K_{Lev}. And in the shear measurement, the different of the shear rate can be 10-100 times. So only a 8% different of the α value would not really effect the result of the limiting current we were measuring. We would consider that the probe was in a relatively stable condition throughout the experiment.

For the voltage-step calibration, the following graph was generated from appendix 7 table A7-1.

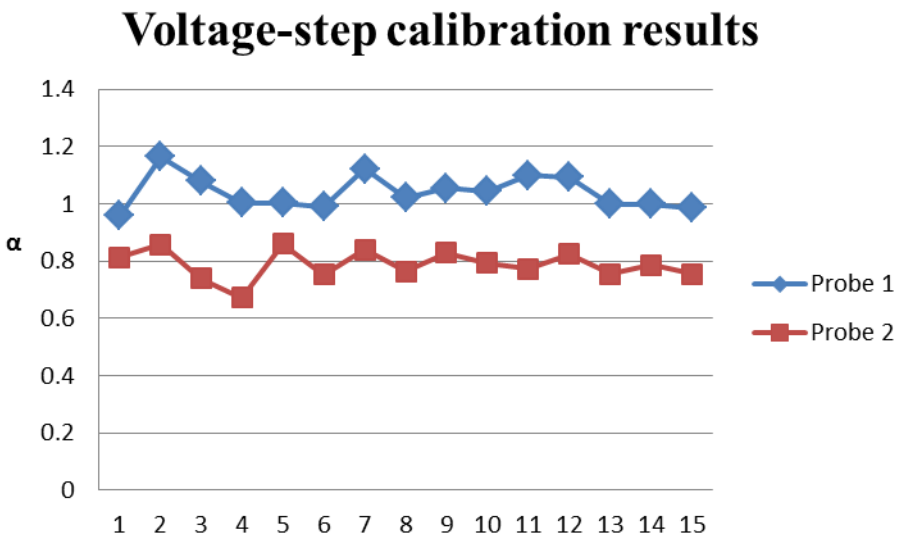

Figure A10-1. Voltage-step calibration results throughout the experiment.

Throughout the study, there were 15 voltage-step calibrations performed. From the figure we could tell that the α value remained stable throughout the experiment. The small variation is likely due to experimental errors. This indicated that the characteristics of the electrolyte remained stable from begin to the end and the electrolyte was well kept in a oxygen free environment.

Table A10-1 presents the combination of results of the steady-state calibration and voltage-state calibration. In the table, the average α values for probe 1 and probe 2 under different calibration methods were presented. From the table we can see that steady-state calibration would give us lower α value than voltage-step calibration. This may due to the different assumptions and other factors that cannot be quantified. For example, the steady-state calibration assumes that the shear probe was at the centre of the plexigals cylinder. This may not be true in the real situation. In addition, the shear probe surface may be not perfectly smooth and circular shape. For the voltage-step calibration, we need to choose the target time interval for the linear regression, but the choice of this time interval is still under research, different time interval would lead to different K_{Cot} value. All of these can lead to small errors of calibration. However, small differences of the α doesn't really effect the measurement results since we average the value between steady-state and voltage-step calibration and would use these two number for the following calculation and discussion.

Table A10-1. Summary of the steady-state and voltage-step calibrations in D14 tank.

	Probe 1 α	Probe 2 α
Steady-state	0.854	0.685
Voltage-step	1.041	0.787
Average	0.948	0.736

A10.1.2 Calibration results of the shear probes in D20 tank experiments

The voltage-step calibration results of the two shear probes in the D20 tank were presented in Table A10-2.

Table A10-2. Voltage-step calibration results of the probe 1 and probe 2 in D20 tank.

Probe 1 α	Probe 2 α
0.872	0.622

A10.2 QA/QC Results for Filtration Test

The data obtained from the pressure transducer was actually a voltage measurement. To convert the voltage signal to pressure, a calibration was done. The results are presented in Figure A10-2. The calibration was done again after the filtration process to make sure that there was not significant change of the pressure transducer.

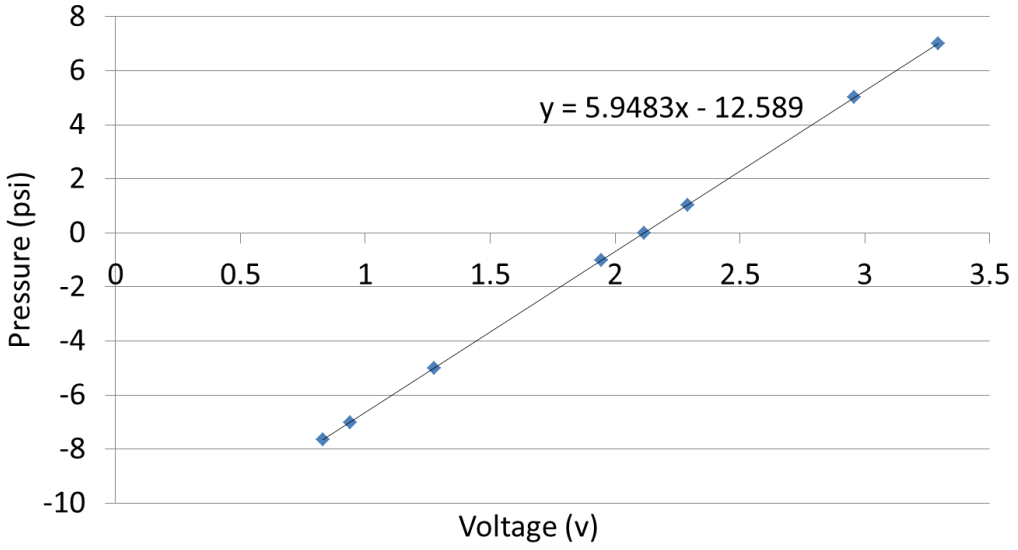

Figure A10-2. Calibration of the pressure transducer

Particle size distribution of the bentonite solution was measured (Figure A10-3). From the figure we can see that peak size distribution happened in the size range from 0.631 to 0.724, which is 14.04% of the total number of the particle. The detectable particle size was about 0.4 μm. This is 10 times larger than the membrane pore size which is about 0.04 μm. The bentonite particle would not likely to go inside the membrane.

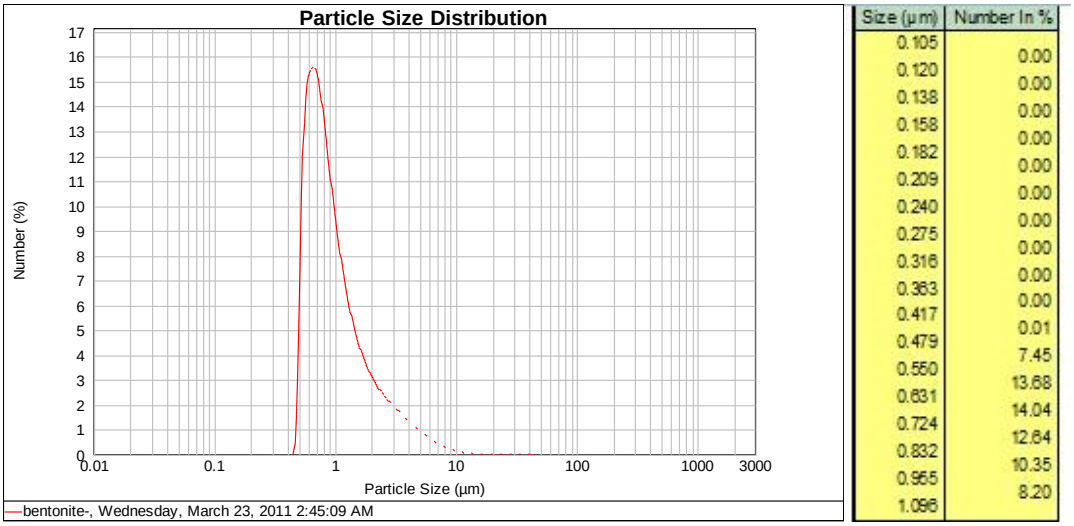

Size (μm)	Number In %
0.105	0.00
0.120	0.00
0.138	0.00
0.158	0.00
0.182	0.00
0.209	0.00
0.240	0.00
0.275	0.00
0.316	0.00
0.363	0.00
0.417	0.01
0.479	7.45
0.550	13.68
0.631	14.04
0.724	12.64
0.832	10.35
0.955	8.20
1.096	

Figure A10-3. Particle size distribution of the bentonite solutions.

Temperature throughout the whole experiment was carefully monitored. The thermometer was used to check the temperature in the tank. The ratio between the cold water and hot water was about 3:4. After the mixing, the temperature was checked and if the temperature was too high or too low, the air would be turned on to mix up the water, which was to help the temperature in the tank reach the room

temperature. The initial temperature and final temperature of each filtration run was recorded and the different between them was within 1 ℃. The room temperature was around 24 ℃. For all the tests, the recorded temperature was between 22.9 to 26.9 ℃. As a result, the effect of the viscosity different was minimized.

There were altogether six integrity tests done throughout the entire filtration experiments. All the pressure drop was less than 0.05 psi when pressurized the membrane to 3 psi. Due to the diffusion of the gas into the water, slightly pressure drop was reasonable and we assume that the fiber was not leak throughout the experiment.

APPENDIX 11. SHEAR STRESS MEASUREMENT RESULTS IN D14 TANK

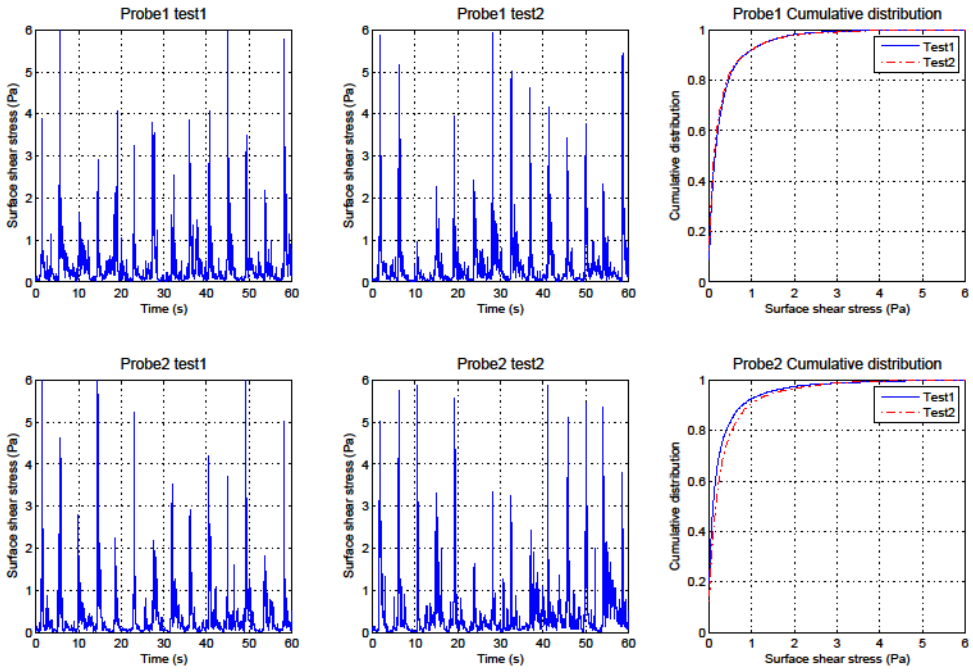

Figure A11-1. Result of PLOSC1.3.

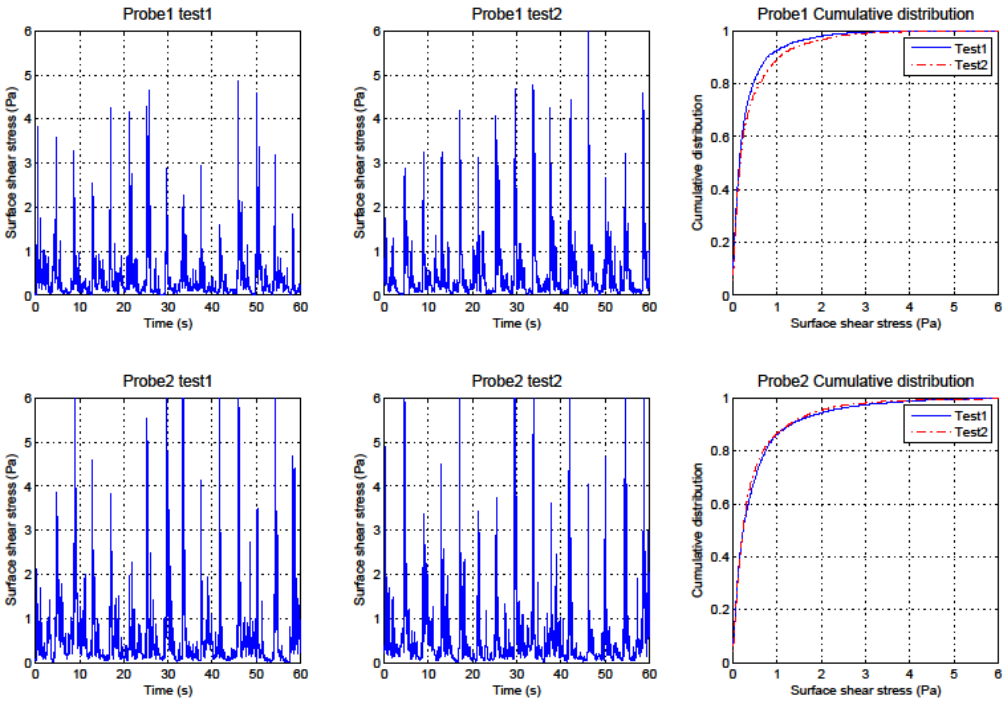

Figure A11-2. Result of PLOSC2.2.

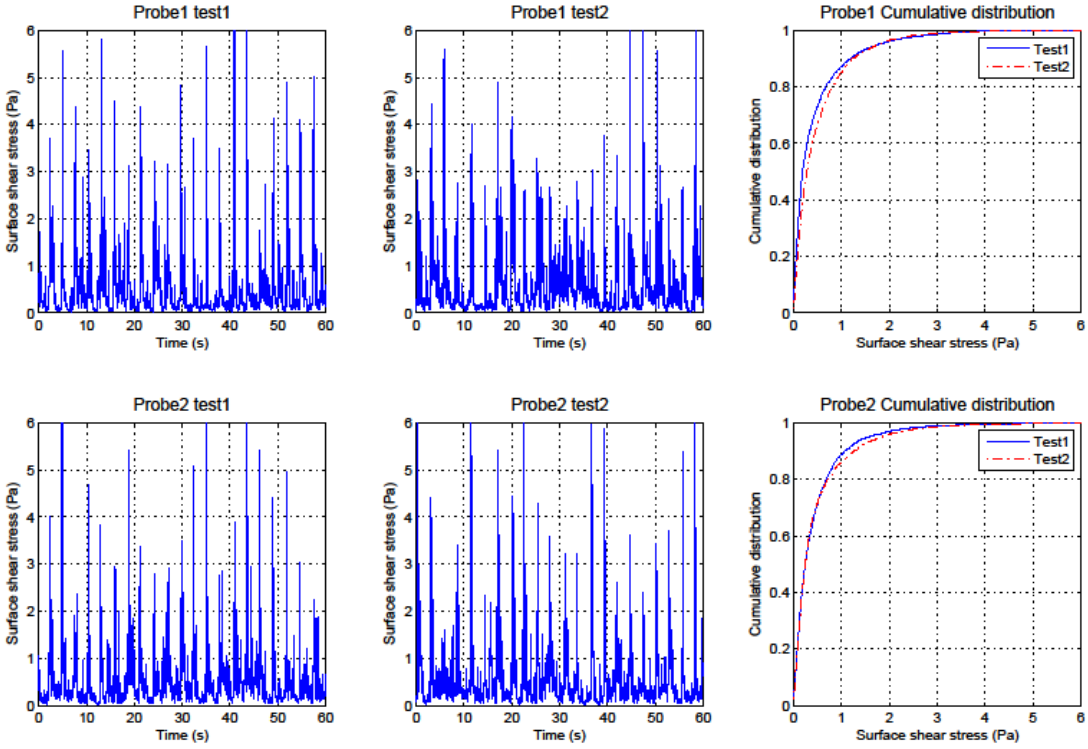

Figure A11-3. Result of PMOSC1.3.

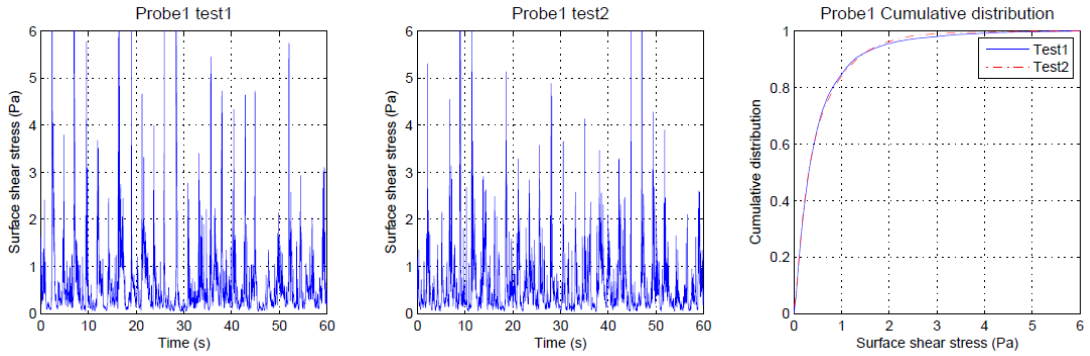

Figure A11-4. Result of PMOSC2.2.

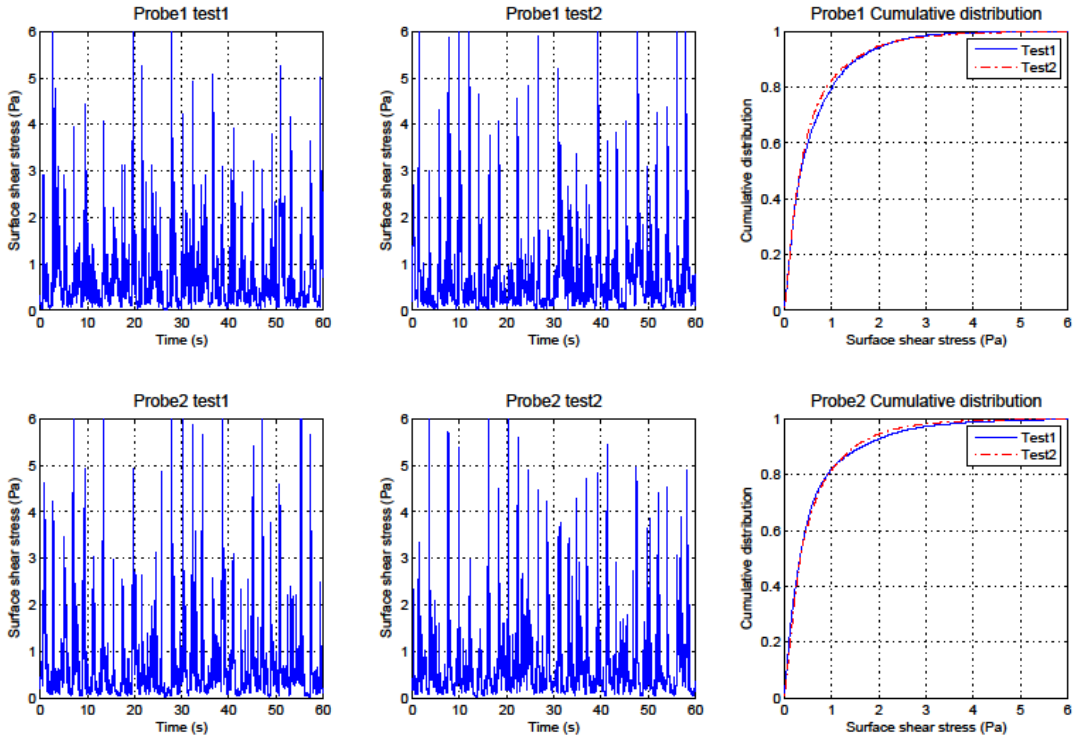

Figure A11-5. Result of PHOSC1.3.

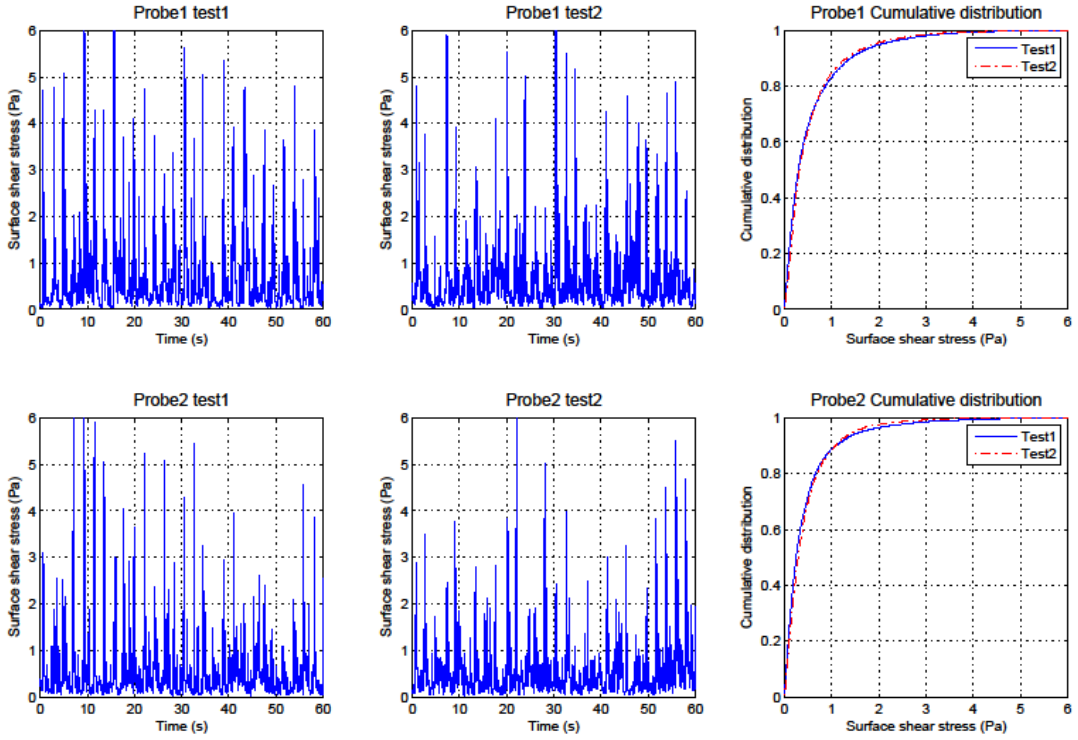

Figure A11-6. Result of PHOSC2.2

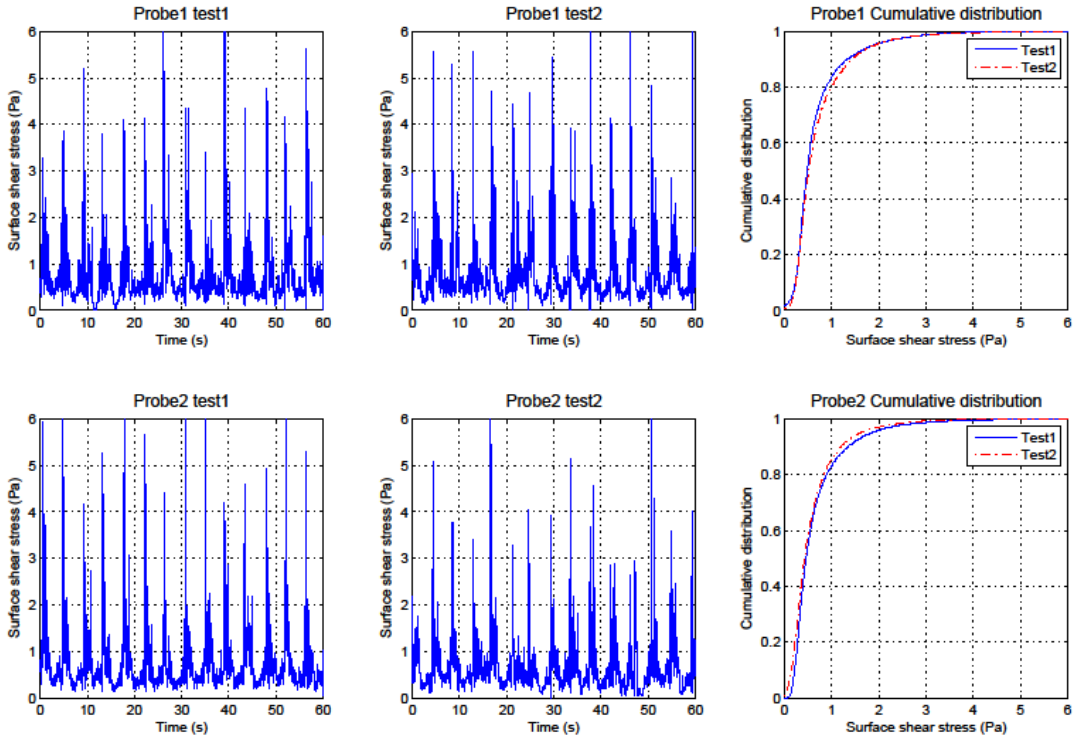

Figure A11-7. Result of PLWSC1.3.

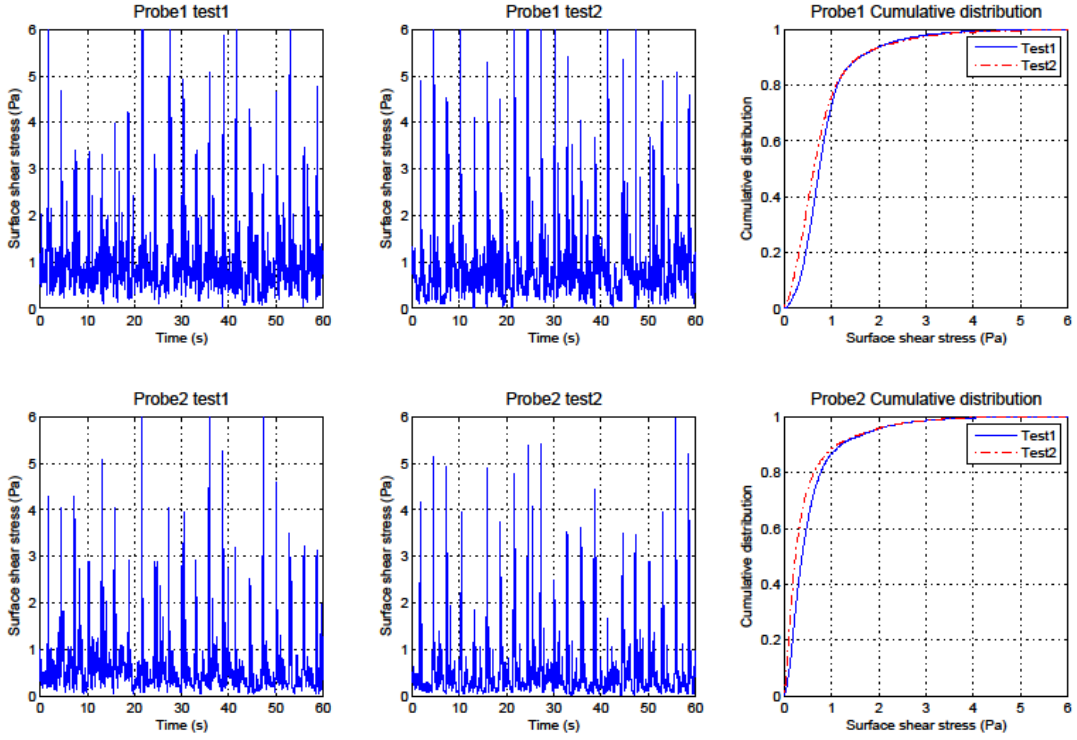

Figure A11-8. Result of PMWSC1.3.

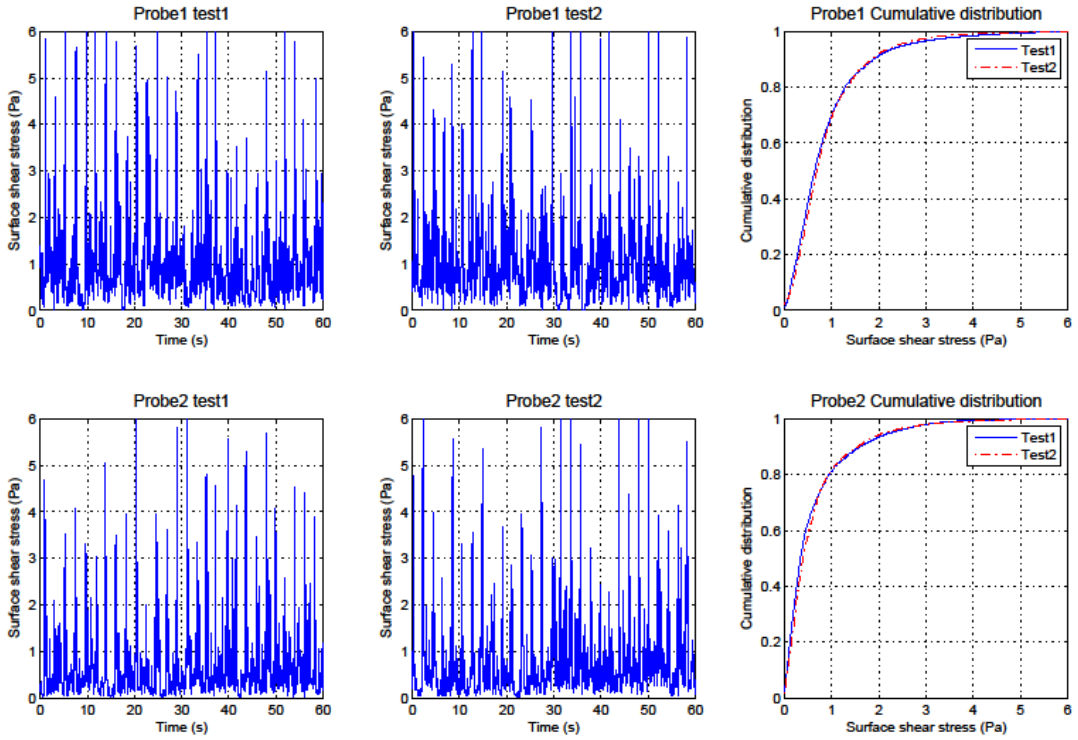

Figure A11-9. Result of PHWSC1.3.

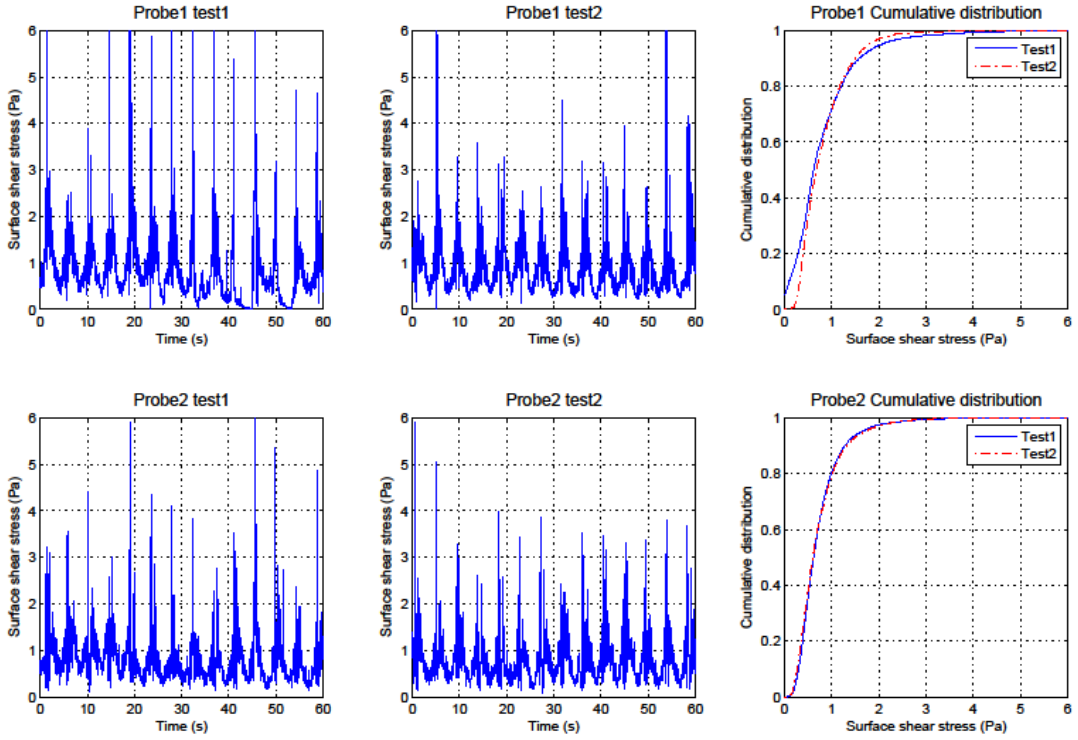

Figure A11-10. Result of PLWCC1.3.

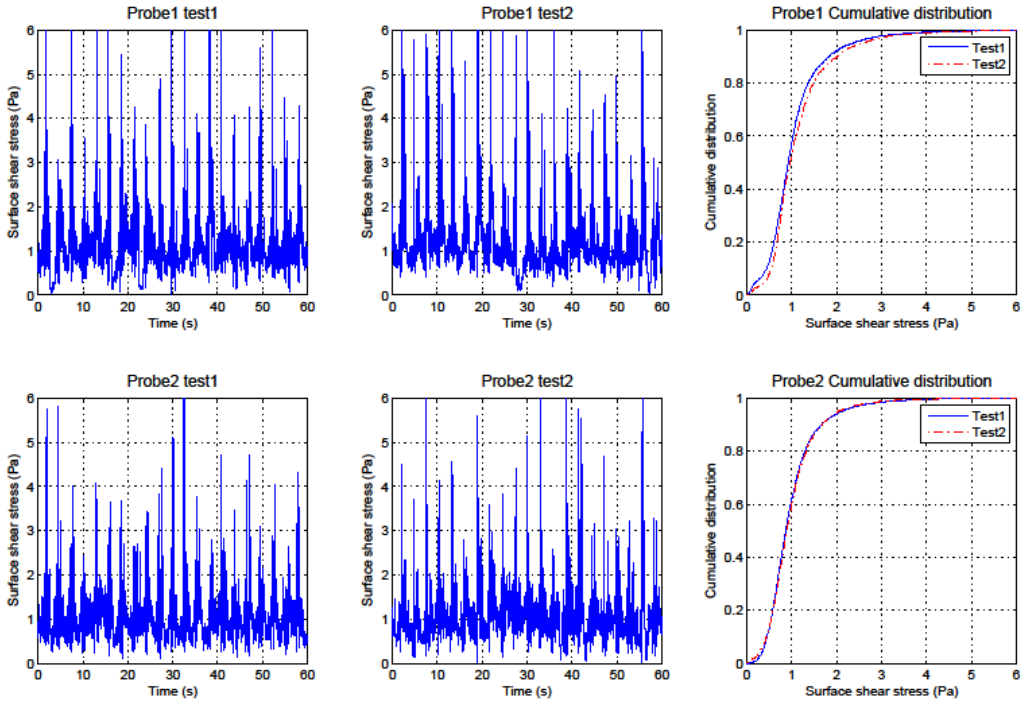

Figure A11-11. Result of PMWCC1.3.

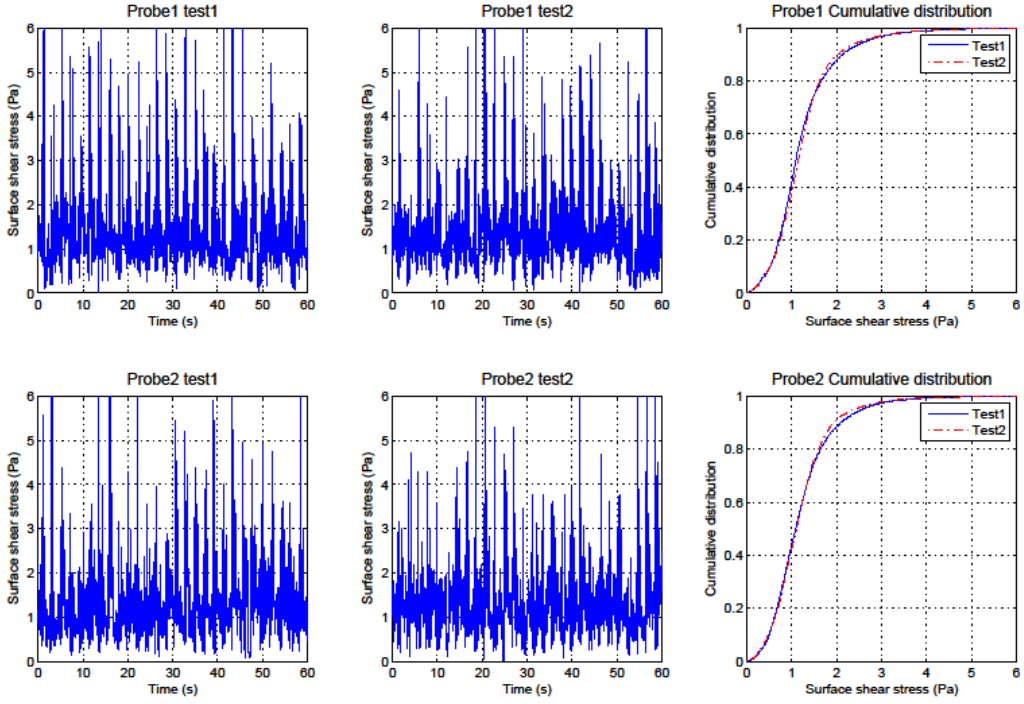

Figure A11-12. Result of PHWCC1.3.

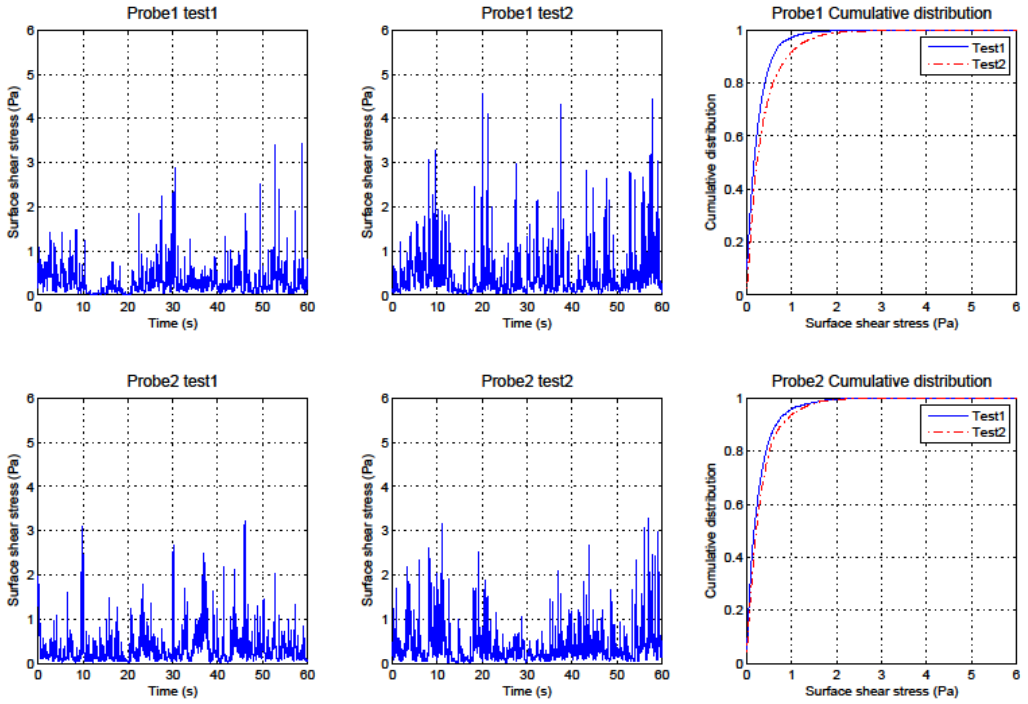

Figure A11- 13. Result of CLOSC1.3.

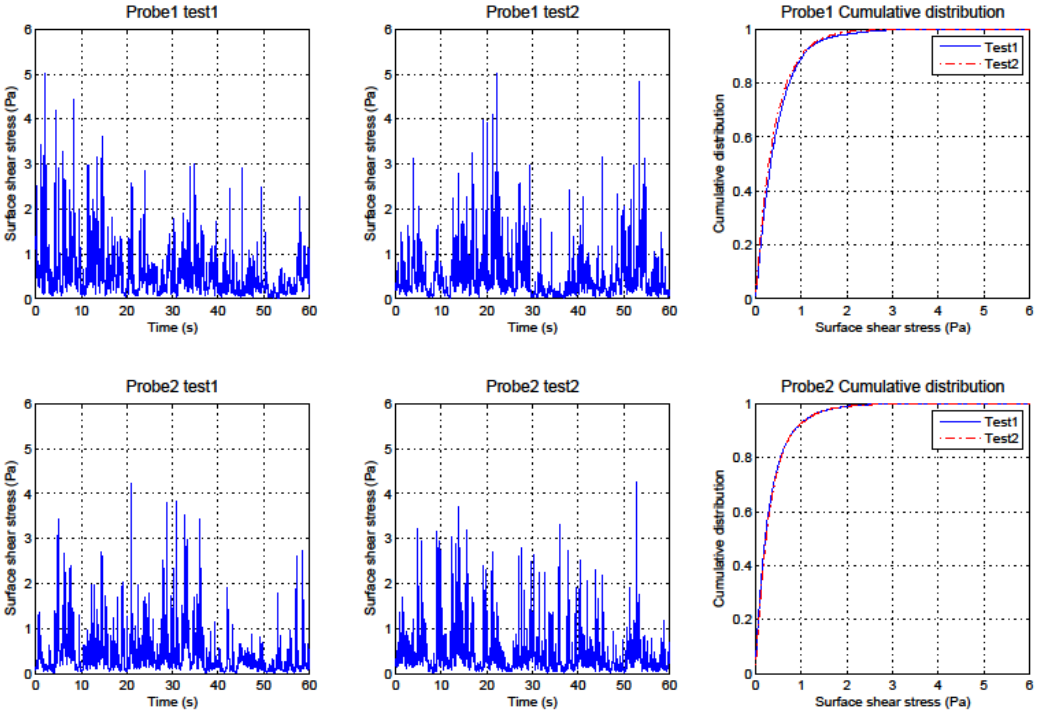

Figure A11-14. Result of CLOSC2.2.

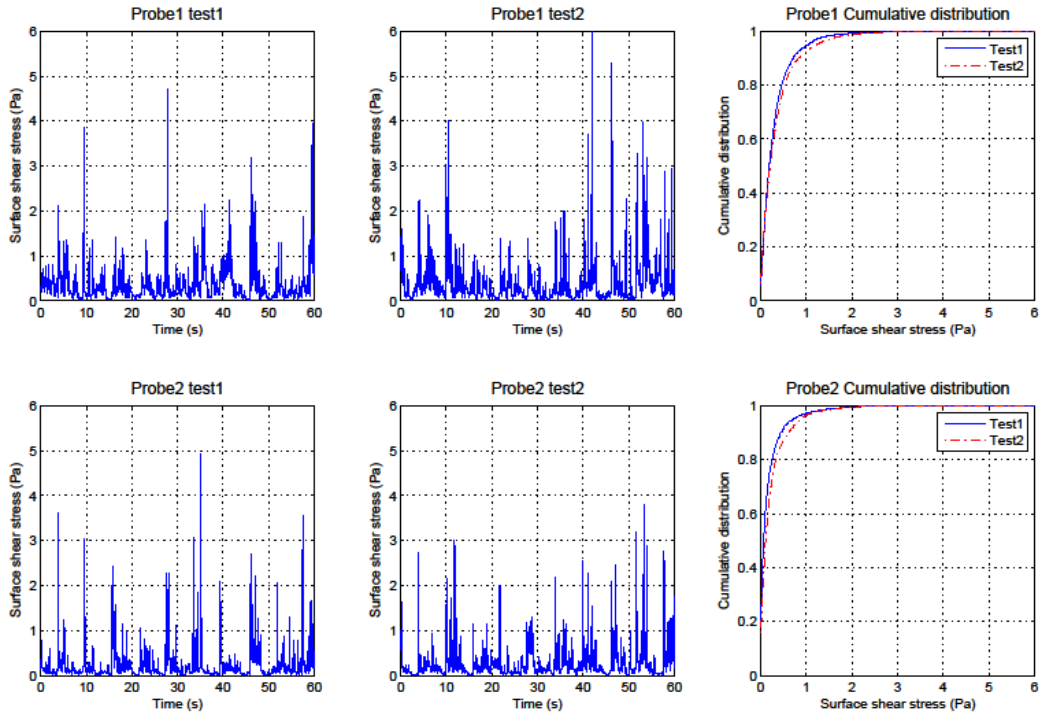

Figure A11-15. Result of CLOSF1.3.

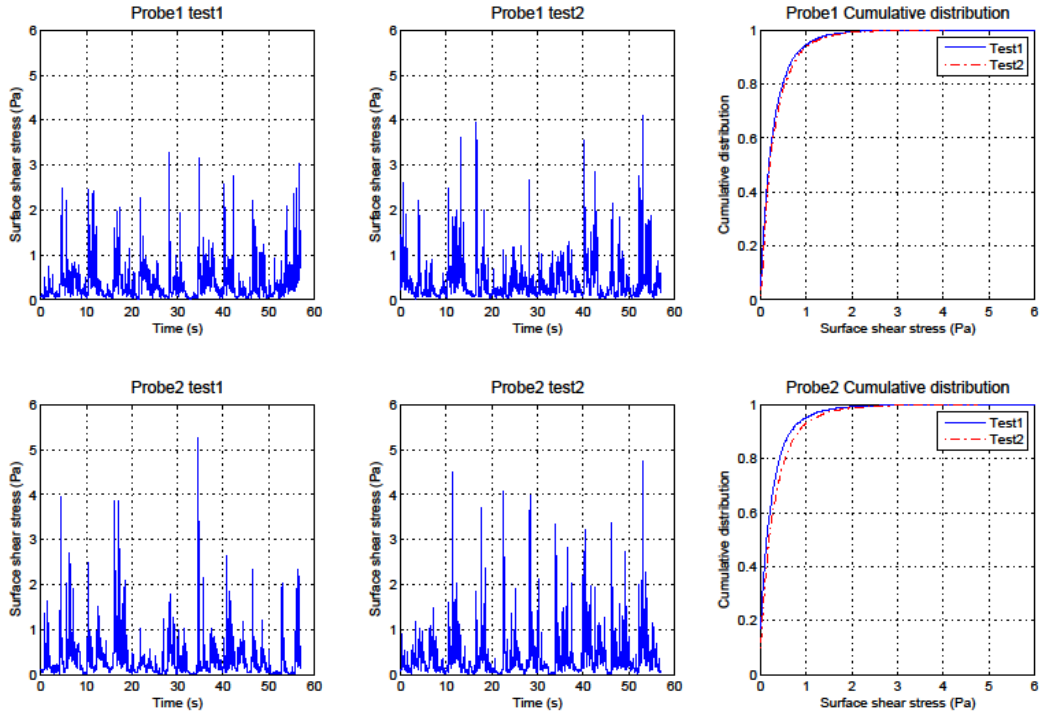

Figure A11-16. Result of CLOSF2.2.

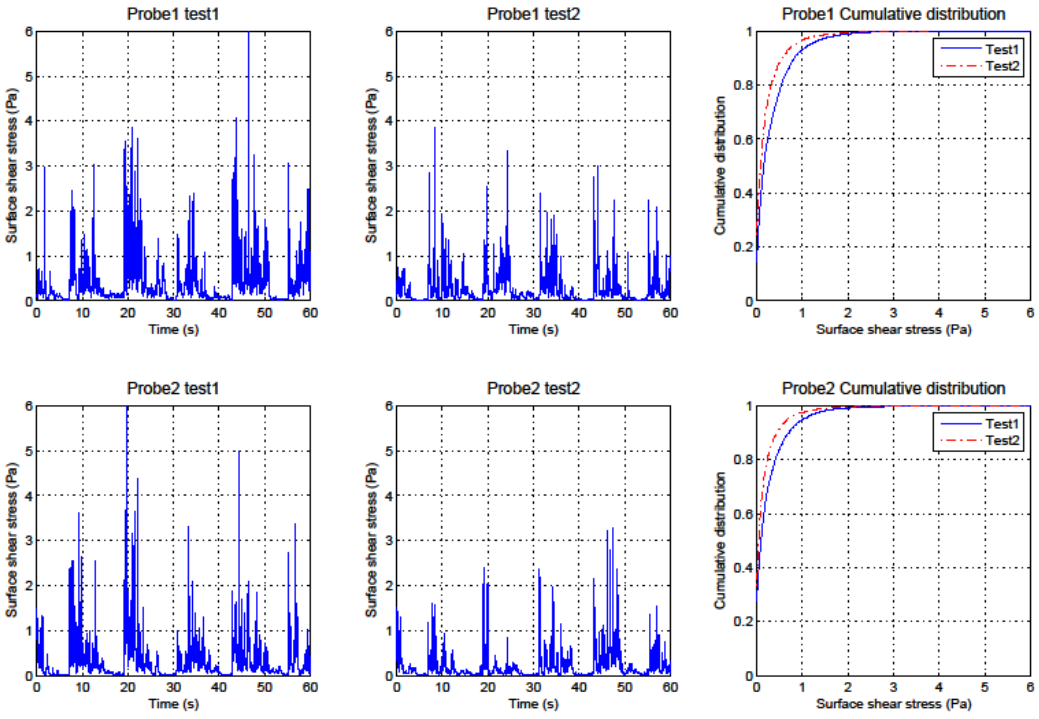

Figure A11-17. Result of CLOSS1.3.

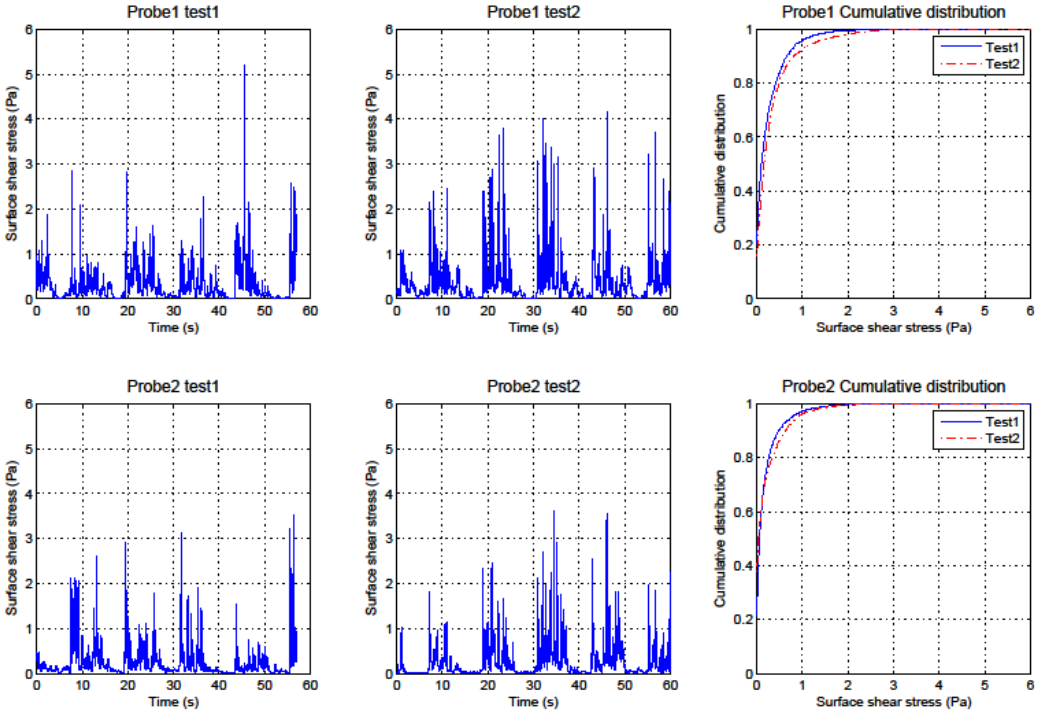

Figure A11-18. Result of CLOSS2.2.

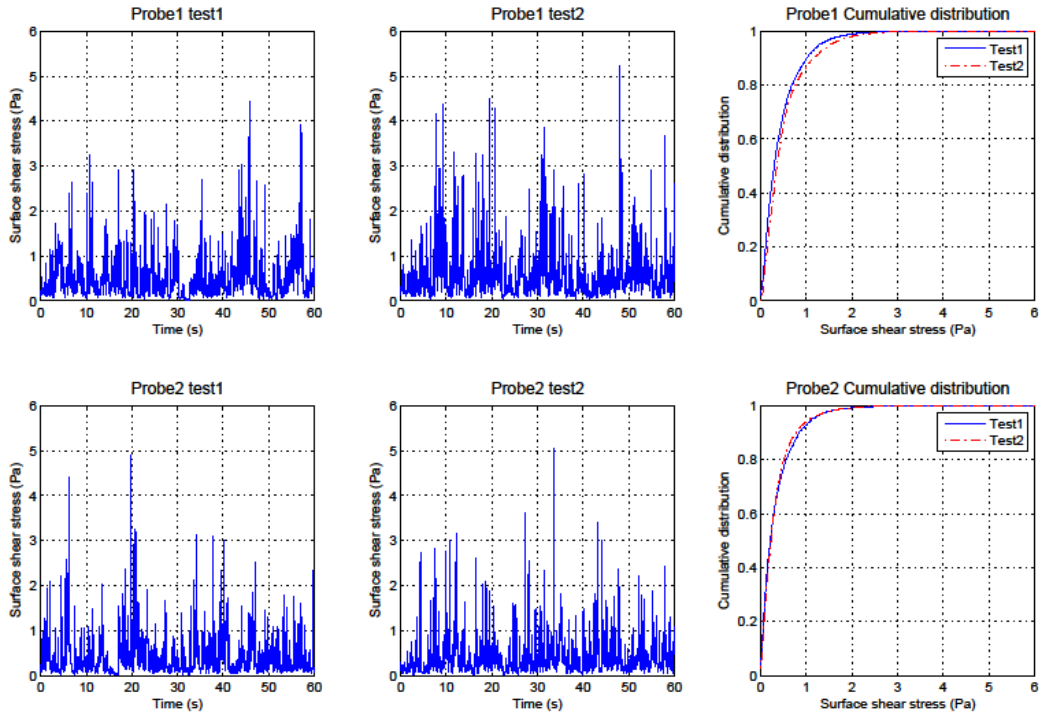

Figure A11-19. Result of CMOSC1.3.

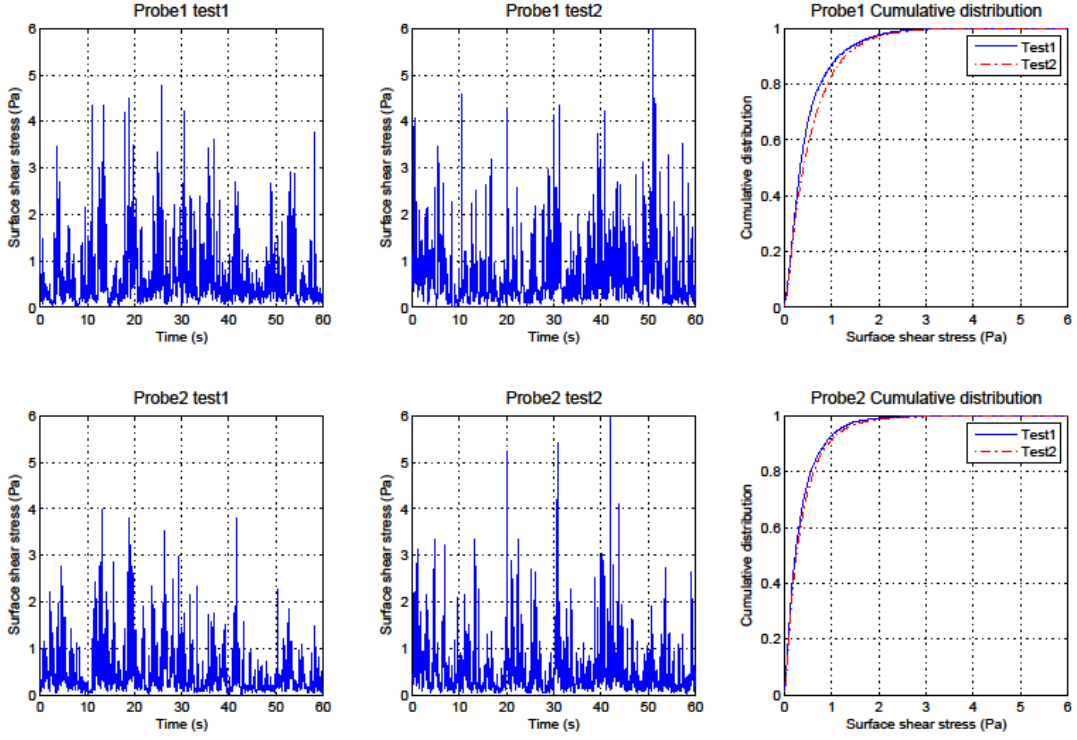

Figure A11-20. Result of CMOSC2.2.

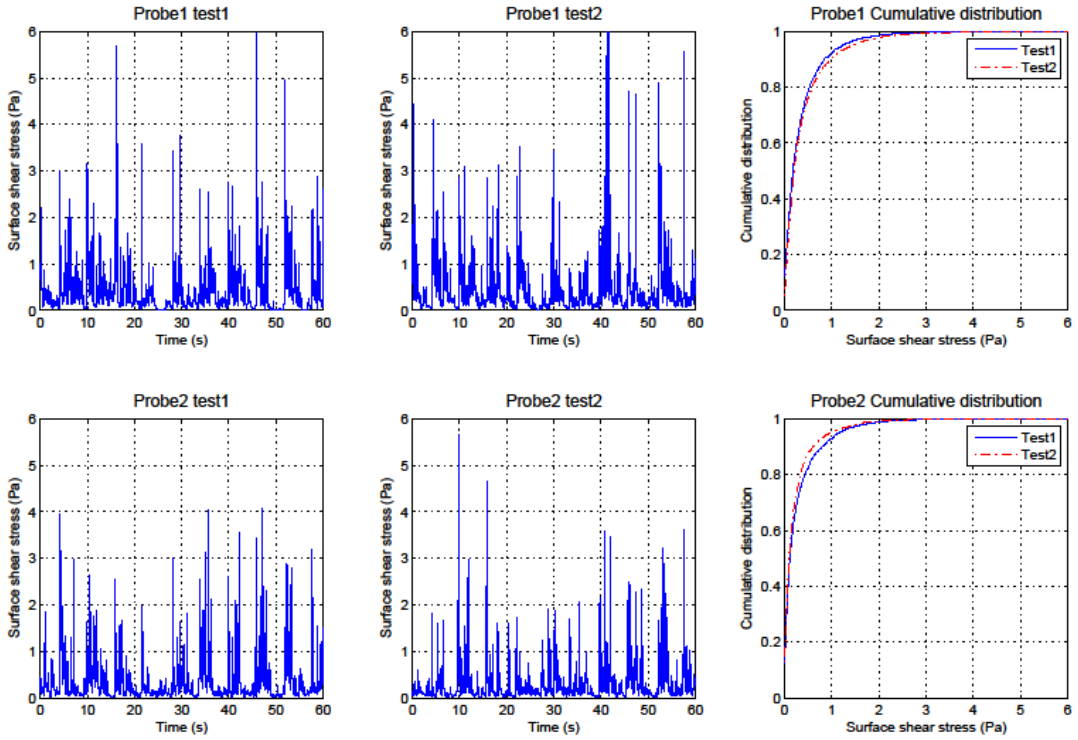

Figure A11-21. Result of CMOSF1.3.

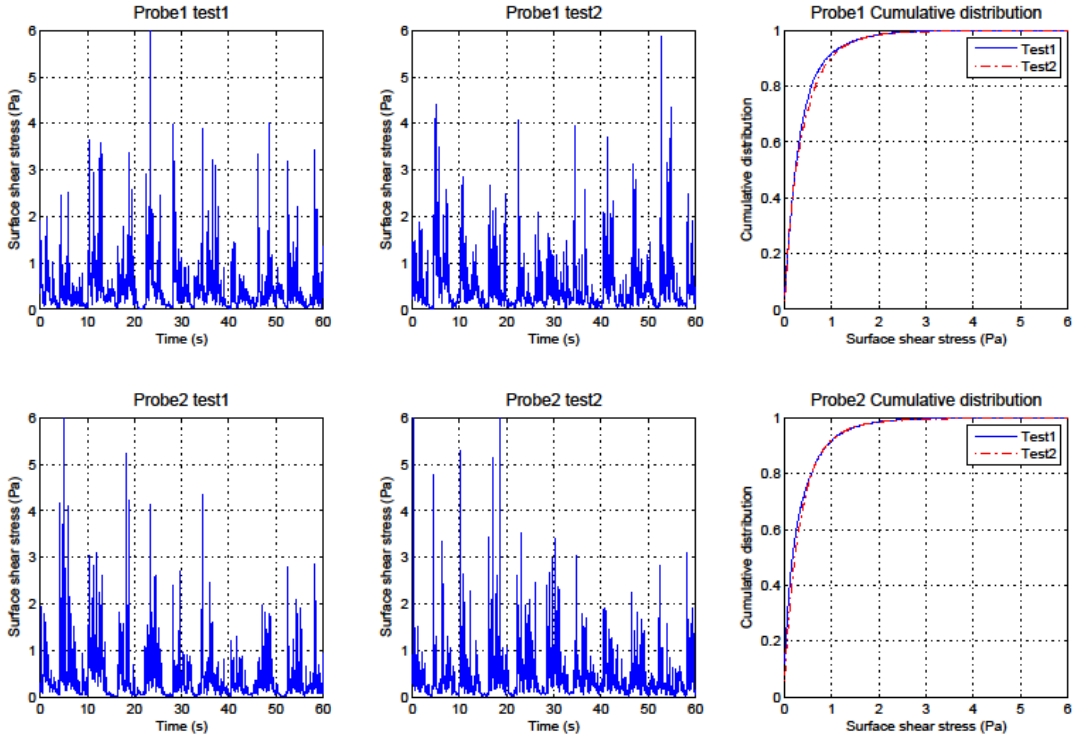

Figure A11-22. Result of CMOSF2.2.

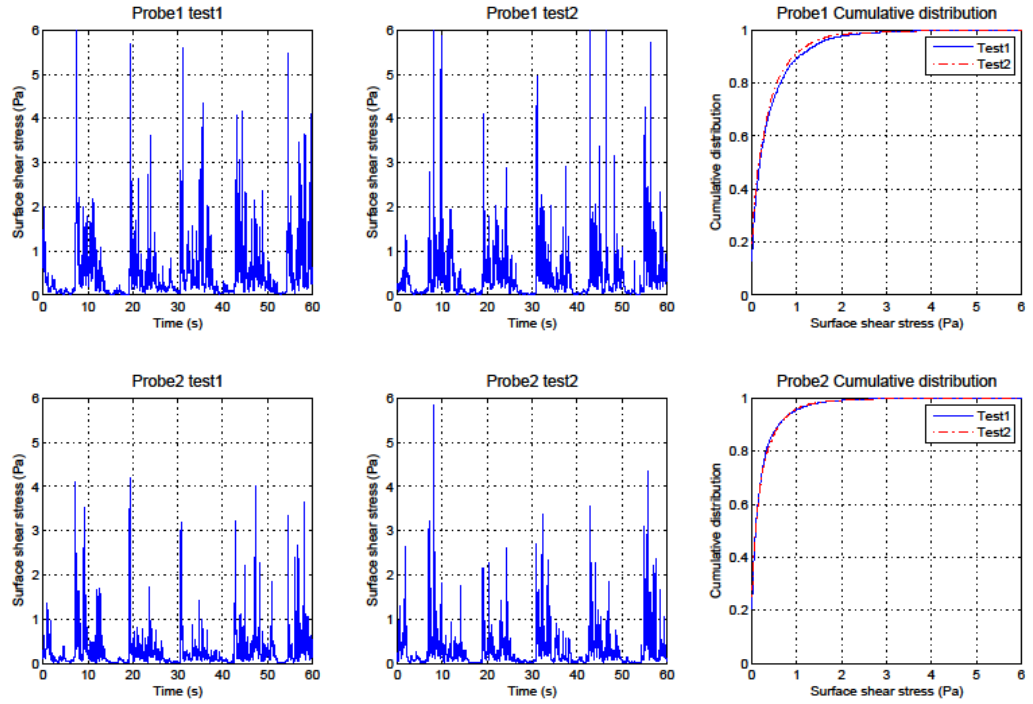

Figure A11-23. Result of CMOSS1.3.

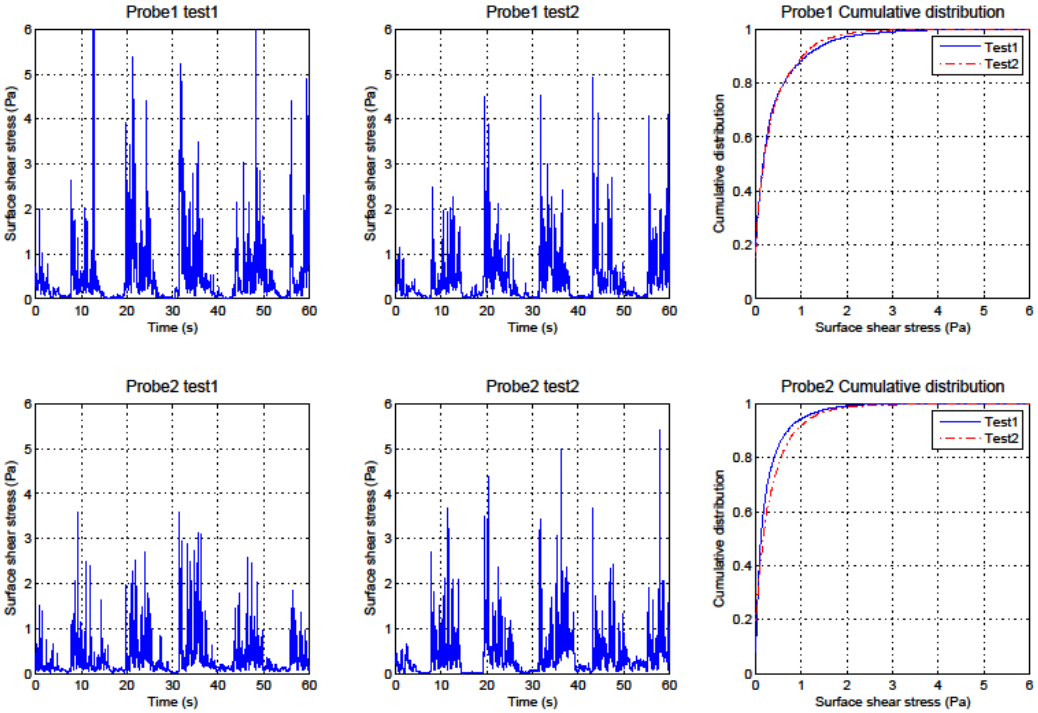

Figure A11-24. Result of CMOSS2.2.

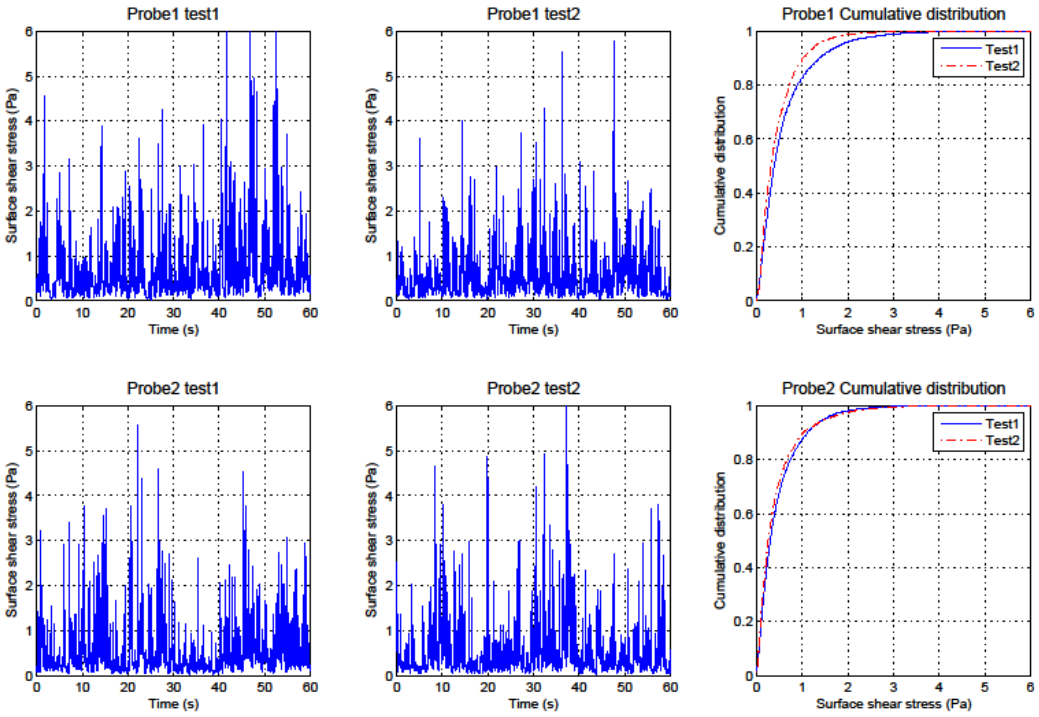

Figure A11-25. Result of CHOSC1.3.

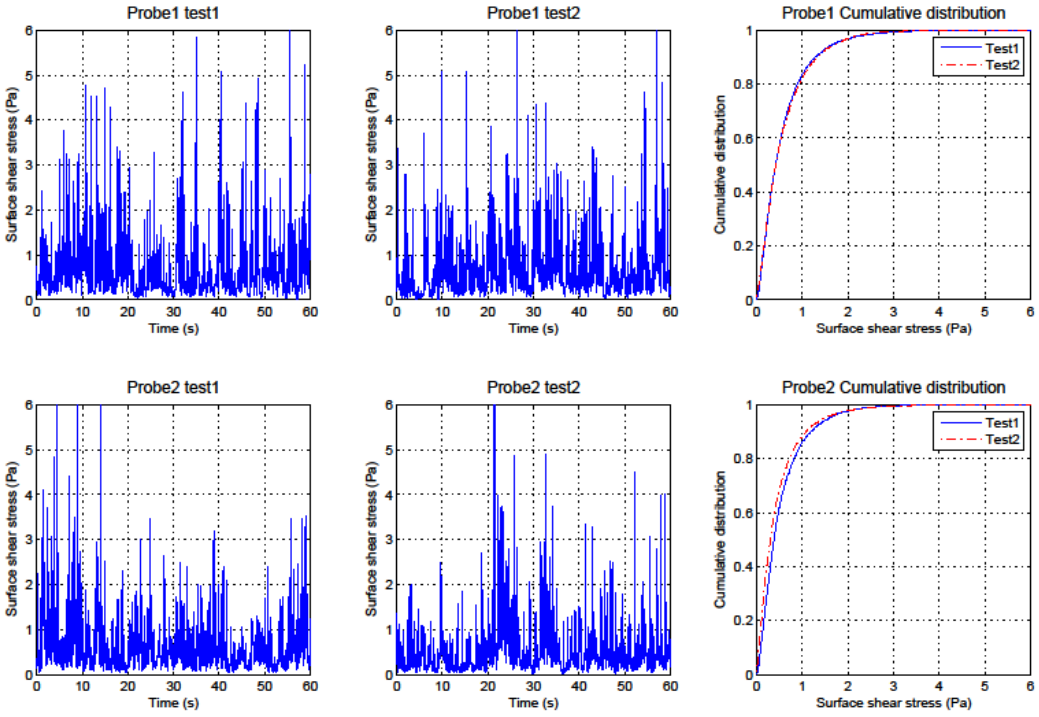

Figure A11-26. Result of CHOSC2.2.

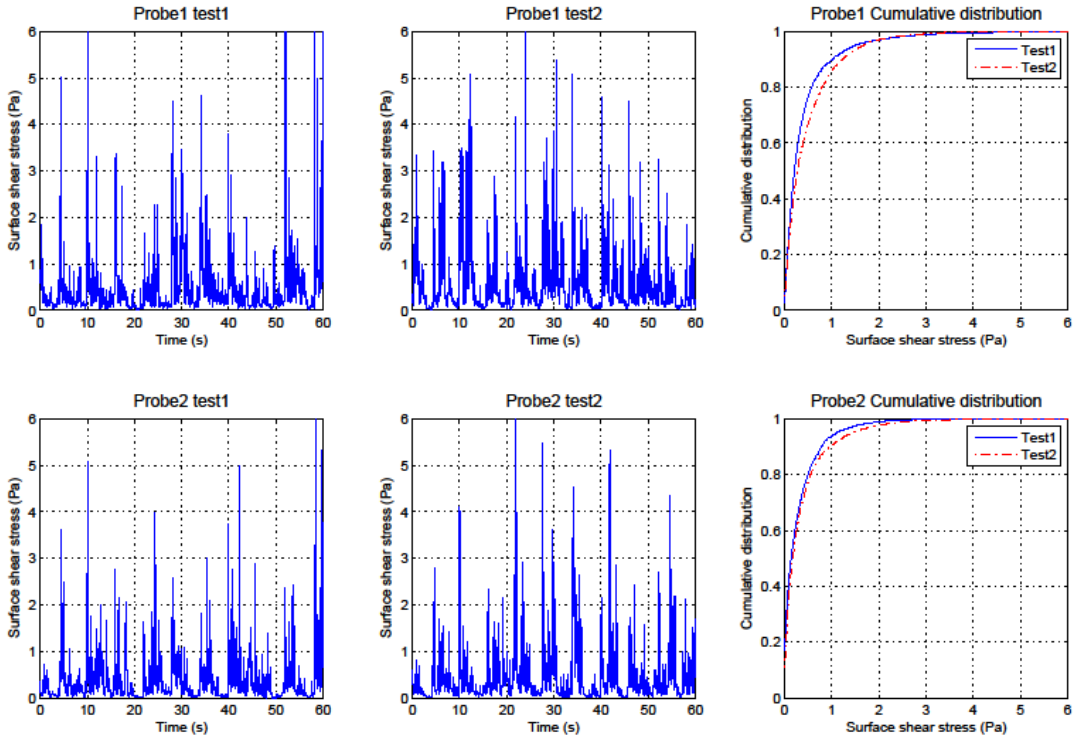

Figure A11-27. Result of CHOSF1.3.

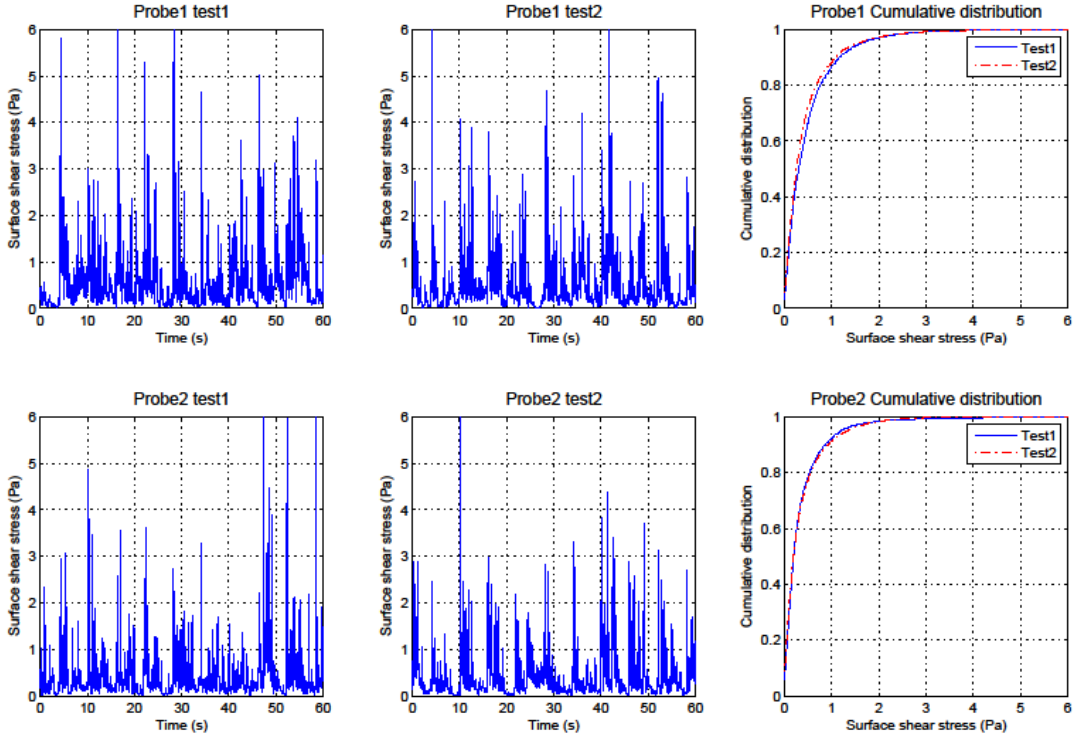

Figure A11-28. Result of CHOSF2.2.

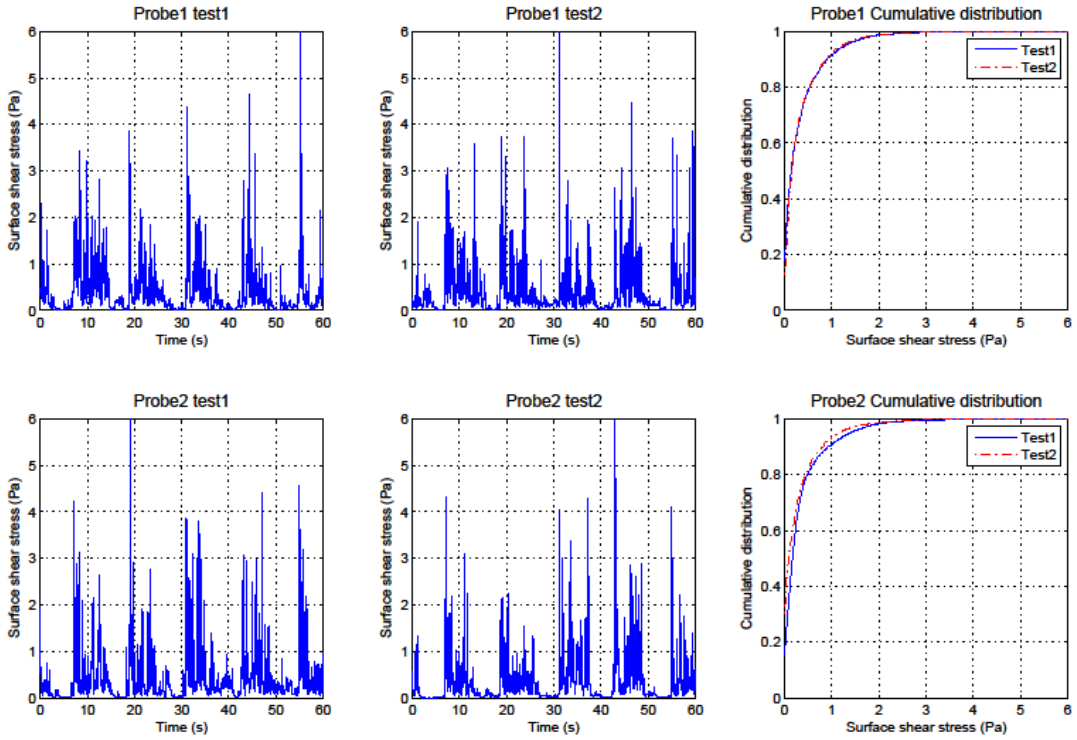

Figure A11-29. Result of CHOSS1.3.

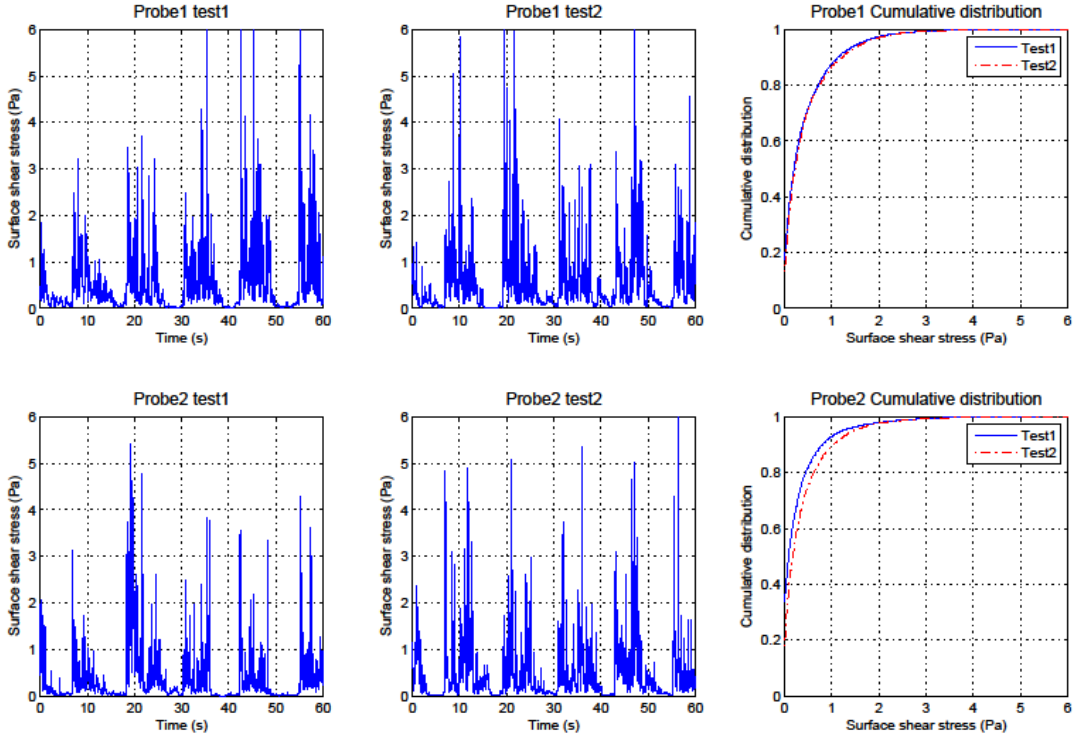

Figure A11-30. Result of CHOSS2.2.

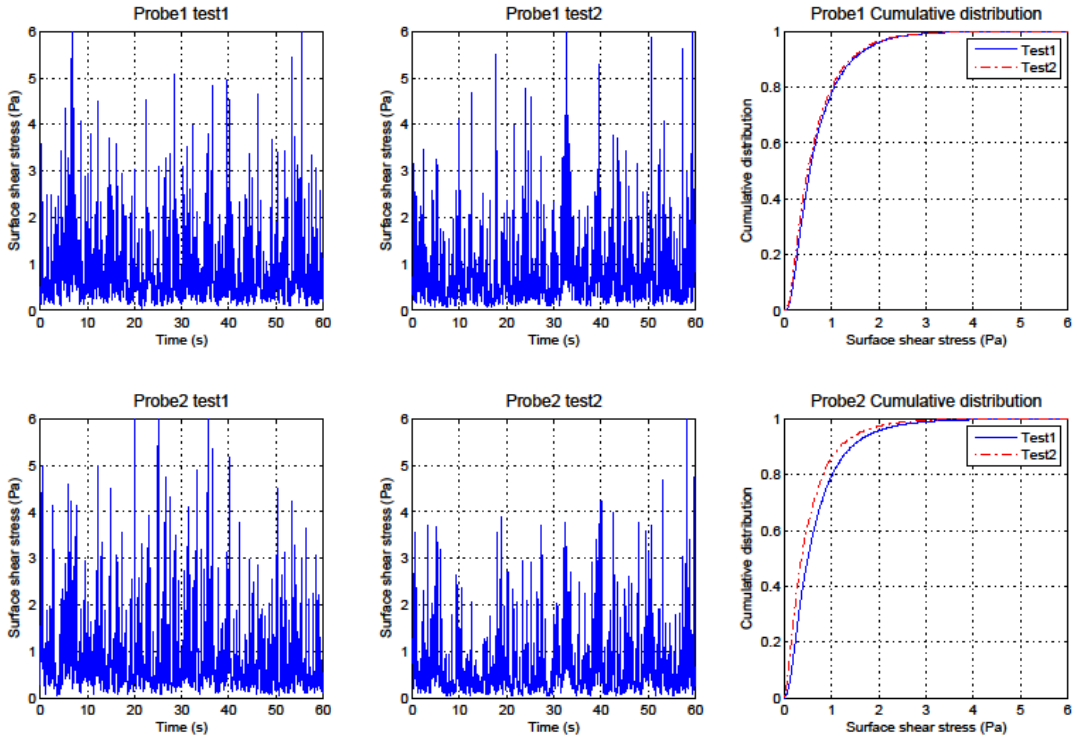

Figure A11-31. Result of CLWSC1.3.

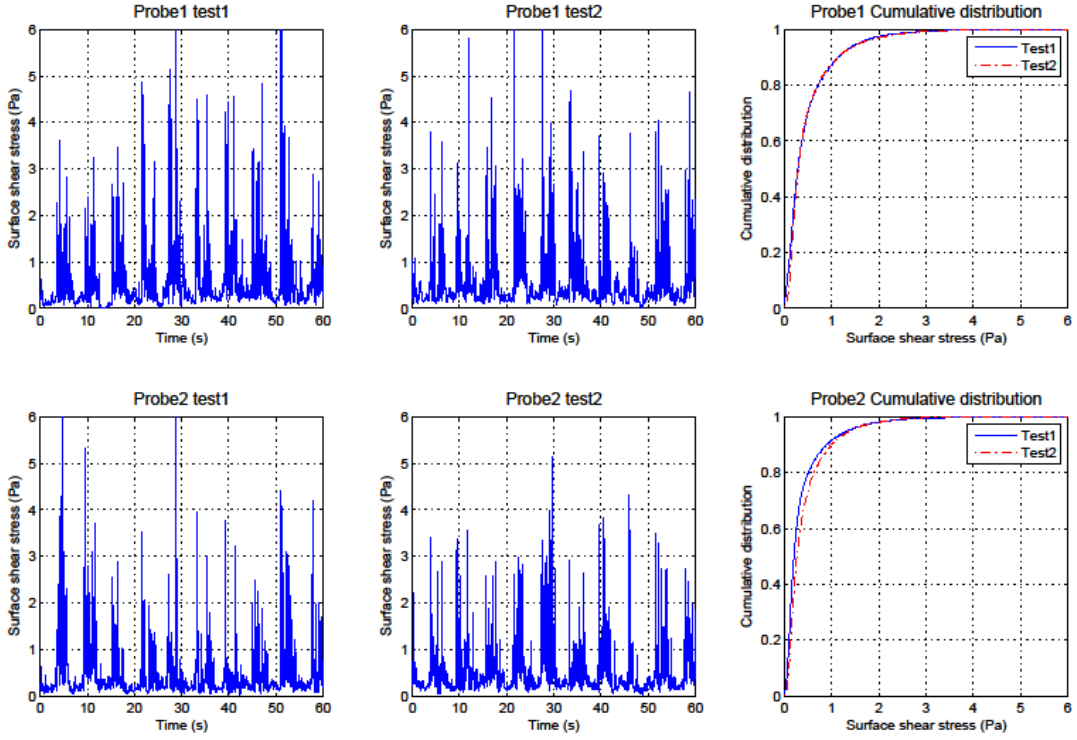

Figure A11-32. Result of CLWSF1.3.

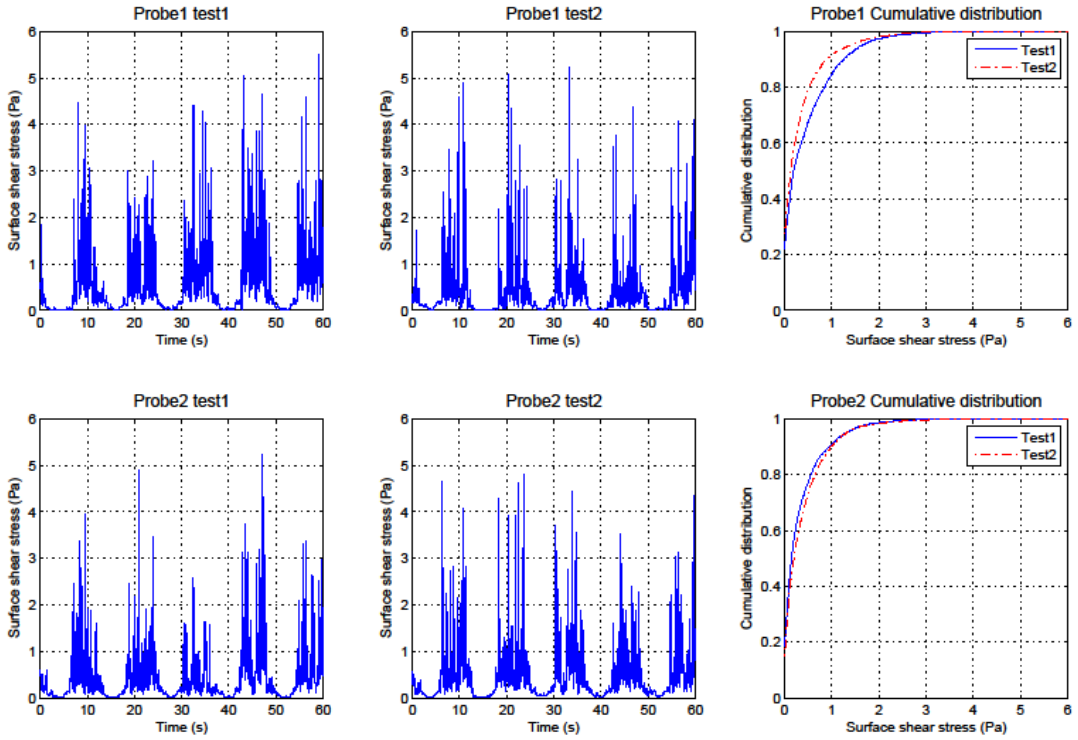

Figure A11-33. Result of CLWSS1.3.

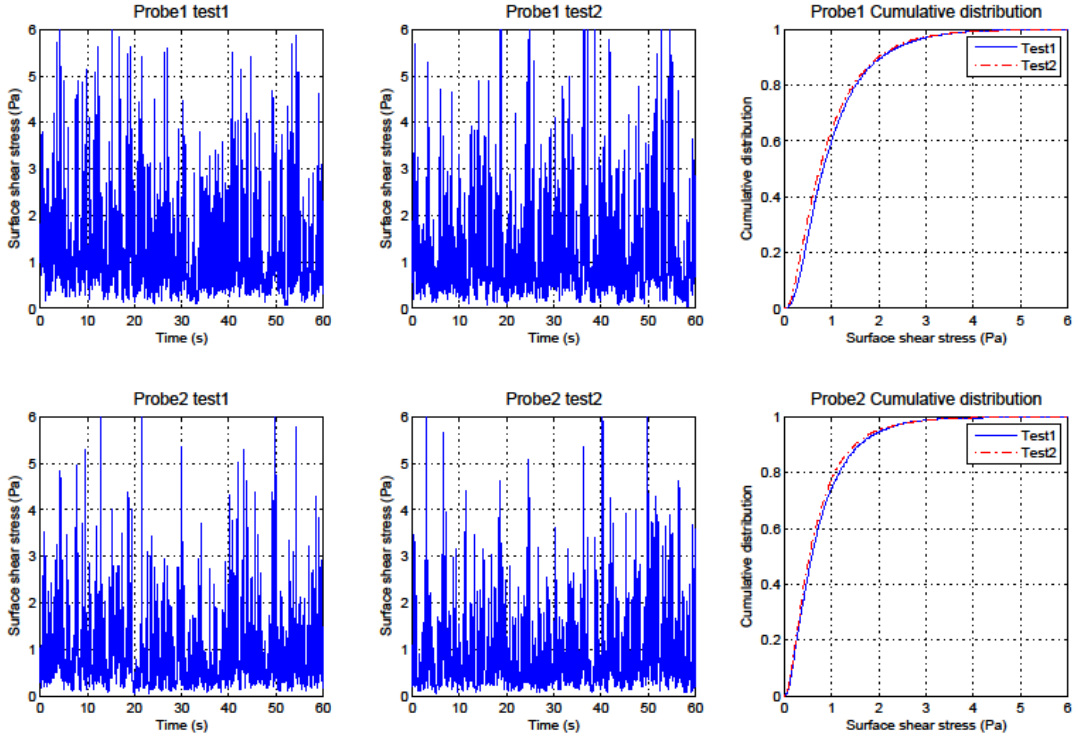

Figure A11-34. Result of CMWSC1.3.

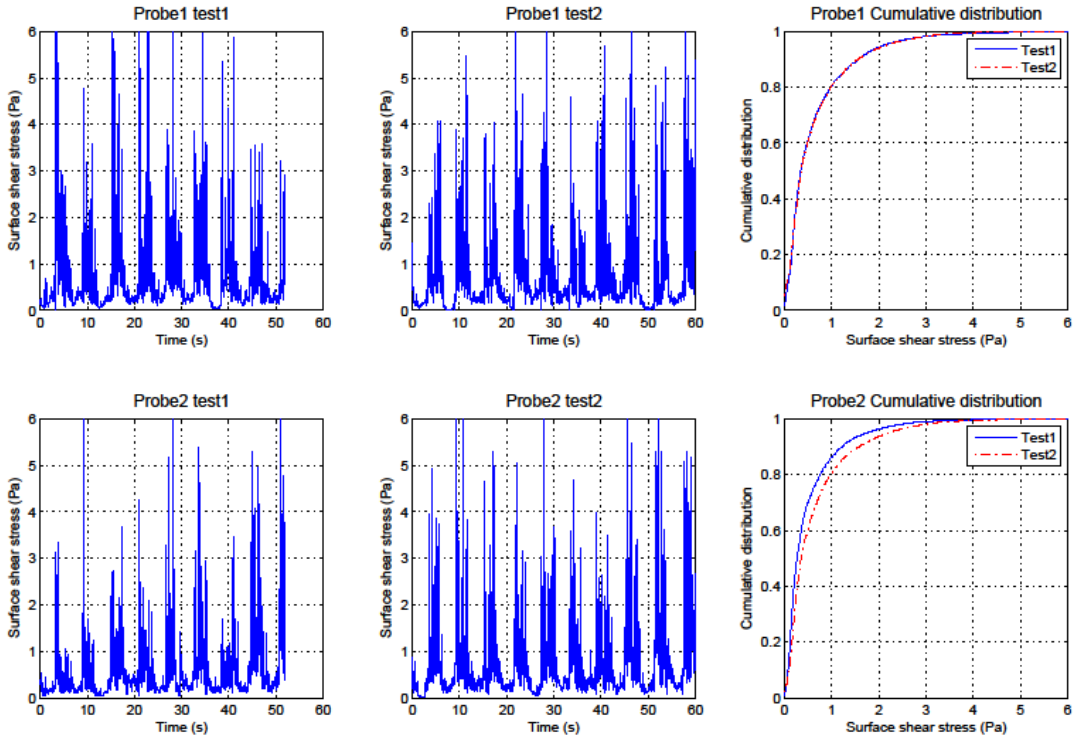

Figure A11-35. Result of CMWSF1.3.

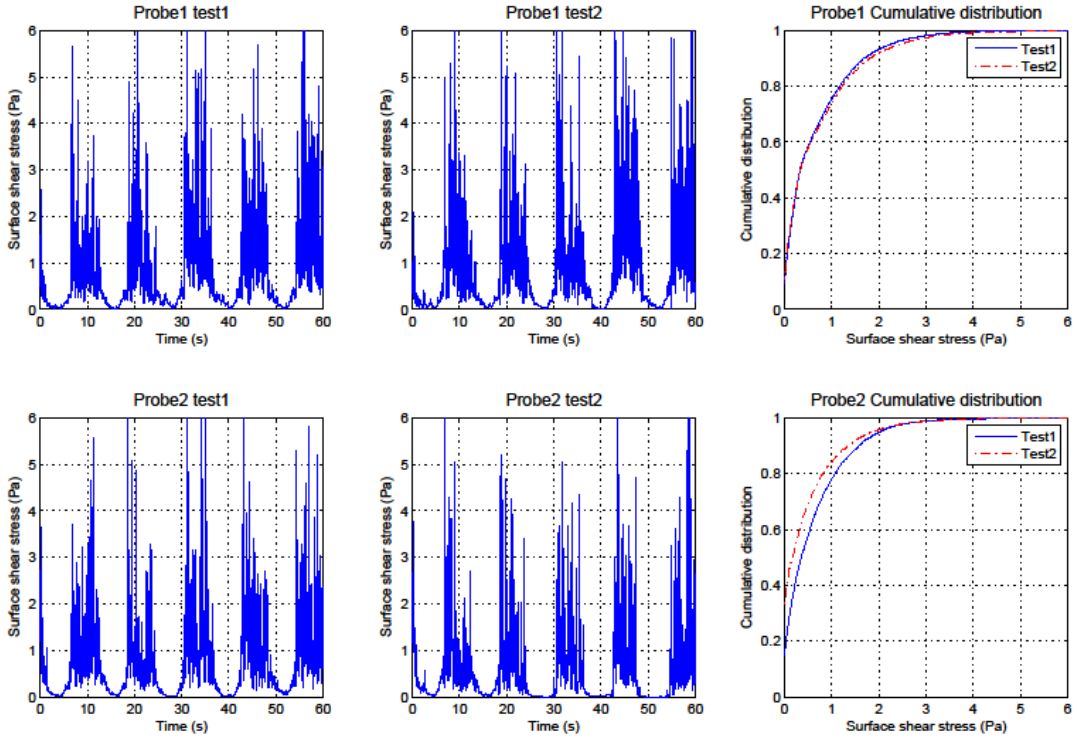

Figure A11-36. Result of CMWSS1.3.

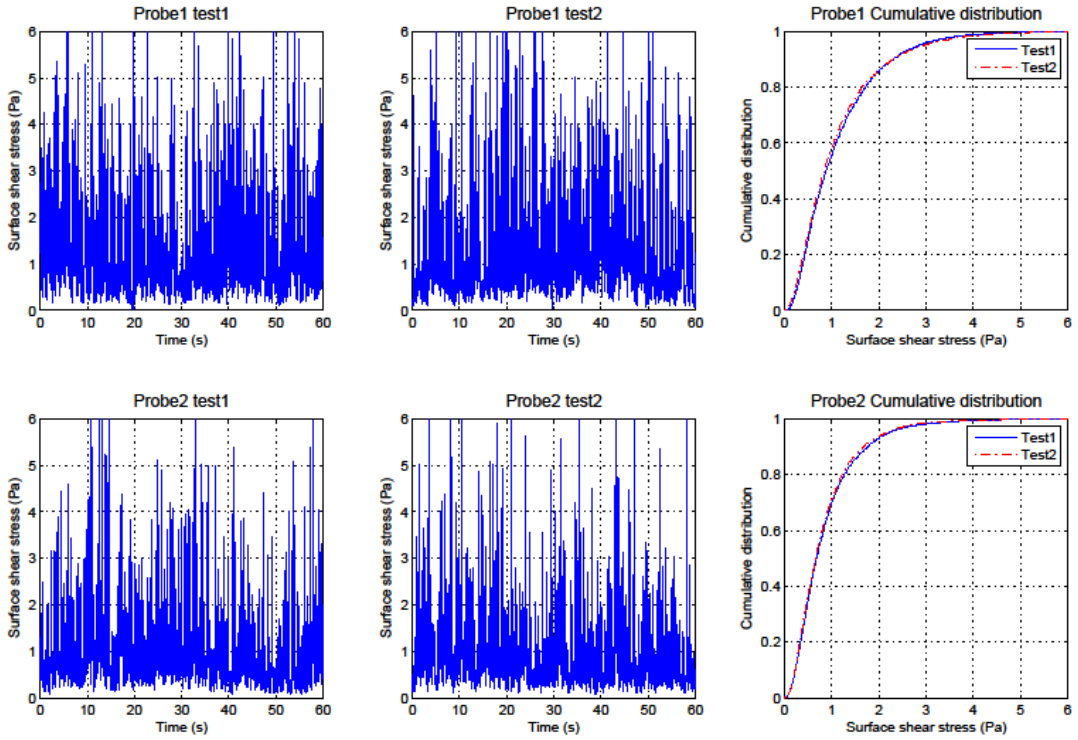

Figure A11-37. Result of CHWSC1.3.

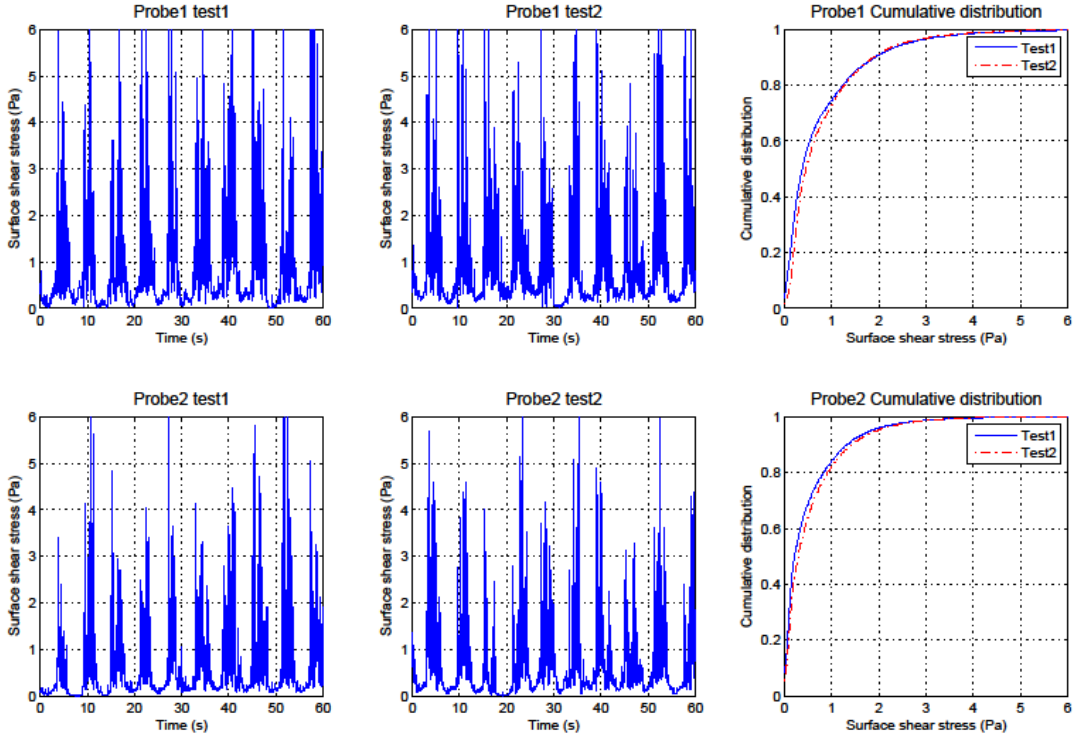

Figure A11-38. Result of CHWSF1.3.

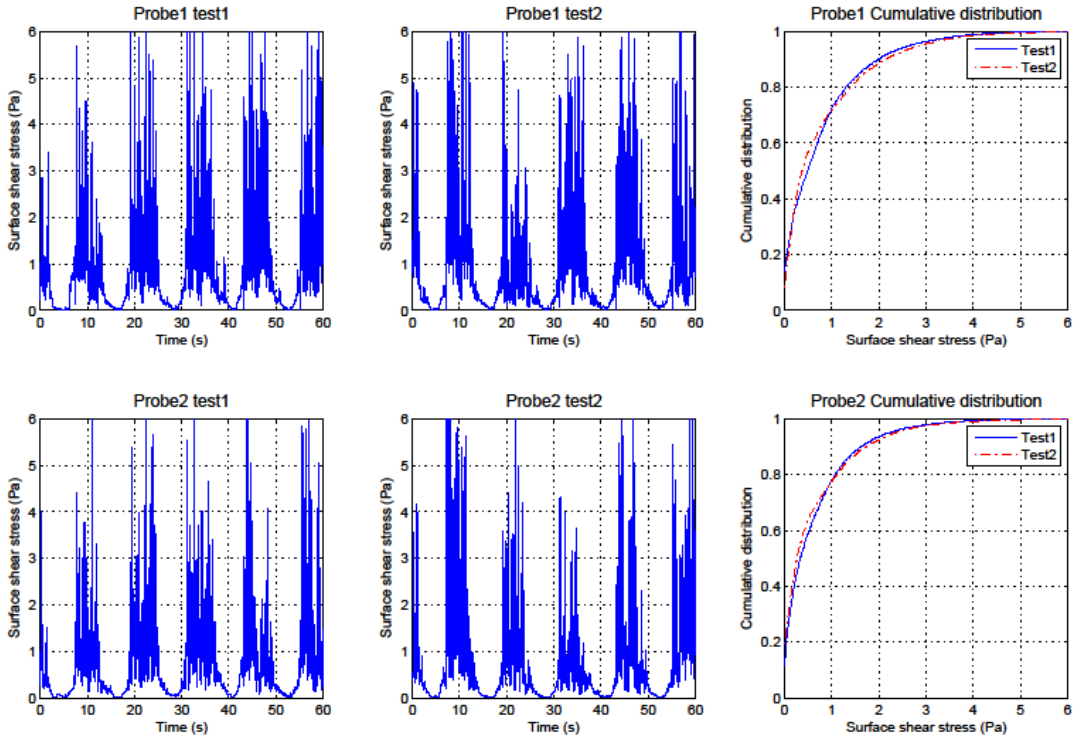

Figure A11-39. Result of CHWSS1.3.

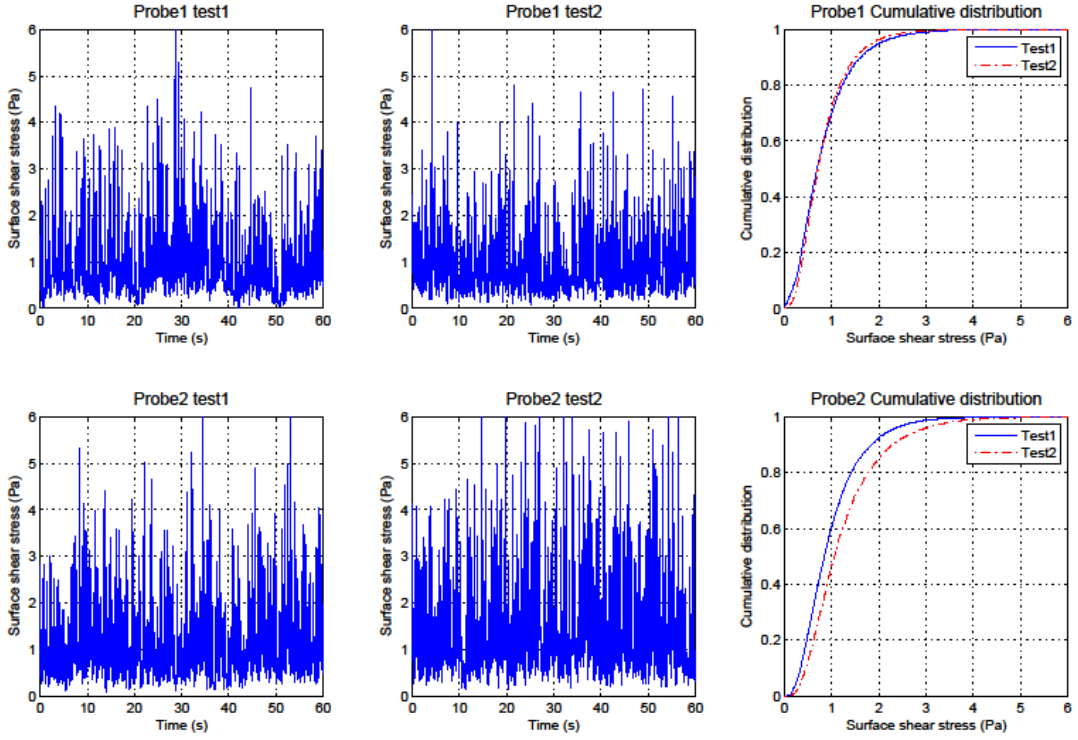

Figure A11-40. Result of CLWCC1.3.

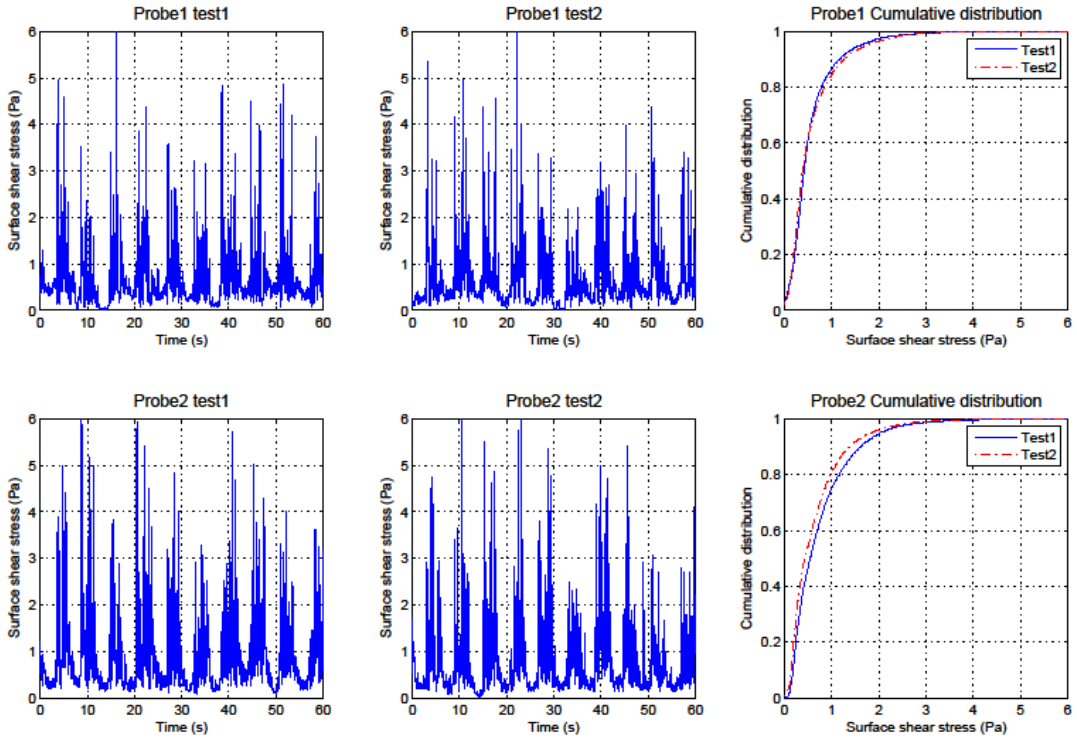

Figure A11-41. Result of CLWCF1.3.

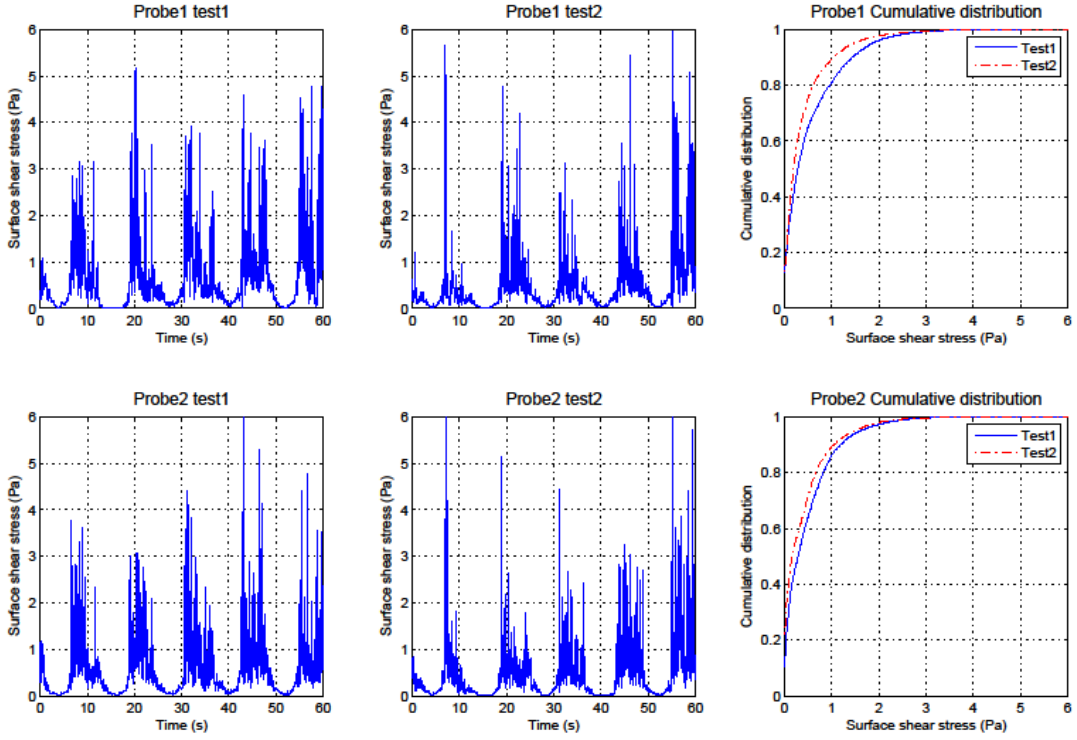

Figure A11-42. Result of CLWCS1.3.

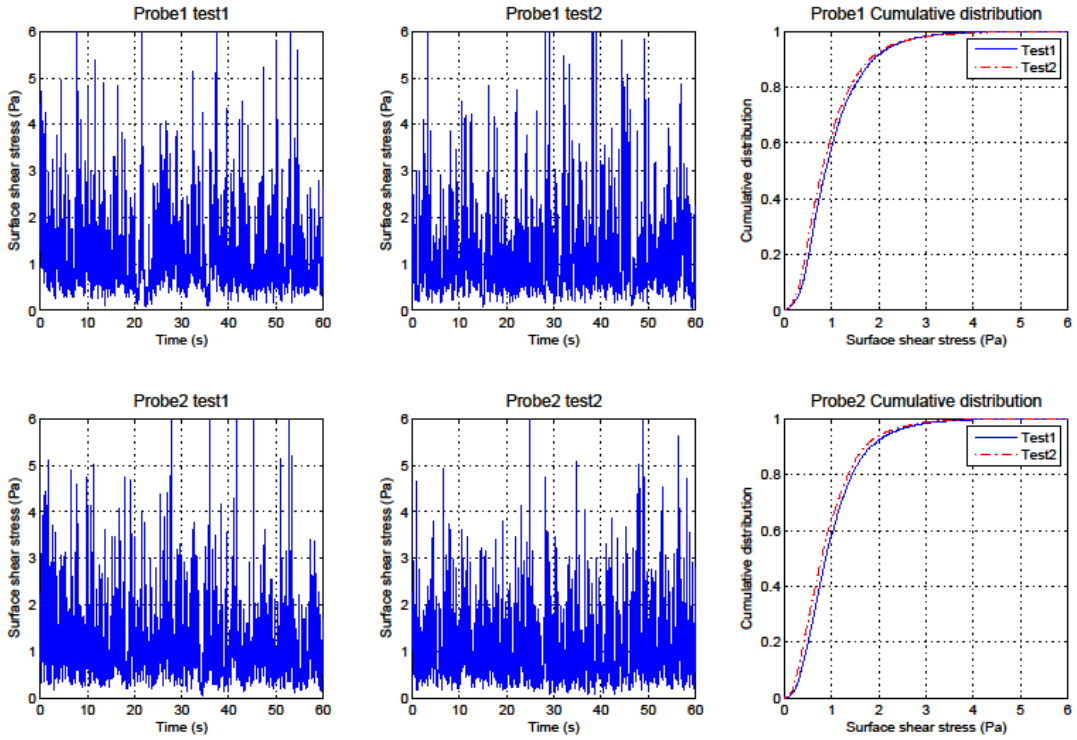

Figure A11-43. Result of CMWCC1.3.

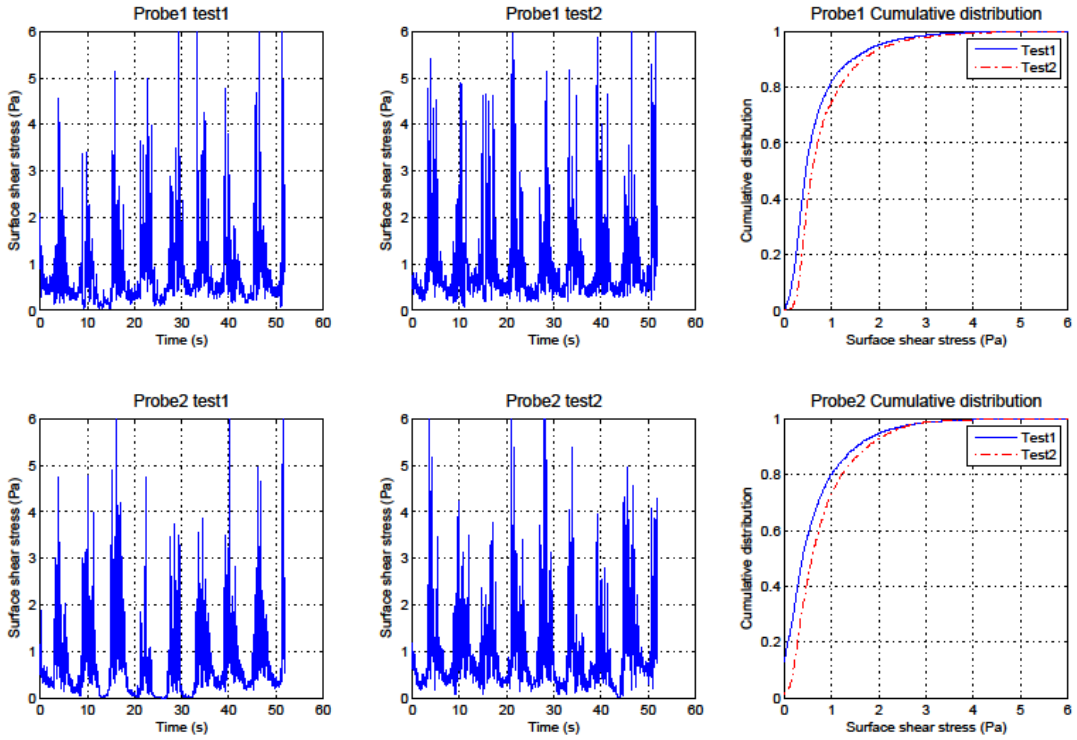

Figure A11-44. Result of CMWCF1.3.

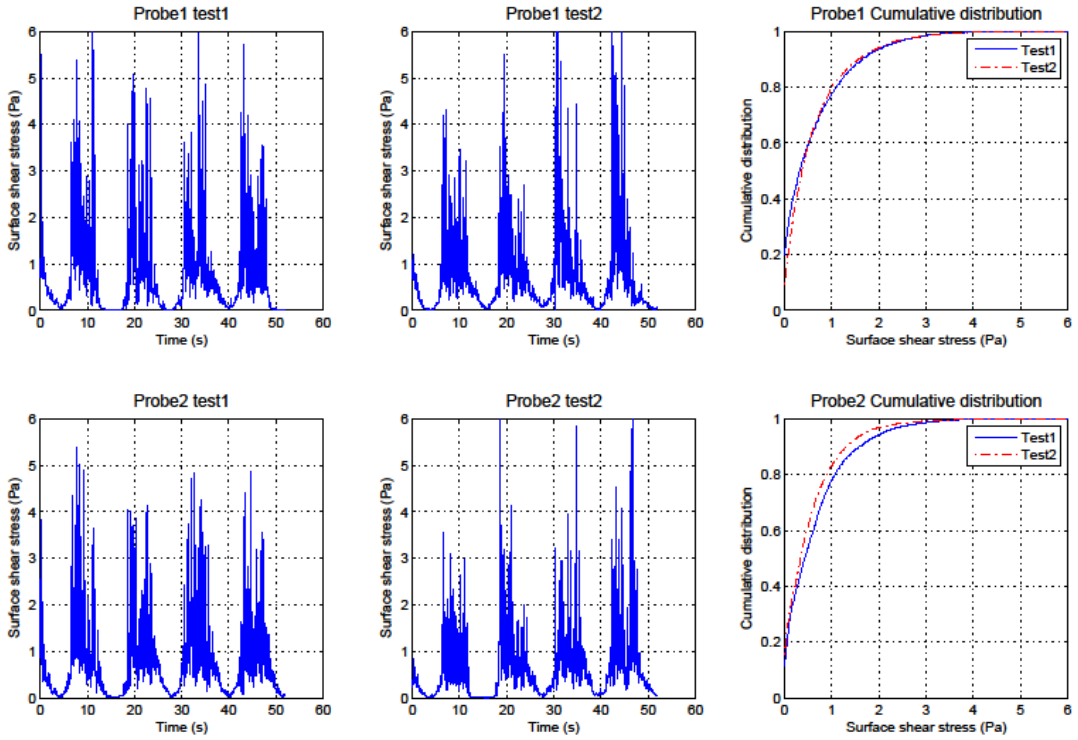

Figure A11-45. Result of CMWCS1.3.

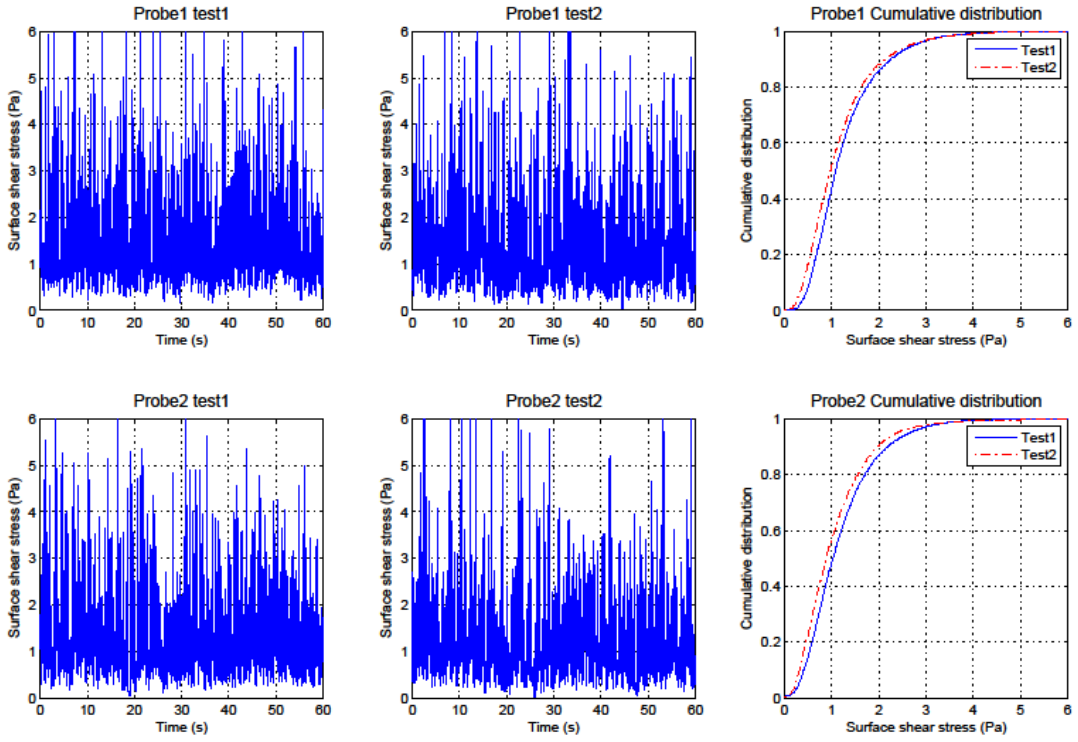

Figure A11-46. Result of CHWCC1.3.

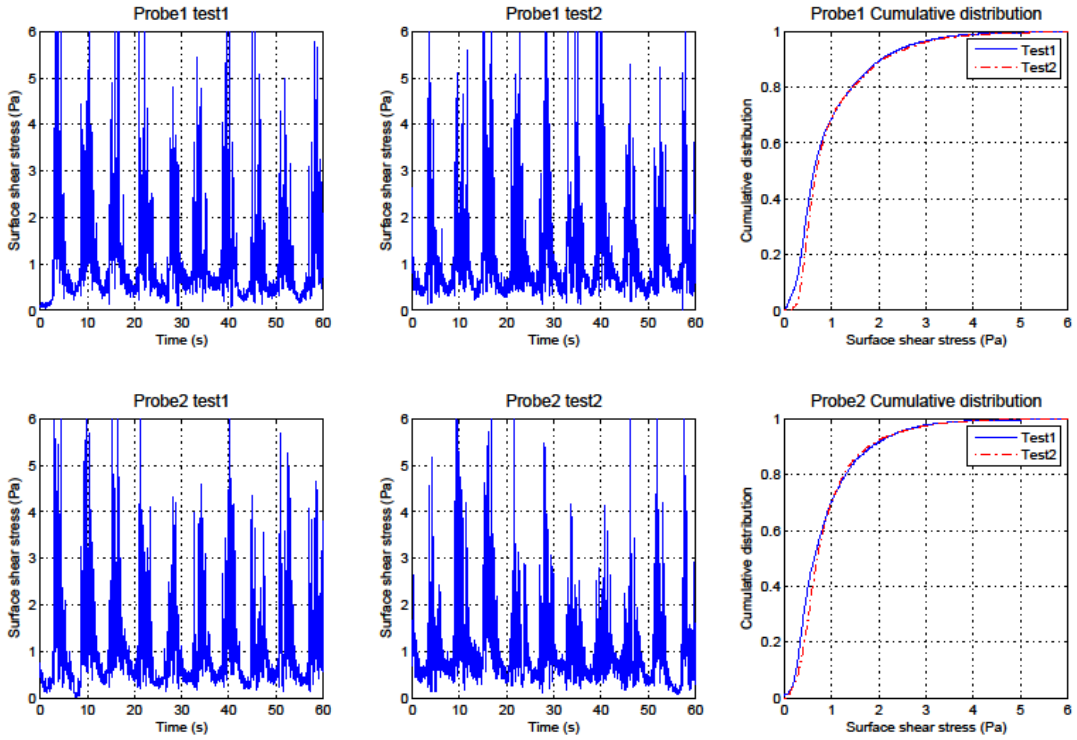

Figure A11-47. Result of CHWCF1.3.

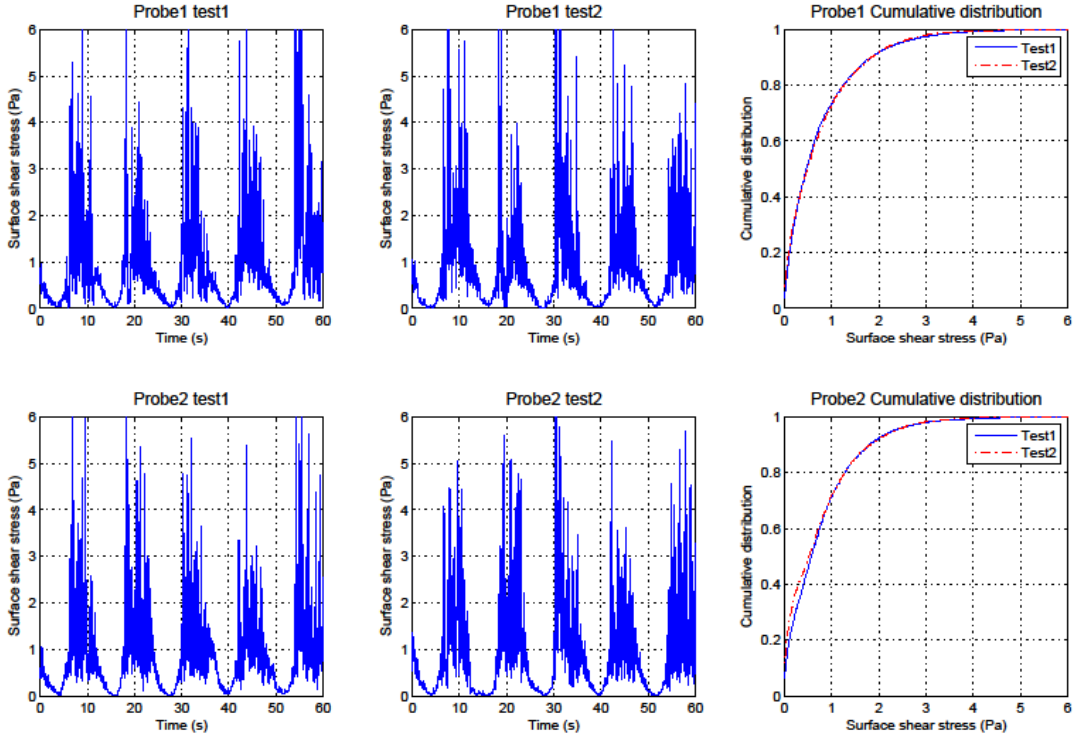

Figure A11-48. Result of CHWCS1.3.

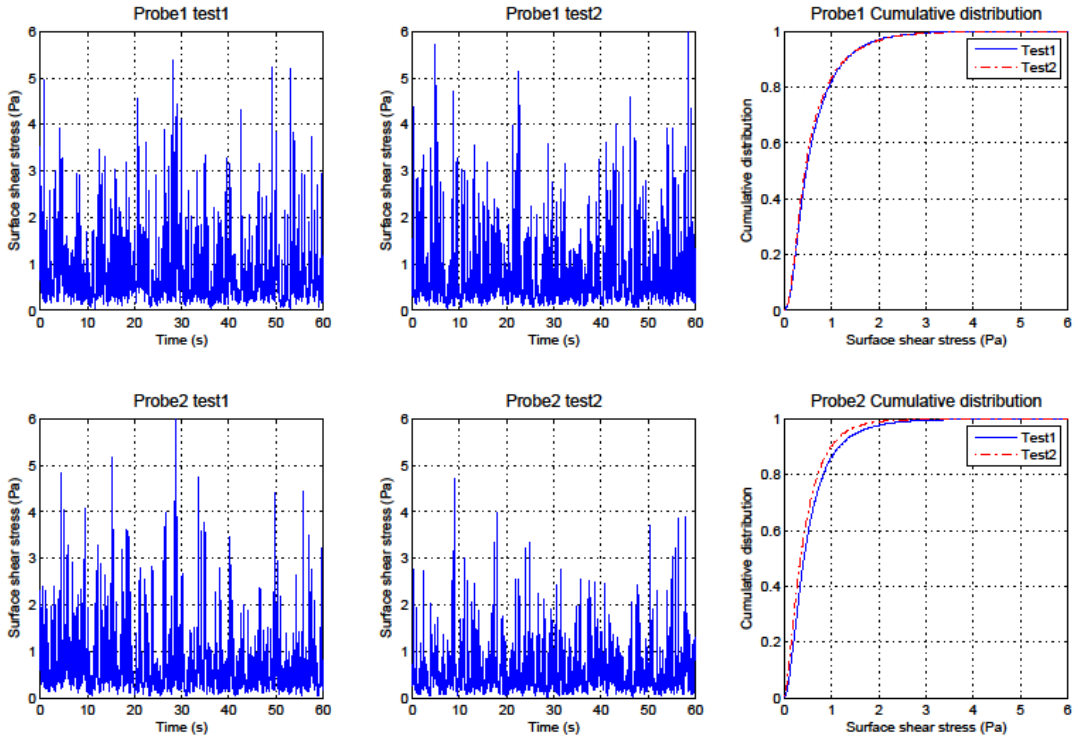

Figure A11-49. Result of FLWSC1.3.

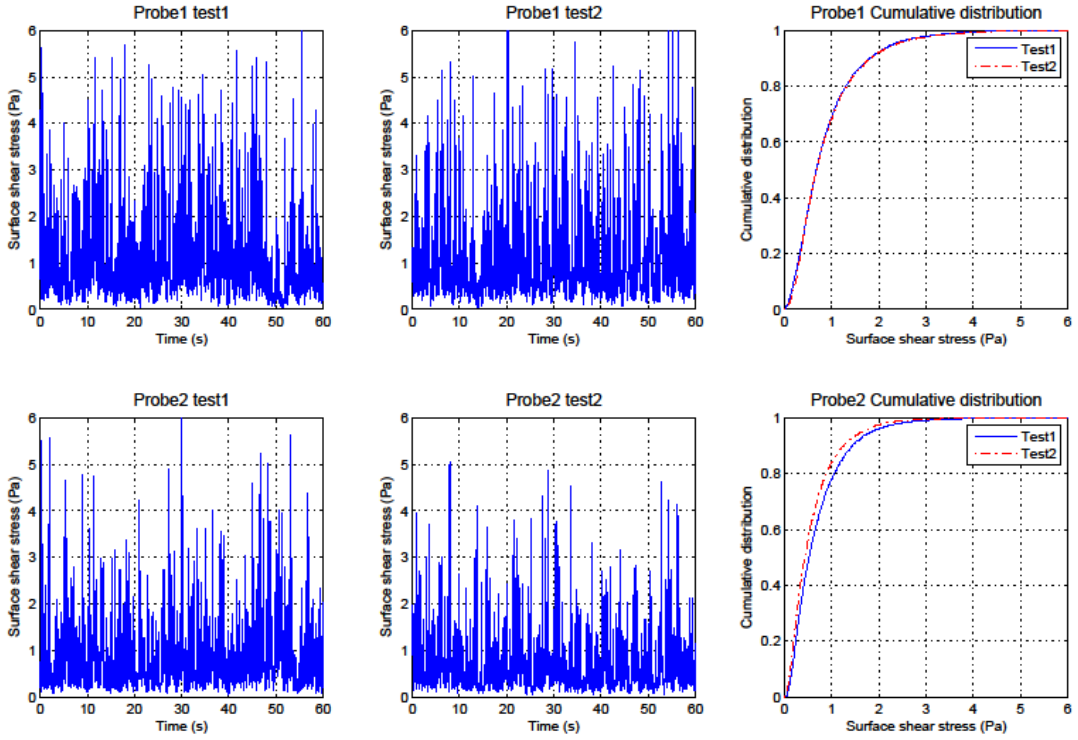

Figure A11-50. Result of FMWSC1.3.

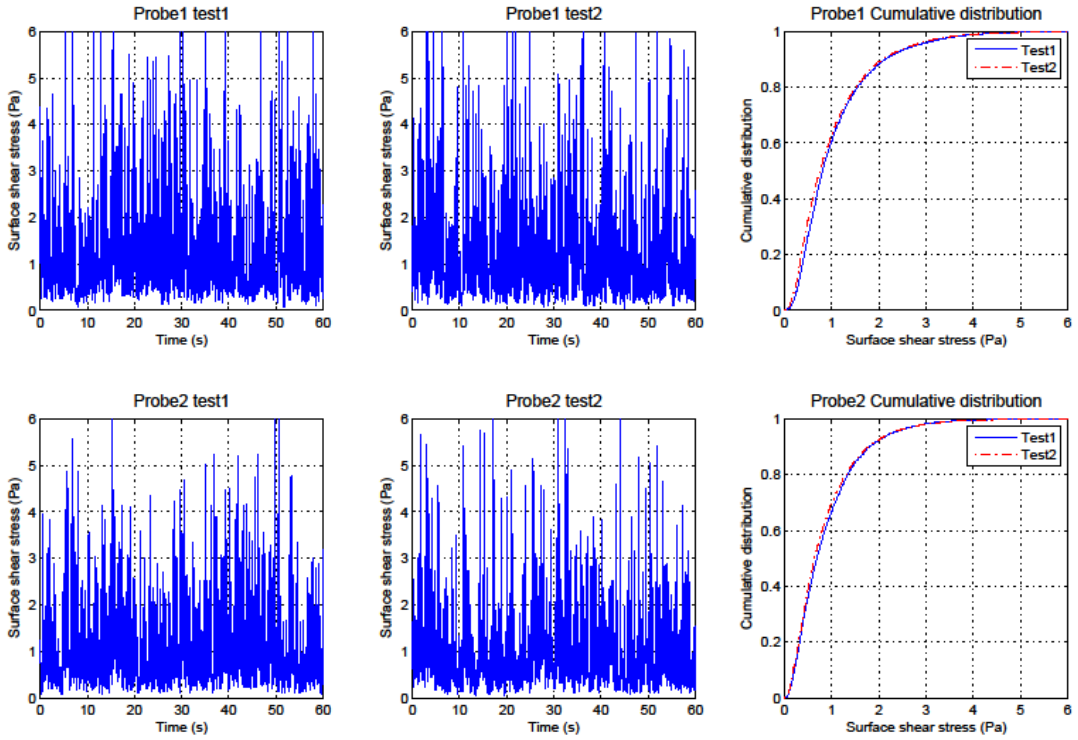

Figure A11-51. Result of FHWSC1.3.

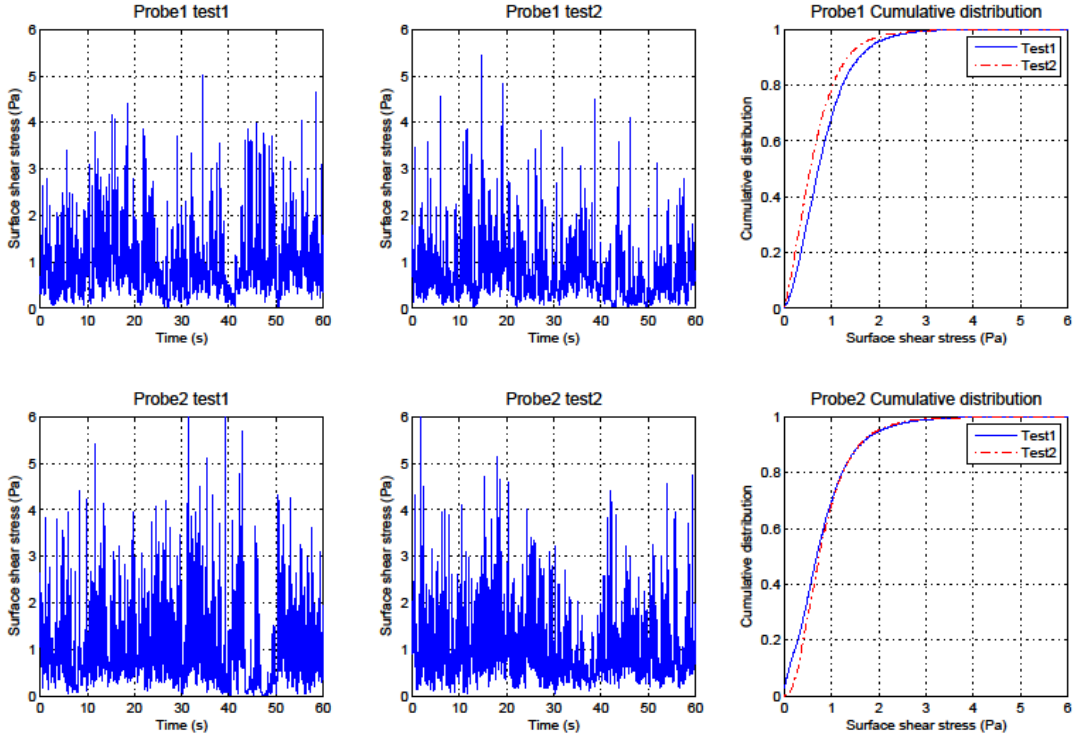

Figure A11-52. Result of FLWCC1.3.

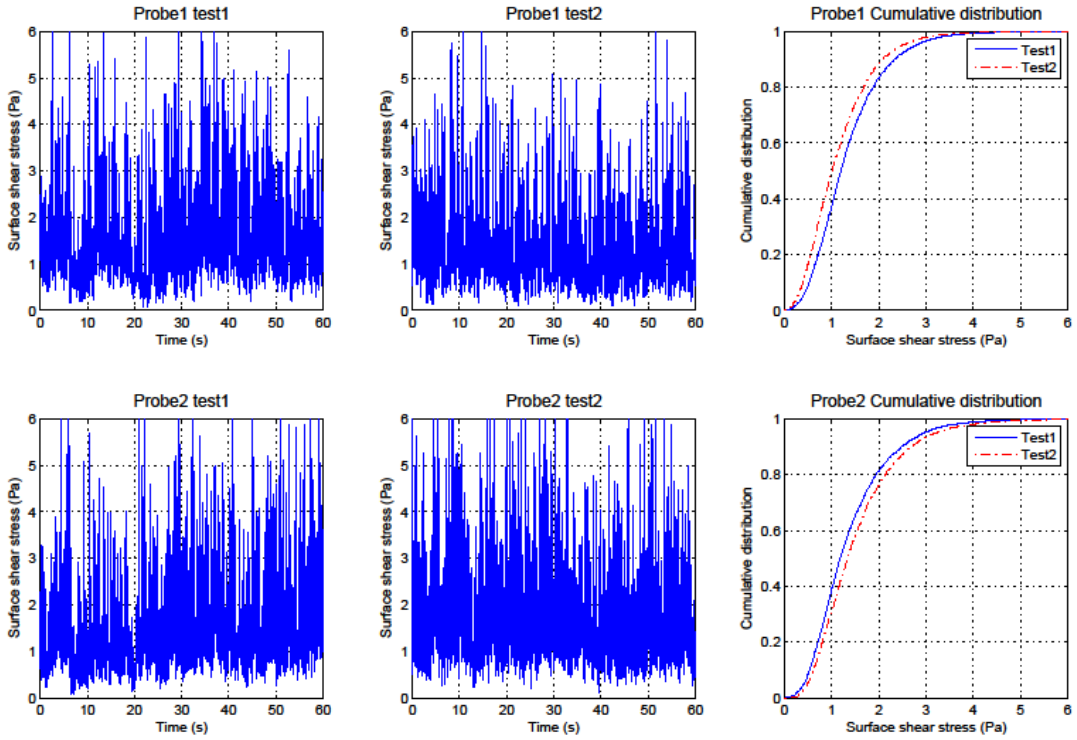

Figure A11-53. Result of FMWCC1.3.

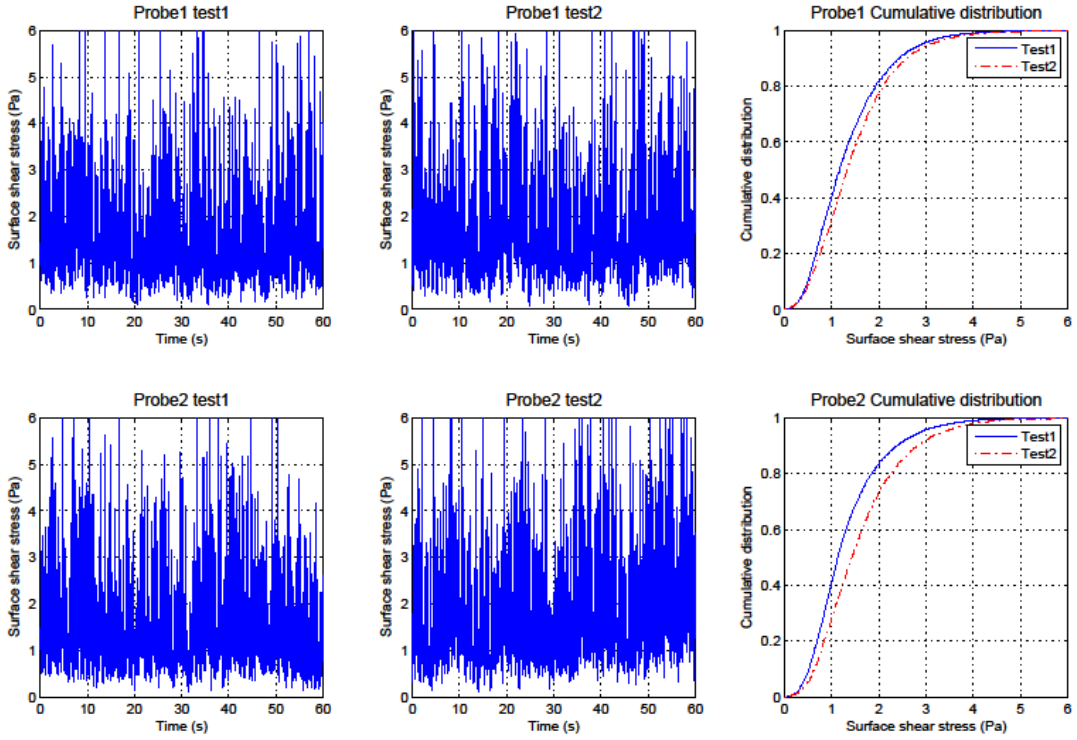

Figure A11-54. Result of FHWCC1.3.

APPENDIX 12. RMS, MEAN AND STD FOR ALL SHEAR STRESS MEASUREMNTS.

Table A12-1. The RMS, mean and STD of shear stress values for the 54 experiments in D14 tank.

	Probe1 Test1			Probe2 Test1			Probe1 Test2			Probe2 Test2		
	RMS	Mean	Std	RMS	Mean	Std	RMS	Mean	Std	RMS	Mean	Std
PLOSC1.3	0.635	0.370	0.516	0.708	0.350	0.615	0.654	0.359	0.547	0.744	0.419	0.615
PLOSC2.2	0.615	0.367	0.494	0.997	0.574	0.815	0.754	0.444	0.609	0.930	0.537	0.759
PMOSC1.3	0.822	0.496	0.656	0.810	0.506	0.632	0.850	0.557	0.642	0.876	0.540	0.690
PMOSC2.2	0.939	0.606	0.718	-	-	-	0.881	0.590	0.654	-	-	-
PHOSC1.3	0.990	0.672	0.727	1.092	0.678	0.856	0.985	0.643	0.747	0.985	0.655	0.735
PHOSC2.2	0.953	0.614	0.730	0.823	0.513	0.643	0.912	0.608	0.679	0.739	0.511	0.534
PLWSC1.3	0.940	0.716	0.608	0.942	0.712	0.617	0.986	0.761	0.626	0.834	0.635	0.541
PMWSC1.3	1.173	0.941	0.700	0.876	0.615	0.624	1.151	0.862	0.762	0.806	0.506	0.627
PHWSC1.3	1.280	0.938	0.870	1.012	0.672	0.757	1.227	0.942	0.787	1.020	0.691	0.750
PLWCC1.3	1.115	0.849	0.723	0.927	0.786	0.491	1.022	0.870	0.536	0.923	0.778	0.496
PMWCC1.3	1.315	1.109	0.706	1.208	1.047	0.602	1.414	1.203	0.743	1.208	1.052	0.594
PHWCC1.3	1.496	1.293	0.753	1.455	1.267	0.715	1.487	1.300	0.723	1.419	1.246	0.678
CLOSC1.3	0.423	0.299	0.299	0.468	0.325	0.337	0.612	0.426	0.440	0.528	0.378	0.368
CLOSC2.2	0.709	0.521	0.480	0.571	0.397	0.410	0.655	0.476	0.451	0.580	0.410	0.410
CLOSF1.3	0.524	0.357	0.383	0.379	0.219	0.310	0.592	0.396	0.440	0.433	0.273	0.336
CLOSF2.2	0.510	0.355	0.366	0.490	0.310	0.380	0.558	0.392	0.398	0.584	0.384	0.440
CLOSS1.3	0.573	0.370	0.437	0.508	0.294	0.414	0.422	0.251	0.340	0.358	0.197	0.299
CLOSS2.2	0.463	0.290	0.360	0.374	0.222	0.301	0.597	0.369	0.469	0.433	0.240	0.361
CMOSC1.3	0.657	0.487	0.441	0.568	0.399	0.404	0.747	0.559	0.496	0.543	0.389	0.379
CMOSC2.2	0.751	0.552	0.510	0.574	0.413	0.398	0.840	0.626	0.560	0.638	0.453	0.449
CMOSF1.3	0.613	0.389	0.474	0.547	0.331	0.435	0.699	0.440	0.543	0.480	0.283	0.387
CMOSF2.2	0.631	0.429	0.463	0.621	0.393	0.482	0.675	0.459	0.494	0.641	0.422	0.482
CMOSS1.3	0.733	0.443	0.584	0.460	0.267	0.374	0.672	0.396	0.543	0.470	0.268	0.385
CMOSS2.2	0.759	0.438	0.620	0.497	0.313	0.386	0.659	0.415	0.513	0.610	0.380	0.477
CHOSC1.3	0.901	0.643	0.631	0.719	0.518	0.498	0.680	0.509	0.451	0.719	0.488	0.527
CHOSC2.2	0.860	0.641	0.574	0.792	0.592	0.527	0.866	0.645	0.578	0.739	0.518	0.528
CHOSF1.3	0.793	0.466	0.641	0.557	0.345	0.437	0.803	0.539	0.595	0.677	0.414	0.535
CHOSF2.2	0.813	0.546	0.603	0.659	0.407	0.519	0.779	0.494	0.602	0.629	0.407	0.480
CHOSS1.3	0.618	0.375	0.491	0.638	0.387	0.508	0.605	0.375	0.475	0.558	0.315	0.460
CHOSS2.2	0.763	0.470	0.602	0.608	0.329	0.512	0.782	0.495	0.605	0.702	0.424	0.559
CLWSC1.3	0.962	0.762	0.587	0.959	0.731	0.620	0.925	0.718	0.583	0.788	0.580	0.534
CLWSF1.3	0.765	0.525	0.556	0.647	0.422	0.490	0.777	0.540	0.559	0.672	0.483	0.468
CLWSS1.3	0.776	0.496	0.597	0.607	0.380	0.474	0.631	0.370	0.511	0.656	0.426	0.498
CMWSC1.3	1.336	1.085	0.779	1.051	0.817	0.661	1.292	1.017	0.797	1.000	0.765	0.645
CMWSF1.3	1.018	0.684	0.754	0.829	0.550	0.621	0.992	0.677	0.726	1.012	0.690	0.739
CMWSS1.3	1.054	0.705	0.783	0.980	0.657	0.727	1.163	0.746	0.893	0.857	0.498	0.697
CHWSC1.3	1.474	1.181	0.881	1.164	0.923	0.709	1.476	1.153	0.921	1.126	0.890	0.691
CHWSF1.3	1.241	0.796	0.952	0.872	0.543	0.683	1.209	0.839	0.871	0.911	0.603	0.683
CHWSS1.3	1.237	0.826	0.920	1.045	0.678	0.795	1.302	0.839	0.996	1.087	0.664	0.861
CLWCC1.3	1.076	0.886	0.611	1.227	1.040	0.652	1.030	0.879	0.536	1.530	1.301	0.805
CLWCF1.3	0.809	0.610	0.530	1.048	0.804	0.672	0.841	0.621	0.568	0.918	0.688	0.607
CLWCS1.3	0.870	0.579	0.649	0.777	0.526	0.572	0.695	0.436	0.541	0.696	0.431	0.546
CMWCC1.3	1.269	1.081	0.665	1.255	1.069	0.657	1.234	1.019	0.696	1.164	0.974	0.636
CMWCF1.3	0.959	0.713	0.641	0.961	0.658	0.700	1.121	0.880	0.695	1.097	0.848	0.696
CMWCS1.3	1.006	0.655	0.764	0.983	0.685	0.705	0.990	0.664	0.734	0.853	0.571	0.633
CHWCC1.3	1.512	1.314	0.747	1.447	1.238	0.748	1.425	1.202	0.766	1.334	1.105	0.747
CHWCF1.3	1.300	0.985	0.849	1.206	0.927	0.772	1.355	1.048	0.859	1.200	0.961	0.718
CHWCS.13	1.157	0.796	0.840	1.141	0.823	0.791	1.144	0.791	0.827	1.113	0.780	0.794

	Probe1 Test1			Probe2 Test1			Probe1 Test2			Probe2 Test2		
	RMS	Mean	Std	RMS	Mean	Std	RMS	Mean	Std	RMS	Mean	Std
FLWSC1.3	0.867	0.680	0.538	0.796	0.611	0.511	0.862	0.658	0.557	0.662	0.509	0.423
FMWSC1.3	1.178	0.926	0.727	0.956	0.746	0.598	1.218	0.948	0.765	0.826	0.637	0.526
FHWSC.13	1.403	1.111	0.855	1.182	0.939	0.717	1.356	1.054	0.853	1.157	0.902	0.724
FLWCC1.3	1.056	0.882	0.581	1.071	0.857	0.642	0.893	0.715	0.534	1.087	0.916	0.585
FMWCC1.3	1.585	1.390	0.763	1.654	1.428	0.835	1.401	1.202	0.720	1.815	1.580	0.894
FHWCC1.3	1.618	1.394	0.822	1.591	1.373	0.804	1.756	1.527	0.867	1.901	1.658	0.929

Table A12-2. The RMS, mean and STD of shear stress values for the 2 experiments in D20 tank.

	Test 1			Test 2			Test 3		
Slow pulse	RMS	Mean	Std	RMS	Mean	Std	RMS	Mean	Std
Probe1	0.953	0.562	0.770	0.918	0.523	0.754	1.040	0.571	0.871
Probe2	0.861	0.500	0.701	0.847	0.480	0.698	0.877	0.481	0.734
Fast pulse									
Probe1	1.010	0.644	0.784	0.993	0.610	0.784	0.947	0.610	0.724
Probe2	0.782	0.496	0.604	0.789	0.484	0.623	0.778	0.497	0.598

APPENDIX 13. FILTRATION TESTS RESULTS

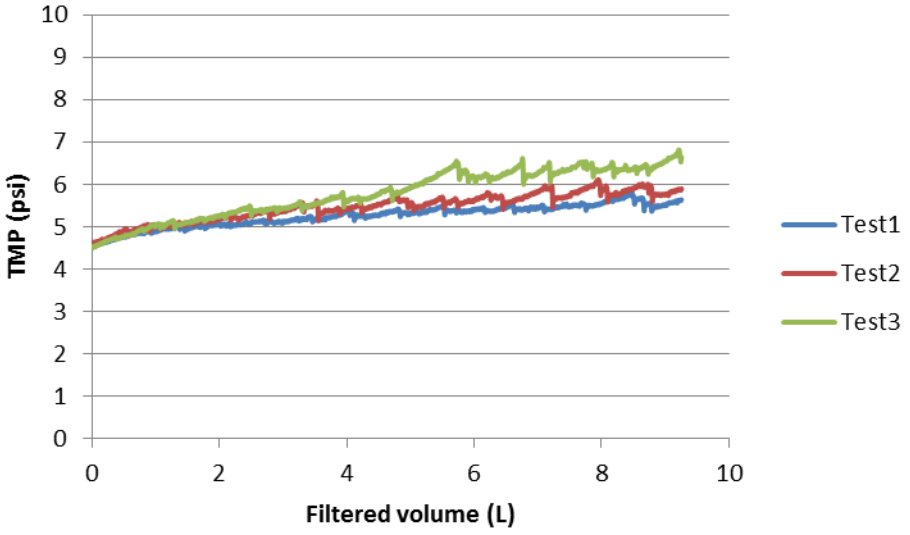

Figure A13-1. Filtered volume vs. TMP under the condition of slow pulse diffuser, stagnant bulk liquid and 3500 mL/min continuous gas flow in D14 tank.

Table A13-1. Filtration model fitting of the results under the condition of slow pulse diffuser, stagnant bulk liquid and 3500 mL/min continuous gas flow in D14 tank.

	Model	Test 1		Test 2		Test 3		k_i	
		k_i	R^2	k_i	R^2	k_i	R^2	Mean	STD
Complete blocking	$P_t = \frac{P_0}{1 - k_b V}$	0.0270	0.2860	0.0324	0.1326	0.0419	0.6954	0.0338	0.0075
Intermediate blocking	$P_t = P_0 e^{k_i V}$	0.0294	0.4223	0.0366	0.3274	0.0488	0.7865	0.0383	0.0098
Cake fouling	$P_t = P_0 + k_c V$	0.1455	0.5367	0.1854	0.4830	0.2588	0.8668	0.1966	0.0575

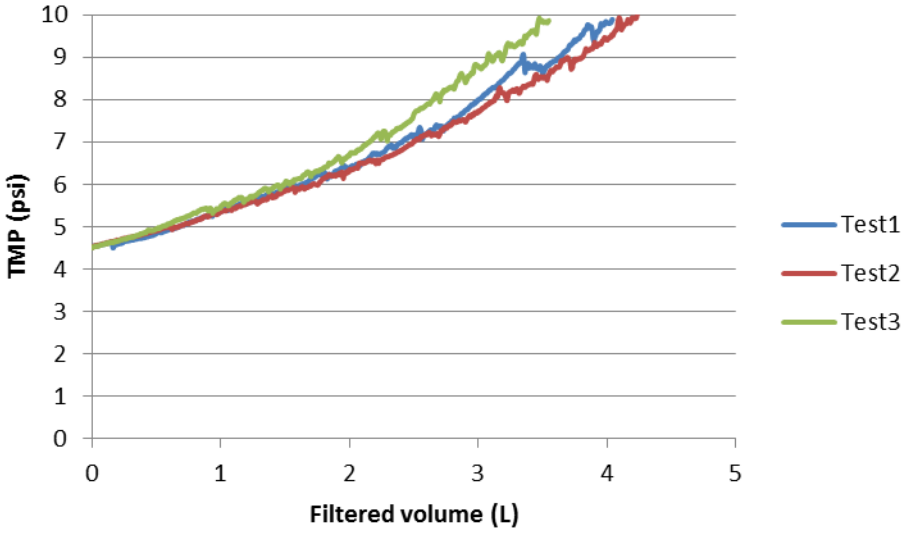

Figure A13-2. Filtered volume vs. TMP under the condition of coarse bubble diffuser, stagnant bulk liquid and 3500 mL/min continuous gas flow in D14 tank.

Table A13-2. Filtration model fitting of the results under the condition of coarse bubble diffuser, stagnant bulk liquid and 3500 mL/min continuous gas flow in D14 tank.

	Model	Test 1		Test 2		Test 3		k_i	
		k_i	R^2	k_i	R^2	k_i	R^2	Mean	STD
Complete blocking	$P_t = \frac{P_0}{1 - k_b V}$	0.1440	0.9915	0.1373	0.9900	0.1625	0.9938	0.1479	0.0130
Intermediate blocking	$P_t = P_0 e^{k_i V}$	0.1894	0.9896	0.1808	0.9956	0.2133	0.9909	0.1945	0.0168
Cake fouling	$P_t = P_0 + k_c V$	1.1646	0.9549	1.1107	0.9595	1.3084	0.9489	1.1946	0.1022

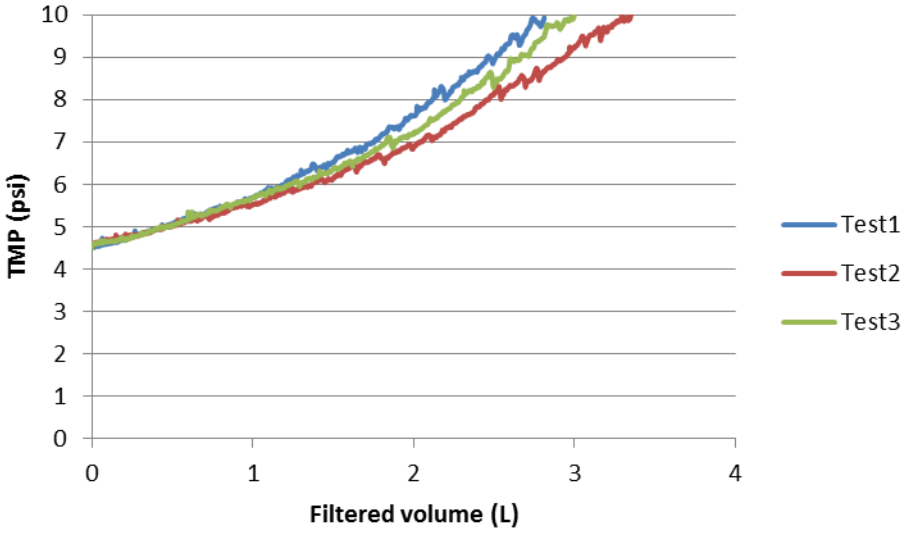

Figure A13-3. Filtered volume vs. TMP under the condition of coarse bubble diffuser, stagnant bulk liquid and 3500 mL/min 3 sec on 3 sec off gas flow in D14 tank.

Table A13-3. Filtration model fitting of the results under the condition of coarse bubble diffuser, stagnant bulk liquid and 3500 mL/min 3 sec on 3 sec off gas flow in D14 tank.

	Model	Test 1		Test 2		Test 3		k_i	
		k_i	R^2	k_i	R^2	k_i	R^2	Mean	STD
Complete blocking	$P_t = \frac{P_0}{1 - k_b V}$	0.2039	0.9965	0.1742	0.9917	0.1908	0.9946	0.1896	0.0149
Intermediate blocking	$P_t = P_0 e^{k_i V}$	0.2675	0.9896	0.2298	0.9914	0.2500	0.9887	0.2491	0.0189
Cake fouling	$P_t = P_0 + k_c V$	1.6401	0.9453	1.4186	0.9489	1.5307	0.9412	1.5298	0.1108

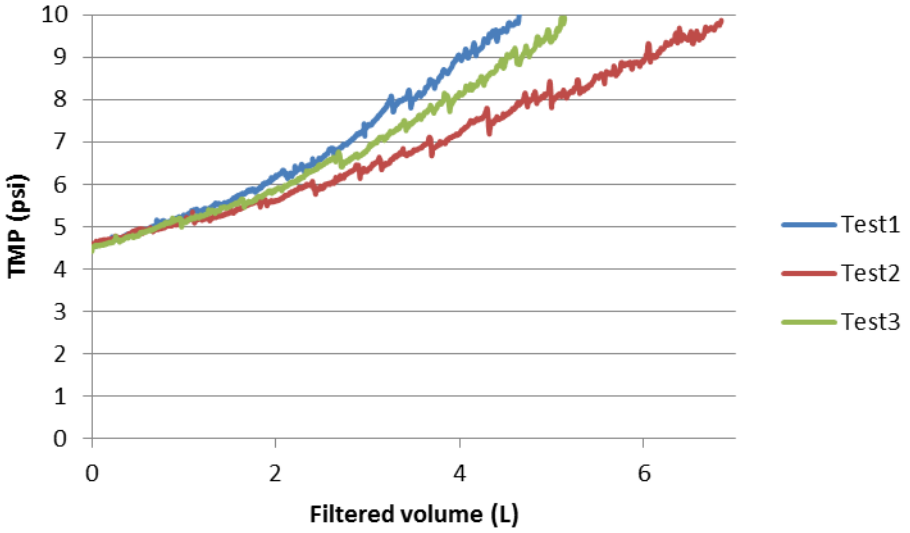

Figure A13-4. Filtered volume vs. TMP under the condition of coarse bubble diffuser, stagnant bulk liquid and 7000 mL/min 2 sec on 2 sec off gas flow in D14 tank.

Table A13-4. Filtration model fitting of the results under the condition of coarse bubble diffuser, stagnant bulk liquid and 7000 mL/min 2 sec on 2 sec off gas flow in D14 tank.

	Model	Test 1		Test 2		Test 3		k_i	
		k_i	R^2	k_i	R^2	k_i	R^2	Mean	STD
Complete blocking	$P_t = \frac{P_0}{1 - k_b V}$	0.1260	0.9913	0.0878	0.9618	0.1116	0.9912	0.1085	0.0193
Intermediate blocking	$P_t = P_0 e^{k_i V}$	0.1661	0.9926	0.1162	0.9958	0.1463	0.9935	0.1429	0.0251
Cake fouling	$P_t = P_0 + k_c V$	1.0238	0.9544	0.7172	0.9813	0.8938	0.9580	0.8783	0.1539

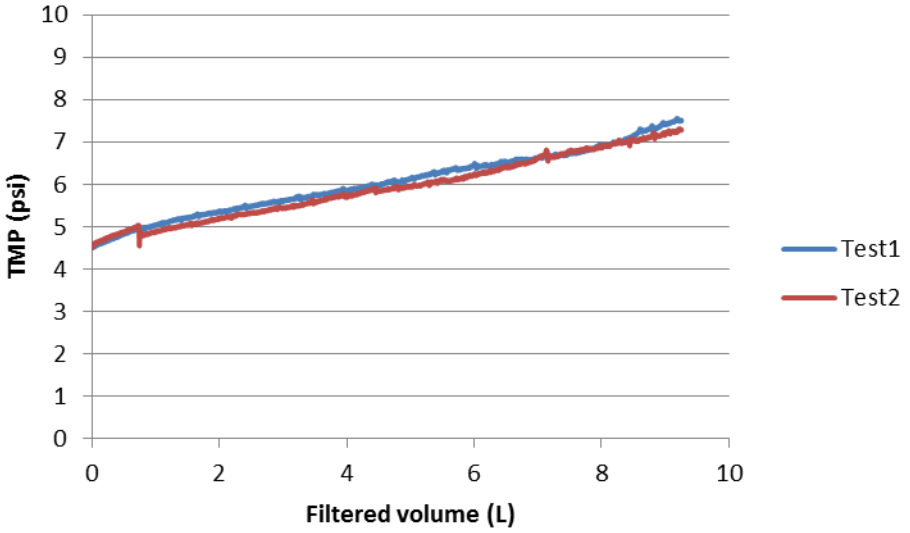

Figure A13-5. Filtered volume vs. TMP under the condition of slow pulse diffuser, cross-flow bulk liquid and 3500 mL/min continuous gas flow in D20 tank.

Table A13-5. Filtration model fitting of the results under the condition of slow pulse diffuser, cross-flow bulk liquid and 3500 mL/min continuous gas flow in D20 tank.

	Model	Test 1		Test 2		k_i	
		k_i	R^2	k_i	R^2	Mean	STD
Complete blocking	$P_t = \frac{P_0}{1 - k_b V}$	0.0482	0.8168	0.0459	0.9076	0.0470	0.0016
Intermediate blocking	$P_t = P_0 e^{k_i V}$	0.0580	0.9144	0.0548	0.9648	0.0564	0.0023
Cake fouling	$P_t = P_0 + k_c V$	0.3186	0.9666	0.2990	0.9885	0.3088	0.0139

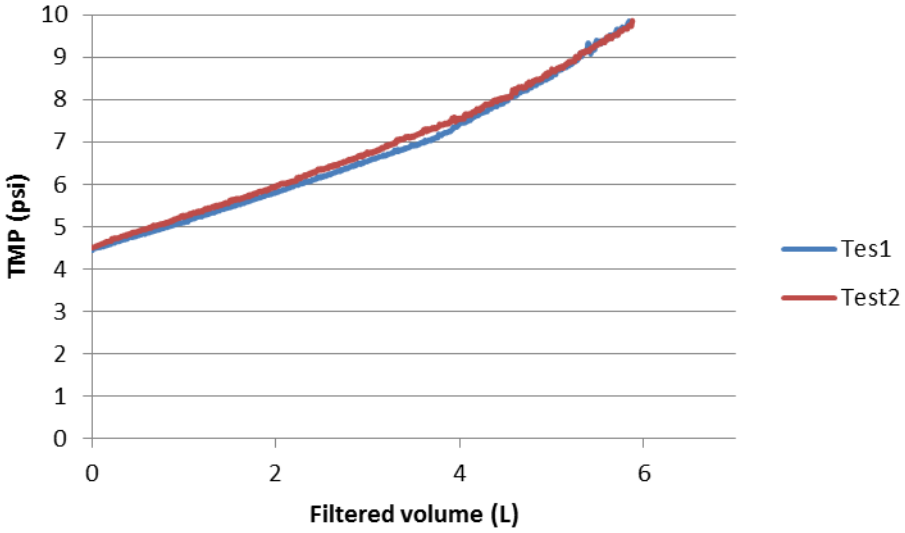

Figure A13-6. Filtered volume vs. TMP under the condition of slow pulse diffuser, cross-flow bulk liquid and 1750 mL/min continuous gas flow in D20 tank.

Table A13-6. Filtration model fitting of the results under the condition of slow pulse diffuser, cross-flow bulk liquid and 1750 mL/min continuous gas flow in D20 tank.

	Model	Test 1		Test 2		k_i	
		k_i	R^2	k_i	R^2	Mean	STD
Complete blocking	$P_t = \frac{P_0}{1 - k_b V}$	0.0981	0.9832	0.1008	0.9543	0.0995	0.0019
Intermediate blocking	$P_t = P_0 e^{k_i V}$	0.1281	0.9973	0.1323	0.9967	0.1302	0.0030
Cake fouling	$P_t = P_0 + k_c V$	0.7789	0.9663	0.8090	0.9847	0.7940	0.0213

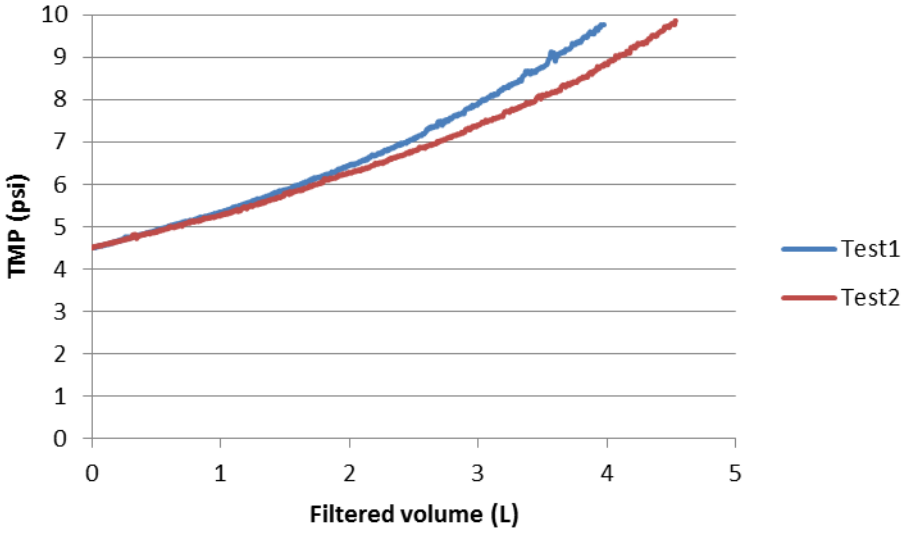

Table A13-7. Filtration model fitting of the results under the condition of slow pulse diffuser, cross-flow bulk liquid and 875 mL/min continuous gas flow in D20 tank.

Table A13-7. Filtration model fitting of the results under the condition of slow pulse diffuser, cross-flow bulk liquid and 875 mL/min continuous gas flow in D20 tank.

	Model	Test 1		Test 2		k_i	
		k_i	R^2	k_i	R^2	Mean	STD
Complete blocking	$P_t = \frac{P_0}{1 - k_b V}$	0.1436	0.9921	0.1278	0.9840	0.1357	0.0111
Intermediate blocking	$P_t = P_0 e^{k_i V}$	0.1876	0.9959	0.1674	0.9988	0.1775	0.0143
Cake fouling	$P_t = P_0 + k_c V$	1.1429	0.9602	1.0222	0.9705	1.0826	0.0853

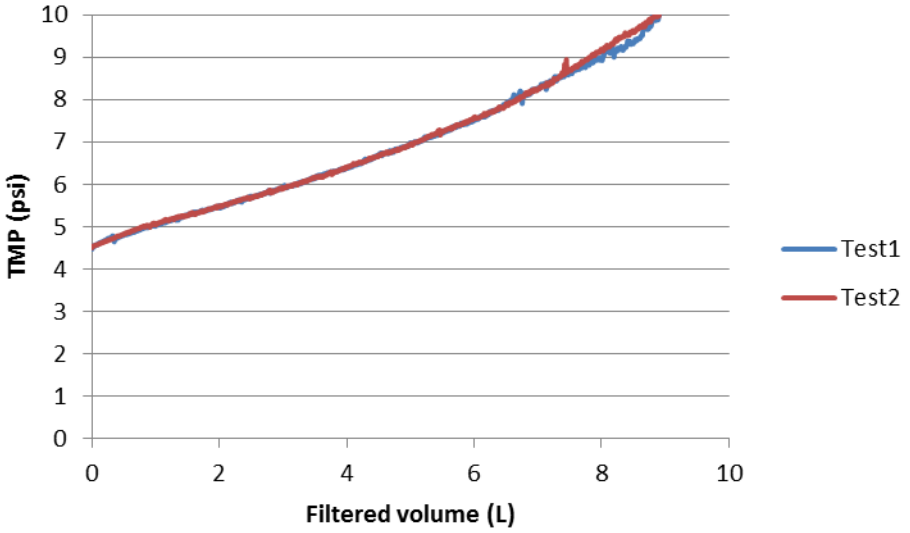

Table A13-8. Filtration model fitting of the results under the condition of fast pulse diffuser, cross-flow bulk liquid and 3500 mL/min continuous gas flow in D20 tank.

Table A13-8. Filtration model fitting of the results under the condition of slow pulse diffuser, cross-flow bulk liquid and 3500 mL/min continuous gas flow in D20 tank.

	Model	Test 1		Test 2		k_i	
		k_i	R^2	k_i	R^2	Mean	STD
Complete blocking	$P_t = \frac{P_0}{1 - k_b V}$	0.0666	0.9530	0.0671	0.9558	0.0668	0.0003
Intermediate blocking	$P_t = P_0 e^{k_i V}$	0.0873	0.9956	0.0882	0.9951	0.0878	0.0006
Cake fouling	$P_t = P_0 + k_c V$	0.5350	0.9808	0.5426	0.9745	0.5388	0.0054

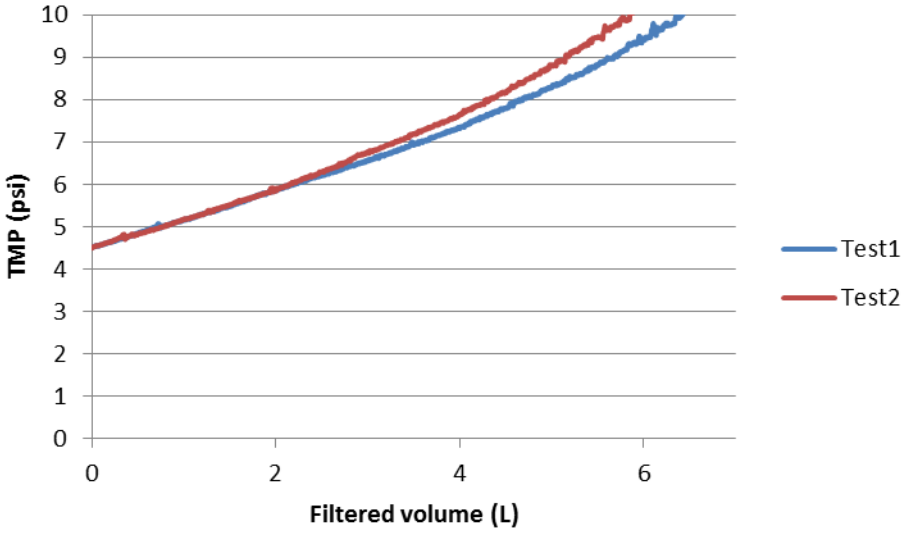

Table A13-9. Filtration model fitting of the results under the condition of fast pulse diffuser, cross-flow bulk liquid and 1750 mL/min continuous gas flow in D20 tank.

Table A13-9. Filtration model fitting of the results under the condition of slow pulse diffuser, cross-flow bulk liquid and 1750 mL/min continuous gas flow in D20 tank.

	Model	Test 1		Test 2		k_i	
		k_i	R^2	k_i	R^2	Mean	STD
Complete blocking	$P_t = \frac{P_0}{1 - k_b V}$	0.0936	0.9586	0.1017	0.9743	0.0977	0.0057
Intermediate blocking	$P_t = P_0 e^{k_i V}$	0.1239	0.9979	0.1343	0.9995	0.1291	0.0074
Cake fouling	$P_t = P_0 + k_c V$	0.7651	0.9821	0.8297	0.9753	0.7974	0.0457

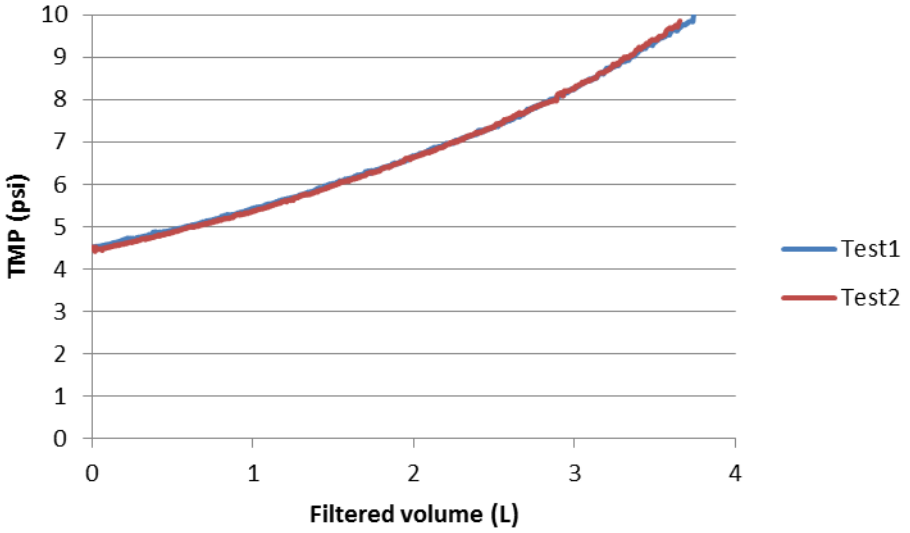

Table A13-10. Filtration model fitting of the results under the condition of fast pulse diffuser, cross-flow bulk liquid and 875 mL/min continuous gas flow in D20 tank.

Table A13-10. Filtration model fitting of the results under the condition of slow pulse diffuser, cross-flow bulk liquid and 875 mL/min continuous gas flow in D20 tank.

	Model	Test 1		Test 2		k_i	
		k_i	R^2	k_i	R^2	Mean	STD
Complete blocking	$P_t = \frac{P_0}{1 - k_b V}$	0.1539	0.9921	0.1544	0.9956	0.1541	0.0003
Intermediate blocking	$P_t = P_0 e^{k_i V}$	0.2020	0.9958	0.2011	0.9924	0.2016	0.0006
Cake fouling	$P_t = P_0 + k_c V$	1.2359	0.9590	1.2220	0.9536	1.2290	0.0098